University of Southampton

EXAFS STUDIES OF CARBON SUPPORTED FUEL CELLS ELECTROCATALYSTS

By

Stéphanie Maniguet

A Thesis Submitted For The Degree Of
Doctor Of Philosophy

Department of Chemistry

July 2002

UNIVERSITY OF SOUTHAMPTON

ABSTRACT

FACULTY OF SCIENCE

CHEMISTRY

Doctor of Philosophy

EXAFS studies of carbon supported fuel cells catalysts

By Stéphanie Maniguet

Carbon supported Pt, PtRu and PtMo fuel cell catalysts were investigated by means of advanced synchrotron X-ray absorption spectroscopies (XAS), in particular extended X-ray absorption fine structure (EXAFS) and X-ray absorption near edge structure (XANES). EXAFS results at both the Pt L_{III} and Ru K edges for the PtRu/C electrocatalysts have highlighted the interference of the backscattering from secondary metal element, Ru, with that from Pt when the neighbours were at similar distances. The resulting phase cancellation in the EXAFS at about k ~10 $Å^{-1}$ gave rise to a splitting of the main peak of the Fourier transform. The extent of intermixing in the alloy could then be related to the extent to which this peak was split. Shortened first shell Pt-Pt coordination distances and decreased first shell coordination numbers provided evidence of the smaller size of carbon supported small platinum particles when modified with Ru or Mo. While the complementary Ru K edge investigation reflected the metallic nature of the Ru at a reducing potential, XAS results at the Mo K edge indicated the presence of Mo oxyhydroxide species at the surface of the particle related to the presence of the redox couple Mo(IV)/Mo(VI), as indicated by changes in the XANES feature as function of potential. The performance of proton exchange membrane fuel cells with PtRu and PtMo catalysts on reformate mixes containing up to 100 ppm CO was enhanced over that of Pt. The enhancement of the catalytic activity for the CO electro-oxidation reaction by PtRu/C electrocatalysts is thought to arise from an intrinsic mechanism rather than the presence of oxide on the Ru surface. Whereas the Mo oxyhydroxide species are thought to play a significant role to oxidise CO adsorbed species at lower potentials than Pt. Finally, *in situ* EXAFS investigation of fuel cell electrocatalysts was shown to be sensitive to the surface composition of the metal particles (CO and O) and, therefore, may be used to investigate the chemistry of the fuel cell reactions.

Acknowledgements

I would like to thank Dr Andrea Russell for having given me the opportunity to do my PhD in her research group in the department of chemistry at the university of Southampton. I appreciated very much her scientific contribution in the understanding and the development of the project I have been working on for three years. I will also remember her human qualities for plenty of reasons.

I would like to thank Johnson Matthey Technology Centre for having sponsored my work and also, let me use their equipments. This sponsorship gave me the great opportunity to spend some time in an interesting and professional environment. I would like to thank more particularly Dr Dave Thompsett and Dr Sarah Ball for their patience and their availability every time I was visiting, and this, in addition to their scientific collaboration.

Thank to all the students of the group (Jun, Fabrice, Anne, Becky and Abbe) that I enjoyed working with and especially spending days and nights at Daresbury to experiment our samples at the stations 9.2 and 9.3. Thank to Linda for having helped me so much when I first started at the university of Southampton. Talking of my first steps in England I would also more specifically thank Dr Gert van Dorssen that introduced me to the technique of EXAFS.

Thank to all my french and english friends that I met during my PhD (Chris, Fiona, Mark, Stéphane, Claire, Cécile, Steven). Warm thanks to Sheila and Sam for having offered me 'Gite et couvert' and also, a great psychological support during all the time periods I attempted to finish the writing up of my PhD back to England.

Un merci tout particulier à Denis pour sa grande capacité d'adaptation face à mes sauts d'humeur pendant la période de rédaction mais aussi pour tous ses encouragements d'expert !!

CONTENTS

Chapter one : Introduction

Chapter two : Experimental and techniques

Chapter three : EXAFS study of PtRu/C fuel cell electrocatalysts

Chapter four : Potential dependance of the EXAFS of Pt-based fuel cell electrodes

Chapter five : EXAFS of CO on Pt/C electrodes

CHAPTER ONE : INTRODUCTION

1 GENERAL INTRODUCTION

At the present time, growing concerns about ecological damage, such as global warming originating particularly from carbon dioxide emissions, together with the long term scarcity of fossil fuel feedstocks emphasise the need for more acceptable sources of energy. Consequently, the reduction of CO_2 emissions resulting from the combustion of hydrocarbon compounds (petroleum or natural gas) that are largely used to generate electrical, thermal and mechanical energy is a challenging target. For instance, the alternative is either to increase the efficiency of the existing energy converters using hydrocarbon compounds as fuel or to use non fossil fuels (biological fuels and hydrogen). In the latter case, 'clean' hydrogen can result from electrolysis using electricity produced without CO_2 emission (solar, hydraulic, nuclear, aeolian) or from the gasification of biomass products (diester, ethanol, or biogas) that are already commercialised or still under study (methane, methanol, ...). Also, fuel cell technology that uses hydrogen as fuel contributed largely to the development of emission control technology. In this, the legislation has helped with the introduction of California's Zero Emission Vehicles (ZEVs) mandate in 1994 [1]. Though batteries were originally first candidate to power electric vehicles, they have insufficient driving range together with a high weight and cost. Also, the consumption of the reactants contained inside the battery leads to the need to recharge or to replace the battery unit. In contrast, the continuous supply of reactants from an external source gives longer life time to the fuel cell unit. Fuel cells are no longer just a potential electric power generation technology, but are now providers of clean energy. Low emission behaviour as well as simple mechanical engineering make fuel cells more attractive in comparison to the conventional fossil-fuel combustion power sources. Other advantages characterise fuel cells such as:

- high thermodynamic efficiencies, particularly when hydrogen is used as a fuel
- rapid response time
- good power/weight ratio and modularity in construction.

Although the first attempt to generate electricity from hydrogen and oxygen based on the reversed water electrolysis reaction was observed by Sir W. Grove in 1839 [2], it was not until 100 years later that F.T. Bacon pioneered the modern fuel cell idea. The development of the hydrogen/oxygen fuel cell using cheap nickel-based electrodes and an alkaline electrolyte started in the early 1930's. Further research led to the optimisation of the Alkaline Fuel Cell (AFC) to a multi-kilowatts power source that found its first application in the Gemini and Apollo space programmes in the 1960s [1]. In addition to its compact structure (no moving parts) and high power/weight ratio, a fuel cell is quiet and produces water and heat (see Equation 2).

2 FUEL CELLS

2.1 Principles

The operating principles of fuel cells are straightforward, since they convert chemical free energy directly into electrical energy. Any electrochemical reaction, whose overall free energy is negative can be used to drive a fuel cell and the maximum voltage from such a cell is given by [3]:

$$E = \frac{-\Delta G}{nF} \qquad \text{Equation 1}$$

where n is the number of electrons transfered from the anode to the cathode during one act of the overall reaction, F is the Faraday constant (96 500 C mol^{-1}) and ΔG is the Gibbs Free Energy of the reaction.

Fuel cell devices rely on supplying gaseous reactants, e.g. hydrogen and oxygen, separately to two electrodes immersed in an electrolyte (ion conducting medium) and connected to an external circuit carrying the load. Figure 1 illustrates the mode of operation of a primary hydrogen/oxygen fuel cell that uses an aqueous alkaline electrolyte (e.g. KOH). The hydroxyl ions (OH^-) migrate from the cathode to the anode where they react with hydrogen fuel to produce water and electrons (Equation *i*). These electrons are used to power an external circuit, then return to the cathode side where they combine with water molecules to

reduce the oxidant or oxygen (usually air) into more hydroxyl ions (Equation *ii*). The fuel cell overall reaction is given by Equation 2.

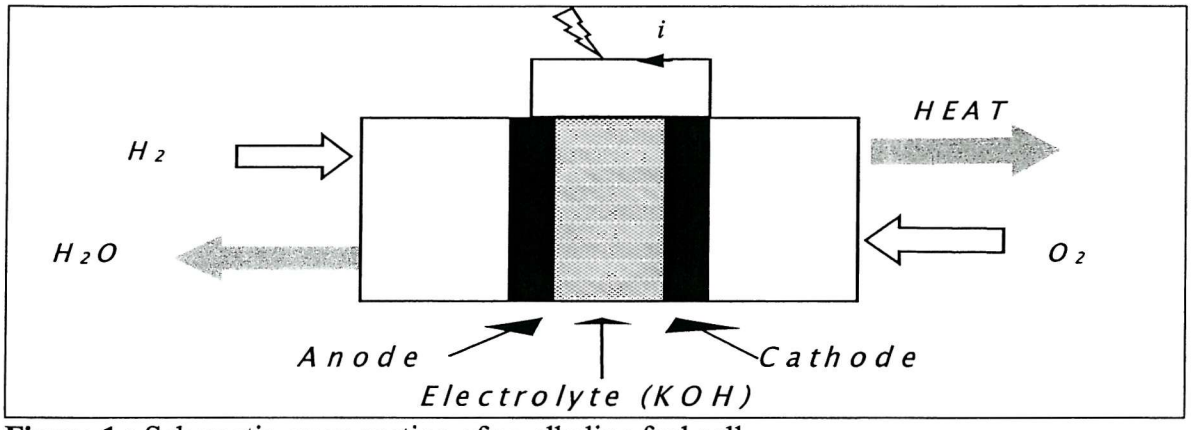

Figure 1 : Schematic cross-section of an alkaline fuel cell.

$2H_2 + O_2 \Rightarrow 2H_2O$	E = 1.23 V vs. NHE (ΔG = -113.4 kcal)	Equation 2
$H_2 + 2OH^- \Rightarrow 2H_2O + 2e^-$	E_{anode} = 0 V vs. NHE	Equation *i*
$O_2 + 2H_2O + 4e^- \Rightarrow 4OH^-$	$E_{cathode}$ = 1.23 V vs. NHE	Equation *ii*

Within the whole family of fuel cells that have been widely described in the literature, the electrolyte used is the major difference. Thus, either protons or oxide ions are transported through the ion-conducting medium which is also an electronic insulator. Table 1 lists the family of the fuel cells with their corresponding electrolyte (solid or liquid) which dictates the operating temperature, varying from 70 °C to 1000 °C.

2.2 Description and applications

The Alkaline Fuel Cell (AFC) has the longest history of the fuel cell technology. Its main advantages are the use of non-noble metal catalysts, namely Ni and low operating temperatures (from 60 to 130 °C), since the oxygen reduction is facile in alkaline electrolyte. Although recognised as the cheapest type of fuel cell to manufacture, AFCs are too bulky for use in car engines, but are suitable for small stationary power generation unit. Exceptionally, precious metal based electrocatalysts are more durable than adequate to achieve the high current densities [4]. In that case, AFCs become sensitive to CO species that would poison catalyst. But, the main concern for the Alkaline Fuel Cell is the presence

of CO_2 in the oxidant (i.e. air) which is easily absorbed into the alkaline electrolyte. This generates relatively insoluble potassium carbonate (K_2CO_3) that, in turn, poisons the cathode. The alternative, using an acid electrolyte, improves the tolerance towards CO_2 that decreases the performance of the fuel cell.

Phosphoric Acid Fuel Cells (PAFCs) introduced in 1967 dominate the low temperature fuel cell market. PAFCs are recognised as the most mature system providing power and heat, from steam, since the number of stationary power plants installed has doubled between 1997 and 1999. This was achieved by ONSI Corp. that installed 160 PC25™ units rated at 200 kW and a life time of 40,000 hours [5]. A unit was running 9500 hours (13 months) at full rated load. Thereby, their reliability is such that they have been marketed as un-interruptible power sources (UPSs) for installations such as computer facilities and hospitals [6]. However, the use of reformate fuel containing 1% to 2% CO and H_2S considerably reduces the PAFCs predominance by poisoning the platinum catalyst. Therefore, the necessity of a desulfurizer device reduces the stack flexibility and limits fuel cell applications mainly to stationary power plants. But, at 190 °C to 210 °C the anode performance is very good even on fuels containing up to 5% CO. Lower operating temperatures would reduce the ionic conductivity of the H_3PO_4 and higher operating temperatures would cause instability of the carbon and platinum materials [3].

Molten Carbonate Fuel Cells (MCFCs) operate at higher temperatures (e.g. 650 °C), usually above the melting point of the alkali metal carbonate electrolyte (i.e. ion conduction by CO_3^{2-}). At such elevated temperatures CO acts as a fuel rather than a poisoning species by means of internal reforming of the hydrocarbons that provide H_2 directly within the fuel cell structure (Equation 3).

$$CO + H_2O \rightarrow CO_2 + H_2 \qquad \text{Equation 3}$$

Operating at even higher temperatures (800 °C to 1000 °C), Solid Oxide Fuel Cells (SOFCs) use nonporous metal oxides to conduct oxygen anions (O^{2-}) by migration through the lattice of the crystal from the cathode to the anode side. Both MCFC and SOFC or high temperature fuel cells use the waste heat to raise system efficiencies or to enhance the reaction rate on non platinum-based catalysts.

In contrast, Polymer Electrolyte Fuel Cells (PEMFC) operate at low temperatures (80 °C) and then require platinum-based catalysts to promote the oxygen reduction reaction at the

cathode and the hydrogen oxidation reaction at the anode. However, PEMFCs offer the advantage of a rapid start-up from cold which is convenient for transportation applications. The first fuel cell powered bus, comprising 20 x 13 kW Ballard stacks and running on compressed hydrogen and air travelled in March 1998 in Chicago. During the last decade car constructors have mainly proposed fuel cell powered car prototypes with on-board stocked hydrogen fuel. Due to space limitations, an on-board reformer system, enabling the use of liquid fuel, e.g. methanol, and a subsequent CO clean-up unit has been incorporated in automotive fuel cells stacks. For instance, ddB Fuel Cell Engines have run a Mercedes A class, Necar 4 using 2 x 25 kW Ballard stacks fed with liquid hydrogen. Whereas the Necar 5 include an on-board methanol reformer and a CO clean-up unit [6]. Also, considering the increasing demand and requirement for portable devices (mobile phone, computer), the PEMFC offers a fair solution to the limited life time and efficiency of the actual rechargeable lithium battery.

Although high efficiency and freedom from pollution are well-rehearsed advantages of the fuel cell, it is currently more expensive than the conventional power plants such as gas turbines and diesel generators. Currently further technical improvements are required including developing less expensive construction materials, increasing the power for each cell, and scaling up the number of power plants sold in order to benefit from mass production and widespread exploitation.

As can be seen from the previous examples as well from the literature [7], the potential of PEMFCs to meet various commercial markets is rather large and significant for stationary power generation (rated up to several megawatts), portable (rated up to 100 W) and transportable (rated up to 5 kW) devices. However, the material cost of the components of PEMFCs slows down fuel cells commercialisation. For instance the graphite gas flow field plates are equal to 50% of the total cost and 90% of the total weight, while the ensemble membrane polymer electrolyte plus electrodes represent the other 50% of the total cost. The following section intends to overview progresses that have been realised to reduce stack costs over the past decades.

Type of Fuel Cell	Temp. / °C	Electrolyte	Reactions (Anode/Cathode) Catalyst	Fuel	Applications Power range
Alkaline (AFC):	80	KOH (liquid)	$H_2 + 2OH^- \Rightarrow 2H_2O + 2e^-$ *Anode: Ni, Ag, Pt, Pt/Au*	pure H_2	Space, transportation 1 kW to 100 kW
			$1/2O_2 + H_2O + 2e^- \Rightarrow 2OH^-$ *Cathode: Ni, Ag, Pt, Pt/Au*		
Molten Carbonate (MCFC)	650	Li_2CO_3/K_2CO_3 (liquid: melted salts)	$H_2 + CO_3^{2-} \Rightarrow H_2O + CO_2 + 2e^-$ *Anode: Ni, Ni/Cr*	natural gas petroleum	Stationary 500 kW to 10 MW
			$1/2O_2 + CO_2 + 2e^- \Rightarrow CO_3^{2-}$ *Cathode: Li/NO*		
Solid Oxide (SOFC)	750 to1000	ZrO_2/Y_2O_3 (solid)	$H_2 + O^{2-} \Rightarrow H_2O + 2e^-$ $CO + O^{2-} \Rightarrow CO_2 + 2e^-$ *Anode : Ni, Ni/ZrO_2*	Hydrocarbon mixture of H_2 and CO typically	Stationary 100 kW to 10 MW
			$1/2O_2 + 2e^- \Rightarrow O^{2-}$ *Cathode: In, $LaSrMnO_3$*		
Phosphoric Acid (PAFC)	200	H_3PO_4 (liquid)	$H_2 \Rightarrow 2H^+ + 2e^-$ *Anode : Pt*	natural gas, reformate	Transportable, stationary 200 kW to 10 MW
			$1/2O_2 + 2\,H^+ + 2e^- \Rightarrow H_2O$ *Cathode: Pt/Ni, Pt/CR/Co*		
Polymer Electrolyte Membrane (PEMFC)	80 (150)	Polymer (solid)	$H_2 \Rightarrow 2H^+ + 2e^-$ *Anode: Pt, Pt/Ru*	H_2 reformate (methanol)	Portable, transportable, stationary 1 W to 10 MW
			$1/2O_2 + 2\,H^+ + 2e^- \Rightarrow H_2O$ *Cathode: Pt*		

Table 1 : Main characteristics of the different type of fuel cells and their commercial applications.

3 POLYMER ELECTROLYTE FUEL CELLS (PEMFCS)

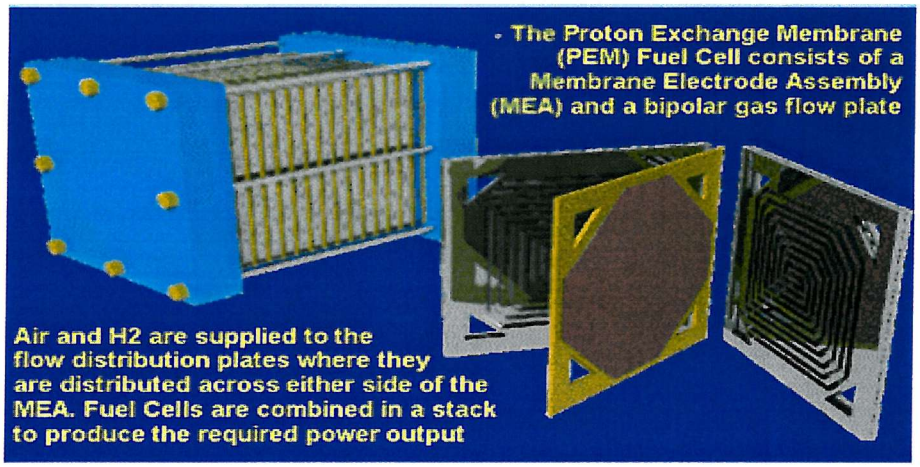

Figure 2 : Schematic of a Polymer Exchange Membrane Fuel Cell taken from the reference [8].

As the name implies, PEMFCs use a solid polymer as the electrolyte which is a proton conductor. Being a solid the electrolyte can not change, move about or vaporize from the system. Polystyrene sulfonate ion-exchange membranes experimented with by General Electric for the solid polymer electrolyte fuel cell in the Gemini spacecraft were not stable in the electrochemical environment. Degradation occured due to chemical attack by hydrogen peroxide, which is an intermediate compound of the oxygen reduction reaction. The success of the PEMFC came with the development of perfluorinated sulfonic acid polymers by Du Pont in 1970 and latterly by Dow Chemical Co. This polymeric chain consists of a polytetrafluoroethylene (PTFE) backbone with sulfonic pendant groups. The structural formula of such cation-exchange membrane is given in chapter two, section 5.1.1.1, page 30.

In addition to being stable in the aggressive fuel cell environment, the polymeric component is dispersible in some organic solvents, e.g. ethanol. This allows the thickness of the membrane to be modulated and the liquid form of the polymer to be used as a binder for carbon supported platinum particles. Though the latter point is discussed in the following paragraph, many groups have demonstrated the enhanced performance of PEMFCs when thin membranes were used [9].

Murphy *et al* have compared two Du Pont membranes, i.e. Nafion® 117 and 115 and a Dow membrane [10] with a given thickness of 178 μm, 127 μm and 100 μm, respectively. The

Dow membrane exhibited superior cell performance such that a high power density, e.g. 2.5 W cm^{-2} at a cell potential of 0.48 V and a current density of 5.1 A cm^{-2} was obtained, using unsupported and high platinum loading electrode. This was related to the higher water retention capability of the Dow membrane over Nafion® membranes as it contains more sulfonic acid groups per molecule. That, in turn, affects the ohmic resistance (R_i), e.g. 0.075 Ω cm^2 for Dow against 0.176 and 0.208 Ω cm^2 for Nafion® 115 and 117, respectively. Thereby, a low equivalent weight (defined as gram of polymer/mole of sulfonic acid group) optimises the water content of the membrane electrolyte polymer and therefore, increases the ionic conductivity. The membrane water level in the PEMFC contributes to the water management process. Subsequently, the second part of the water management strategy relies on the operating conditions such as pressure drop, temperature rise and reactant gas counter flow. Unadjusted parameters together with membrane contamination lead to improper water balance, such as cathode flooding, gas dilution or membrane dehydratation, which decreases the fuel cell performance, e.g. anode and cathode kinetic losses, mass transport limitations at high current densities and increase of the ohmic resistance [11]. The fuel cell performance will be described in chapter two, section 5.2. To prevent the membrane from being dehydrated, reactant gases are humidified prior to reaching the anode (hydrogen) and the cathode (air).

Since PEMFCs operate at low temperatures, platinum-based electrodes are used to promote the reduction of oxygen at the cathode, due to the slow kinetics of the reaction. Platinum has been recognised as the most active and stable material in the fuel cell environment. Hence, the increasing price of platinum over the past decade has motivated the lowering of the platinum loading on the electrodes. For instance, the early fuel cell prototypes used Pt black at a loading of 4 mg Pt cm^{-2} [12]. Recently, high fuel cell performance were obtained using low catalyst loading, e.g. 0.5 mg Pt cm^{-2} and even ultralow platinum loading, e.g. 0.05 mg Pt cm^{-2} on the electrodes [13]. In this context, many groups have purposely sought higher surface area catalysts such as small platinum particles (2 nm to 3 nm) dispersed on carbon.

A key issue of the investigation of the low loading platinum electrode was then to bring the catalyst into contact with the solid polymer electrolyte. This was achieved by impregnation of the active catalyst area with a soluble form of polymer to increase the protonic conductivity and thus, permitting efficient use of low platinum loading materials over a volume (geometric area × thickness of the electrode). This process was initiated by Los

Alamos National Laboratory (LANL) and the Texas A&M University (TAMU) [14]. LANL achieved the deposition of a mixture of carbon supported catalyst with a Nafion® solution onto the polymer membrane electrolyte. A microporous gas diffusion backing layer or substrate, namely carbon cloth, was compressed onto the catalyst layer to remove the product, water, from the cathode. At TAMU, the supported catalyst was firstly impregnated with a PTFE (polytetrafluoroethylene) binder and deposited onto the electrode substrate. Subsequently, the membrane polymer electrolyte was compressed onto the catalyst side. These two techniques led to platinum loading on the cathode electrode as low as 0.12 and 0.05 mg Pt cm^{-2}, respectively. The attempt of chemical deposition of a platinum salt directly onto the membrane polymer gave rise to higher platinum loadings such as 1 mg Pt cm^{-2} and a lower dispersion of the platinum. Thereby, the success of low loading platinum on electrodes can most readily be obtained by the use of platinum supported carbon catalysts.
Currently, such electrodes are prepared with catalysts containing a nominal platinum loading of 10 to 40 wt.% Pt on carbon. If ultralow loading of Pt on the final electrode is attempted with the 10 wt.% Pt/C catalyst, the electrode thickness is rather high and may cause life time deterioration. Modelling as well as practical studies have indicated a limited thickness of the catalyst layer utilisation. LANL estimated 5 μm [15] and TAMU indicated 10 μm [16] thick active layer catalyst for their electrodes. Ultra-low loadings of platinum were obtained by electrochemical deposition of a platinum salt onto a porous carbon support pre-layered with a mixture of carbon black and a solution of polymer [17]. This technique allows the deposited platinum to benefit from a good ionic contact with the solid polymer electrolyte and a good electronic contact with the carbon support. However, the platinum electrodeposition may cause difficulties with mass production.

Based on the LANL and TAMU methods, Ralph *et al* have measured comparable performances for a PEMFC using a high catalyst loading MEA, e.g. 8 mg Pt cm^{-2} prepared with Pt black, and a low platinum loading membrane electrode assembly (MEA), e.g. 0.62 mg Pt cm^{-2} prepared with 40 wt. % Pt/C at the cathode and 20 wt. % Pt, 10 wt. % Ru/C at the anode. At a cell potential of 0.75 to 0.65 V the MEA generates 0.4 to 0.8 mA cm^{-2} equivalent to 0.3 to 0.5 W cm^{-2} [9].
When operating on pure hydrogen, a platinum loading as low as 0.025 mg Pt cm^{-2} on the anode electrode is sufficient to sustain high current densities [18]. This is due to the facile nature of the hydrogen oxidation reaction. Thereby, the decrease of the catalyst loading on the anode electrode is not a technical challenge.

If stationary power plant and light duty transportable devices are to use PEMFCs for electrical power generation, liquid fuel is seen as more convenient than gaseous pure hydrogen. This is explained by higher requirement for performance as well as insufficient space to store H_2 on-board. Although hydrogen rich fuel may be obtained by reforming fossil fuels such as methanol, gasoline or other hydrocarbons (Equation 4), impurities are invariably present in the fuel stream, e.g. CO up to 2.5 % and CO_2 between 20% to 25% by volume.

$$CH_4 + H_2O \rightarrow 3H_2 + CO \qquad \text{Equation 4}$$

While CO_2 is mostly present as diluant of the H_2 fuel content, the trace level of carbon monoxide (CO) poisons the platinum sites which are available for the hydrogen oxidation reaction at the anode. Thus, the performance of the cell is largely reduced for CO levels as low as 30 ppm [19]. Subsequently, the system requires a water gas shift reactor or preferential oxidation reactor to reduce the level of CO to ppms. Thus, the remaining CO is oxidised into CO_2 and H_2 (Equation 3). However, this process increases the cost, the weight and the complexity of the mechanical engineering of the fuel cell. The initial flexibility of the fuel cell can be kept with the direct supply of a liquid fuel such as methanol which is readily oxidised at the anode according to the Equation 5.

$$CH_3OH + H_2O \rightarrow CO_2 + 6H^+ + 6e^- \qquad E_o = 0.046 \text{ V vs. NHE} \qquad \text{Equation 5}$$

As methanol is easily transported, stored and alterated to accommodate power changes, the Direct Methanol Fuel Cell (DMFC) is rather competitive for transportable applications [20]. However, the slow kinetics of the anode reaction dictates that DMFCs operate at higher temperatures than conventional PEMFCs, eg. 150 °C. In addition, the dehydrogenation reaction of methanol (Equation 5) involves different adsorption steps, facile on platinum, with the formation of chemisorbed residues that decrease the catalytic activity of the platinum electrode surface. These steps are detailed from Equation 6 to Equation 9. The main poisoning species are recognised as linearly or bridged bonded CO [21]. Subsequently, an oxygen transfer reaction to Pt-CO species is believed to produce CO_2. However, this oxidation reaction rate is slow at the potential range (below 450 mV) [20], where methanol

adsorbs onto the surface. Therefore, efforts have been made in order to search for a catalyst that could lower the potential of the CO oxidation reaction.

$$CH_3OH \rightarrow CH_2OH + H^+ + e^- \quad \text{Equation 6}$$

$$CH_2OH \rightarrow CHOH + H^+ + e^- \quad \text{Equation 7}$$

$$CHOH \rightarrow COH + H^+ + e^- \quad \text{Equation 8}$$

$$COH \rightarrow CO + H^+ + e^- \quad \text{Equation 9}$$

In addition, the permeability of the perfluorosulfonic acid membrane to methanol gives rise to high fuel crossover towards the cathode side. The latter phenomenom results in a cathode overpotential and thereby, a reduction of the performance and efficiency of the fuel cell.

The addition of an air bleed directly to the hydrogen rich fuel stream enables the decrease of the level of CO well below 10 ppm. However, the exothermic nature of the gas phase reactions (e.g. oxidation of CO and H_2 by O_2) degrade the catalyst (sintering) and the membrane. Therefore, the most elegant alternative to the use of an air bleed is the development of CO tolerant electrocatalysts capable of operating in the presence of at least 100 ppm CO. Over the past decades, many groups have sought for inexpensive and highly active electrocatalysts for the electrochemical reactions at the electrode surfaces. Binary and ternary alloys that combine Pt with first row transition metals (Cr, Mn, Ni, Fe, Co) enhanced the catalytic capabilities of the electrocatalyst. In addition, these materials can maintain their chemical and physical integrity for long time periods in the hostile fuel cell environment (e.g. operating temperature and electrolyte).

4 ADVANCED MATERIALS USED FOR THE ELECTRODES IN THE PEMFCS

As can be seen from the previous examples, the presence of CO affects significantly the performance of the platinum electrocatalyst and, thereby, the performance of the fuel cell. CO can be either present initially in the reformated fuel stream or produced directly from the oxidation of methanol at the anode. Molecules of CO block and decrease the number of platinum sites available for the reaction at the anode. Subsequently, this phenomenon

increases the activation overpotential (i.e. voltage losses) that, in turn, affects the current-voltage curve. (The characteristic curve of the fuel cell performance can be seen in detail in chapter 2, figure 8). To overcome the CO poisoning effect, researchers focused on the limitations of the electrocatalyst to improve the CO tolerance of fuel cells anodes. By combining a secondary element with platinum [22], one would expect the intrinsic properties of the electrocatalyst to be changed or the oxidation of CO into CO_2 to be promoted at lower potential than that obtained with pure platinum. Therefore, the modification of the platinum enables the design of the electrocatalyst according two separate concepts:

- the incorporation of a first row transition metal (e.g. Ru, Rh, Sn, Fe, W, Mo, etc...) to the small platinum particles to form an alloy phase
- the association of a metal oxide (e.g. SnO_3, WO_3, etc...) to the small platinum particles supported on carbon

A number of groups have reported improvement of the activity for CO [23] and methanol [24] oxidation when Pt alloy electrocatalysts were used as anode fuel cells. In the early seventies, Ross *et al.* reported the enhanced activity of Pt-Rh supported on graphitised carbon for the hydrogen oxidation in CO/H_2 mixtures (1.7 % CO in H_2). They related this result to an increase of the d-band vacancy for the alloy rather than considering this catalyst as CO-tolerant [25]. Complementary electrochemical investigation pursued with Pt-Ru supported on graphitised carbon demonstrated the tolerance of this alloy to poisoning by CO [26]. The CO coverage was seen to decrease with increasing Ru content as well as varying with the temperature and the electrode potential. In addition to the oxidation of CO, the enhancing effect of Ru was observed for the oxidation of methanol. This is consistent throughout the various preparation methods used such as alloying, electrodeposition [27,28], as well as carbon supported and unsupported dispersed particles [29]. In contrast, Sn can be recognised as good candidate for CO oxidation [23] but is a rather inefficient promotor for methanol oxidation. Moritomo *et al.* have attributed this inconsistency to the susceptibility (instability) of both the Sn in the potential range and the morphology of the platinum surface [24].

However, within a wide range of Pt alloy electrocatalysts examined as anode fuel cell electrodes, the Pt-Ru alloy was recognised as the most efficient electrocatalyst for both CO and methanol oxidation reactions. As can be seen in the previous examples, as well as in the

literature, there has been much debate about the reasons why Pt alloys provide higher activity for CO and/or methanol oxidation. The most likely are defined as follows [22]:

- the modification of the electronic nature of the surface and thereby, the weakening of the chemical bond between platinum and the surface intermediate, namely CO
- the modification of the physical structure or a more favourable Pt-Pt interatomic distance
- the surface roughening by preferential leaching of the secondary metal leaving a highly reticulated and active surface. These extented step sites provide additional adsorption sites for the methanol electroreduction. The oxidation of these lo-coordinate sites give rise to Pt-OH_{ads} at lower potentials.
- the preferential adsorption of anions or water activation on the secondary metal that can take part in the main oxidation process. The secondary metal can donate OH_{ads} to adjacent Pt sites through a spillover process. This occurs at lower potentials than those at which platinum is usually oxidised.

While the role of the alloy has been clearly stated, no conclusive mechanism regarding CO and/or methanol electrooxidation on the surface of Pt alloy supported catalysts has been specifically described yet. This is explained by the poor surface characterisation, in terms of the real surface area (i.e. distinction between metal oxides and pure metallic phase) and in terms of metal surface composition. Nevertheless, two models have been suggested, a *promoted* mechanism and an *intrinsic* mechanism [30]. The latter case postulates that the presence of the secondary element modifies H_2 and CO chemisorption properties, so as to reduce CO coverage with respect to H_2 oxidation sites. The promoted mechanism is based on CO oxidation at low potentials. Earlier, Watanabe *et al.* have suggested the bifunctional mechanism of the activity enhancement for methanol oxidation on platinum by ruthenium ad-atoms [28]. In this mechanism Ru nucleates oxygen containing species due to the preferential water activation on Ru atoms, (Equation 10) at lower potential than on Pt. These species in turn, oxidise the CO-like species adsorbed on the neighbouring Pt atoms (Equation 11). This mechanism resulted from studies on well-characterised Pt-Ru alloy surfaces [31,32].

$$Ru + H_20 \rightarrow Ru\text{-}OH + H^+ + e^- \qquad \text{Equation 10}$$

$$Ru\text{-}OH + Pt\text{-}CO \rightarrow Ru + Pt + CO_2 + H^+ + e^- \qquad \text{Equation 11}$$

Although the bifunctional mechanism was recognised to perform the bimolecular oxidation reaction of CO to CO_2, the optimum Ru surface composition was determined according to the anode oxidation reaction or the type of adsorbate. A 50 at.% Ru surface composition provides a large number of Pt-Ru pairs, that enables CO adsorbed onto Pt and Ru sites to readily migrate from these sites to Ru oxide containing species sites. Whereas a 10 at.% Ru surface composition optimises the oxidation of CO-like species produced from the methanol dehydrogenation reaction (Equation 5). That is, a threefold Pt ensemble enables the initial methanol adsorption whereas Ru sites initiate only the water activation.

The electrochemical investigations described above were done on individual surface planes and well-defined surface alloy composition. Such studies are useful, but insufficient to understand the higher catalytic activity of supported Pt alloy catalyst used in the fuel cell electrode. Highly dispersed platinum catalysts have been investigated using transmission electron spectroscopy and X-ray crystallography and have been found to consist of Pt crystallites which are comprised of an amalgam of planes [33]. This surface arrangement corresponds to the lowest surface energy.

A key issue was then the method of preparation of supported platinum (and platinum alloy) catalysts including the subsequent treatment in reducing atmospheres to control the morphology of the particles (i.e. crystallite size), the alloy formation (i.e. phase) and composition, as well as the porosity and purity of the carbon support. There has been much debate regarding the effective impact of the crystallite size of the platinum nanoparticle on the kinetics of PEMFCs electrode reactions. For example, Kabbabi *et al.* observed a loss of catalytic activity with decreasing Pt particle size for the oxygen reduction reaction (ORR) and methanol oxidation. They correlated these results to the stronger adsorption of oxygenated species and to the more difficult CO oxidation [34]. More recently, measurements of the kinetic performance of a series of cathodes prepared from unsupported Pt black and 40wt.% Pt electrocatalyst on different carbon supports have confirmed the role of oxide stability. The decreased Pt crystallite size was observed when incorporating the C support and accordingly to the type of carbon support used [35]. The existence of the particle size effect in PEMFCs was extended to the Pt alloy where a reduction in size accompanied higher catalytic activity.

Hydrophobic character of the carbon also has to be taken into account where the presence of oxidised complexes on its surface could modify the wettability properties during the impregnation support with the metal precursors in polar media. Moreover, the modification of the surface chemistry of the carbon by activation treatments can produce a noticeable

effect on the metal precursor/support interaction. The beneficial effects of the activation treatments on the catalytic activity appear to depend on the type and the amount of the complexes developed on the carbon surface [36]. For example, oxidation of the carbon support to produce an acidic functionality increases the catalytic activity for the methanol electro-oxidation reaction [37].

Aiming to a single alloy phase for carbon supported Pt alloy is a difficult task. Mc Breen *et al.* starting from an atomic ratio of Ru to Pt of 3.4:1 on carbon, found a large excess of unalloyed Ru, with only about 10% of the Ru alloyed with the Pt [38]. Antolini and co-workers studied physical and morphological characteristics of PtRu/C using X-Ray Diffraction (XRD), transmission electron microscopy (TEM), specific surface area analysis (BET) and X-Ray photoelectron spectroscopy (XPS). They have concluded that a strong metal/carbon support electronic interaction was present which hindered the formation of a single phase face centered cubic (fcc) PtRu alloy. Parallel PEM fuel cell tests in H_2/air operation mode have shown decreased fuel cell performance due only to the dilution of Pt atoms with respect to C, at a fixed Pt loading. In 100 ppm CO in H_2 operation mode the highest fuel cell performance was seen for 0.63 atomic fraction Ru comprising two solid solutions, fcc and hexagonal cubic centered (hcc) [36].

Since there is no possible structure predetermination, *in situ* spectroscopic experiments for supported platinum fuel cell electrocatalysts seem the most appropriate. X-ray absorption spectroscopy (XAS) using the synchrotron radiation source is a powerful technique that propelled to a realistic dimension structural investigations of amorphous materials such as those generally used in fuel cells systems.

5 XAS STUDIES

X-ray absorption spectroscopy appears as the most promising technique to investigate both structural and electronic changes of carbon supported platinum (and Pt alloy) fuel cell catalysts under electrochemical control with element specificity. *In situ* XAS spectra recorded at the Pt L_{III} and L_{II} edges and at the K edge of the alloying element enable determination of the electrode structure under conditions more closely related to the fuel cell

environment (e.g. acidic medium, variation of potential and poisoning conditions in presence of CO and methanol).

Although this technique will be described in more detail later in this thesis, its main characteristics are summarised in the following paragraph. The XAS spectrum can be divided clearly in two parts. The extended X-ray absorption fine structure (EXAFS) part of the spectrum (the post-edge region) provides detailed structural information, *i)* regarding the particle size and composition, by determination of the number of neighbours, *ii)* regarding the lattice contractions, by determination of the inter-atomic distances, and *iii)* regarding the particle/substrate interactions by determination of the type of neighbours. The X-ray absorption near edge structure (XANES) part of the spectrum (the near edge region) enables the determination of the Pt oxidation state by comparing the Pt L_{III} and the Pt L_{II} edges.

During last decade, a number of authors have reported the efficacy of *in situ* XAS experiments for study of fuel cell electrode formulated with carbon supported platinum and bimetallic catalysts. Herron *et al.* demonstrated the chemisorbed nature of the adsorbed oxygen atoms by applying oxidation potential to a Pt/C fuel cell electrode [39]. The absence of bulk-oxide-like Pt-Pt coordinations at distances larger than 2.01 Å together with the existence of a large fraction of Pt atoms still coordinated in a metallic fcc structure, indicates that only a thin oxide was formed at the surface of the platinum particles at higher electrode potentials. Furthermore, changes in the Pt oxidation state were directly observed with the increase of the height of the threshold peak at the Pt L_{III} edge when sweeping the electrode potential towards more oxidative potentials to reach the Pt oxide formation (Equation 12).

$$Pt + H_2O \rightarrow Pt\text{-}O + 2H^+ + 2e^- \qquad E_o = 0.88 \text{ V vs. NHE} \qquad \text{Equation 12}$$

Furthermore, the XAS technique has provided a wealth of useful information regarding the influence of alloy formation on the structure and electronic properties of the metal particles. For example, Mukerjee *et al.* have reported both contractions in the Pt-Pt inter-atomic distance and higher *d*-band vacancies per Pt atom at a potential in the double layer region for a series of alloys (PtCr, PtFe, PtCo or PtNi) [40]. Also, the analysis of XAS data for oxygen reduction reaction by alloys revealed the increase of the *d*-band vacancies and the absence of a Pt-O inter-atomic distance in the fit model at potentials where oxides form on Pt. They attributed the enhanced electrocatalysis for oxygen reduction by alloys to the electronic and geometric properties of the alloys together with the preferential

chemisorption of OH species by the alloying element. Other *in situ* XAS studies were concerned with the H_2 oxidation by alloys [41], methanol electrooxidation [42] and CO oxidation. For example, *in situ* XANES studies performed at the Ru K edge for the CO electrocatalysis by PtRu/C at a Pt:Ru atomic ratio of 1:1 evidenced electronic changes (i.e. edge feature changes) of Ru atoms when exposed to CO. At oxidative potentials (e.g. +0.8 V vs. RHE) a much lower state of oxidation for Ru was observed for Ru atoms in presence of CO than that recorded in inert gas atmosphere. The authors suggested the rate determining step (rds) of the CO oxidation reaction of such PtRu as the oxidation of the Ru surface (Equation 10).

6 PROJECT AIMS AND OBJECTIVES

As seen in the brief review presented above, a key issue for the widespread use of the fuel cell technology is the design of the carbon supported Pt-based fuel cell electrocatalyst. Carbon supported PtRu is the state-of-the-art electrocatalyst as it improves greatly the fuel cell performance over that found for platinum. However, the mechanism by which this phenomenom occurs has not be clearly stated yet. This thesis attempts to establish more closely the impact of the secondary metal element on the structure of the carbon supported Pt particles and to the catalytic properties of the electrocatalyst. Specifically, the CO and methanol electrooxidation reactions were investigated.

The chemical reduction of metal salts under specific experimental conditions leads easily to platinum-based catalysts. The characterisation of the extent of formation of the alloy is currently performed by using the X-ray diffraction technique. In this thesis, the use of EXAFS in identifying the extent of alloy formation will be presented. The specific example of Pt-Ru will be presented in Chapter 3 as an illustration.

Chapter 4 deals with a comparative and detailed structural investigation for carbon supported Pt, Pt-Ru and Pt-Mo electrocatalysts. This study was completed at the Pt and the M adbsorption edges, with M corresponding to Ru or Mo. In addition, the ability to measure EXAFS spectra as function of the potential provides information as the electrode is oxidised or reduced.

In chapter five the influence of the CO adsorbed species on the carbon supported platinum particles will be presented by means of the *in situ* EXAFS technique.

The final part of the thesis seeks to correlate the structural and morphological changes that have been observed throughout EXAFS studies to the catalytic properties of the fuel cell material determined by electrochemical tests in a half cell as well as under real fuel cell conditions.

7 REFERENCES

[1] Hoogers, G., *Physics World,* **1998**, 31.

[2] Bockris, J. O. M.; Srinivasan, S., *Fuel Cells: their electrochemistry*; McGraw-Hill, Inc: New York, 1969.

[3] Hamnett, A., *Phil. Trans. R. Soc. Lond. A,* **1996**, *354*, 1653.

[4] Acres, G. J. K.; Hards, G. A., *Phil. Trans. R. Soc. Lond. A,* **1996**, *354*, 1671.

[5] Ralph, T. R., *Platinum Metals Review,* **1999**, *43*, 14.

[6] Cameron, D. S., *Platinum Metals Review,* **1997**, *41*, 171.

[7] Cells and marketing In *Automotive engineer*, 1997; 97.

[8] http:\\www.johnsonmatthey.com

[9] Ralph, T. R., *Platinum Metals Review,* **1997**, *41*, 102.

[10] Murphy, O. J.; Hitchens, G. D.; Manko, D. J., *J. Power Sources,* **1994**, *47*, 353.

[11] St-Pierre, J.; Wilkinson, D. P.; Knights, S.; Bos, M. L., *J. New Materials for Electrochemical Systems,* **2000**, *3*, 99.

[12] Prater, K., *J. Power Sources,* **1990**, *29*, 239.

[13] Appleby, A. J., *Phil. Trans. R. Soc. Lond. A,* **1996**, *354*, 1681.

[14] Dhar, H. P., *J. Electroanal. Chem.* **1993**, *357*, 237.

[15] Springer, T. E.; Wilson, M. S.; Gottesfield, S., *J. Electrochem. Soc.,* **1993**, *140*, 3513.

[16] Ticianelli, E. A.; Berry, J. G.; Srinivasan, S., *J. Appl. Electrochem.,* **1991**, *21*, 597.

[17] Taylor, E. J.; Anderson, E. B.; Vilambi, N. R. K., *J. Electrochem. Soc.,* **1992**, *139*, L45.

[18] Hards, G. A.; Ralph, T. R.; Cooper, S. J. "High performance, low cost membrane electrode assemblies for solid polymer fuel cells," ETSU Report ETSU/FCR/002, Dec. 92.

[19] Cooper, S. J.; Gunner, A. G.; Hoogers, G.; Thompsett, D. In *Proceedings of the 2nd International Symposium on New Materials for fuel cells and modern battery systems*; O.Savadogo, P. R., Ed.: Montreal, Canada, 1997; pp 286.

[20] Hogarth, M. P.; Hards, G. A., *Platinum Metals Review,* **1997**, *40*, 150.

[21] Leger, J. M.; Lamy, C., *Berichte Der Bunsen-Gesellschaft-Physical Chemistry Chemical Physics,* **1990**, *94*, 1021.

[22] Parsons, R.; VanderNoot, T., *J. Electroanal. Chem.,* **1988**, *257*, 9.

[23] Morimoto, Y.; Yeager, E. B., *J. Electroanal. Chem.,* **1998**, *441*, 77.

[24] Morimoto, Y.; Yeager, E. B., *J. Electroanal. Chem.,* **1998**, *444*, 95.

[25] Ross, P. N.; Kinoshita, K.; Scarpellino, A. J.; Stonehart, P., *J. Electroanal. Chem.*, **1975**, *59*, 177.

[26] Ross, P. N.; Kinoshita, K.; Scarpellino, A. J.; Stonehart, P., *J. Electroanal. Chem.*, **1975**, *63*, 97.

[27] Watanabe, M.; Motoo, S., *J. Electroanal. Chem.*, **1975**, *60*, 275.

[28] Watanabe, M.; Motoo, S., *J. Electroanal. Chem.*, **1975**, *60*, 267.

[29] McNicol, B. D.; Short, R. T., *J. Electroanal. Chem.*, **1977**, *81*, 249.

[30] Hoogers, G.; Thompsett, D., *Cattech*, **2000**, *3*, 106.

[31] Gasteiger, H. A.; Markovic, N.; Ross, P. N.; Cairns, E. J., *J. Phys. Chem.*, **1994**, *98*, 617.

[32] Gasteiger, H. A.; Markovic, N.; Ross, P. N.; Cairns, E. J., *J. Phys. Chem. B*, **1993**, *97*, 12020.

[33] Stonehart, P., *Electrochemistry and Clean Energy*, **1994**, *146*, 16.

[34] Kabbabi, A.; Gloaguen, F.; Andolfatto, F.; Durand, R., *J. Electroanal. Chem*, **1994**, *373*, 251.

[35] Ralph, T. R.; Hogarth, M. P., *Platinum Metals Review*, **2002**, *46*, 3.

[36] Antolini, E.; Giorgi, L.; Cardellini, F.; Passalacqua, E., *J. Solid State Electrochem.*, **2001**, *5*, 131.

[37] Frelink, T.; Visscher, W.; Van Veen, J. A. R., *J. Electroanal. Chem*, **1995**, *382*, 65.

[38] McBreen, J.; Mukerjee, S., *J. Electrochem. Soc.*, **1995**, *142*, 3399.

[39] Herron, M. E.; Doyle, S. E.; Pizzini, S.; Roberts, K. J.; Robinson, J.; Hards, G.; Walsh, F. C., *J. Electroanal. Chem*, **1992**, *324*, 243.

[40] Mukerjee, S.; Srinivasan, S.; Soriaga, M. P.; McBreen, J., *J. Electrochem. Soc.*, **1995**, *142*, 1409.

[41] Mukerjee, S.; McBreen, J., *J. Electrochem. Soc.*, **1996**, *143*, 2285.

[42] Mukerjee, S.; McBreen, J., *J. Electroanal. Chem.*, **1998**, *448*, 163.

CHAPTER TWO : EXPERIMENTAL AND TECHNIQUES

This chapter gives detailed information on the theory and practical aspects of the techniques used in this project. Electrode fabrication, cyclic voltammetry, polarisation, single cell fuel cell testing and X-Ray Absorption Spectroscopy are covered.

1 REAGENTS AND MATERIALS

Table 1 lists the chemical reagents and materials used with their respective suppliers.

Reagent / Material	Supplier
Platinum supported on Carbon	Johnson Matthey
Platinum-Ruthenium supported on Carbon	Johnson Matthey
Platinum-Molybdenum supported on Carbon	Johnson Matthey
Vulcan XC-72R carbon black	Cabot Corporation
Nafion® solution (5 wt. %) in an alcoholic solution	Aldrich
Nafion® -115 and –117 membranes	Aldrich
Carbon paper - TGHP-090	E-TEK, Inc

Table 1: Materials and reagents.

Ion exchange treated water with a conductivity of 10^{18} MΩ cm was used for the electrode fabrication and the electrochemical tests.

2 ELECTRODES

Electrodes are the sites for the electrochemical reactions to take place. As the reactants used in Polymer Electrolyte Membrane Fuel Cells (PEMFCs) are usually gaseous, the development of porous *gas diffusion electrodes (GDE)* has enabled significant breakthroughs in fuel cell technology. The principal function of a porous gas diffusion electrode is to provide a large reaction zone with a minimum of mass transport limitation for

the access of reactants and the removal of products. Therefore, such high surface area electrodes deliver a current load scaled in amperes per cm^2 compared to smooth platinum surface in microamperes per cm^2.

Fuel cell electrodes normally have a backing layer, which is usually carbon fibre paper or woven carbon cloth, supporting the catalyst layer. The carbon support acts as a current collector and also allows gaseous reactants to diffuse through the pores towards the catalyst layer. To prevent water molecules from accumulating within the pores and thus limiting the diffusion of reactant gases (e.g. oxygen at the cathode), the carbon support can be coated with a hydrophobic substrate, e.g. polytetrafluoroethylene (PTFE) at about 12 weight percent. The chemical structure of the PTFE is given by $-(CF_2-CF_2)_n-$. The *wet proofing* of the electrode enhances the contact between catalyst, reactant gases and electrolyte. This so-called *three-phase zone* can be enlarged with the incorporation of metal powders with a high specific area such as carbon black, 200 to 250 $m^2\ g^{-1}$. The carbon black crystallises (graphitises) from its amorphous state after being heat treated in an inert gas (nitrogen). The enhanced long range order improves the electronic conductivity [1]. Chemically inert carbon is also a suitable support for catalyst deposition such as platinum. The large surface area of the carbon enables a better dispersion of the catalyst avoiding sintering of the particles. To function, the catalyst must be in contact with both the electronic (e.g. carbon) and protonic conductor. The proton conduction is optimised when the supported catalyst is impregnated with a solution of Nafion®, which is described further in section 5.1.1.1.

2.1 Preparation of Nafion® -bonded electrodes - Type A- solvent free ink

A small quantity of purified water and the required amount of an aqueous Nafion® solution (i.e. 50 weight percent equivalent catalyst) were added to the catalyst powder. The mixture was then dispersed using a blender for 15 minutes until an ink-like paste was obtained. The slurry was then screen-printed onto Carbon base-layered Carbon paper and pressed at 3 bars for 20 seconds at room temperature. The catalyst loading (i.e. 0.2 to 0.3 mg Pt cm^{-2}) was determined by weighing the electrode before and after the ink application. Electrodes of 1 cm^2 and 50 cm^2 were cut from this compacted sheet to be tested electrochemically in a wet cell and in a single cell fuel cell, respectively.

2.2 Preparation of Nafion® -bonded electrodes – Type B

A weighed quantity of catalyst powder was suspended in a small quantity of purified water with the required amount of an alcoholic Nafion® solution (i.e. 15 weight percent equivalent catalyst) and dispersed in an ultrasonic bath for 2 hours until an ink-like paste was obtained. The slurry was then spread manually onto a carbon paper current collector and hot-pressed at 10 bars for 3 minutes at 100 °C. Electrode buttons of 2.5 cm^2 were cut from this compacted sheet to be studied in EXAFS. In order to get an edge jump (defined later) of 0.3 to 0.6 in the EXAFS spectra the electrode loading was about 5 mg Pt cm^{-2}.

3 CATALYSTS

The catalysts used in this thesis were provided by Johnson Matthey and were prepared using a proprietary method [2]. This process involves aqueous deposition followed by chemical reduction steps.

4 ELECTROCHEMICAL TECHNIQUES AND APPARATUS

The techniques described below have been applied to half-cell measurements, i.e. anode, and fuel cell membrane electrode assemblies. Further detailed information can be found elsewhere [3], [4].

4.1 Electrochemical cell

Half-cell experiments have been conducted using a standard three-electrode glass cell, as illustrated in Figure 1. The reference electrode (Mercurous/Mercurous Sulphate (MMS) = 0.65 V vs. Reversible Hydrogen Electrode (RHE)) is in close proximity to the working electrode by a luggin capillary and a platinum gauze acts as a counter electrode. The electrodes were then immersed in 180 cm^3 of sulphuric acid (1 mol dm^{-3}) and the

experiments were conducted at 80 °C. The potentials reported in this thesis are referenced towards the MMS reference electrode, which was standardised towards RHE electrode.

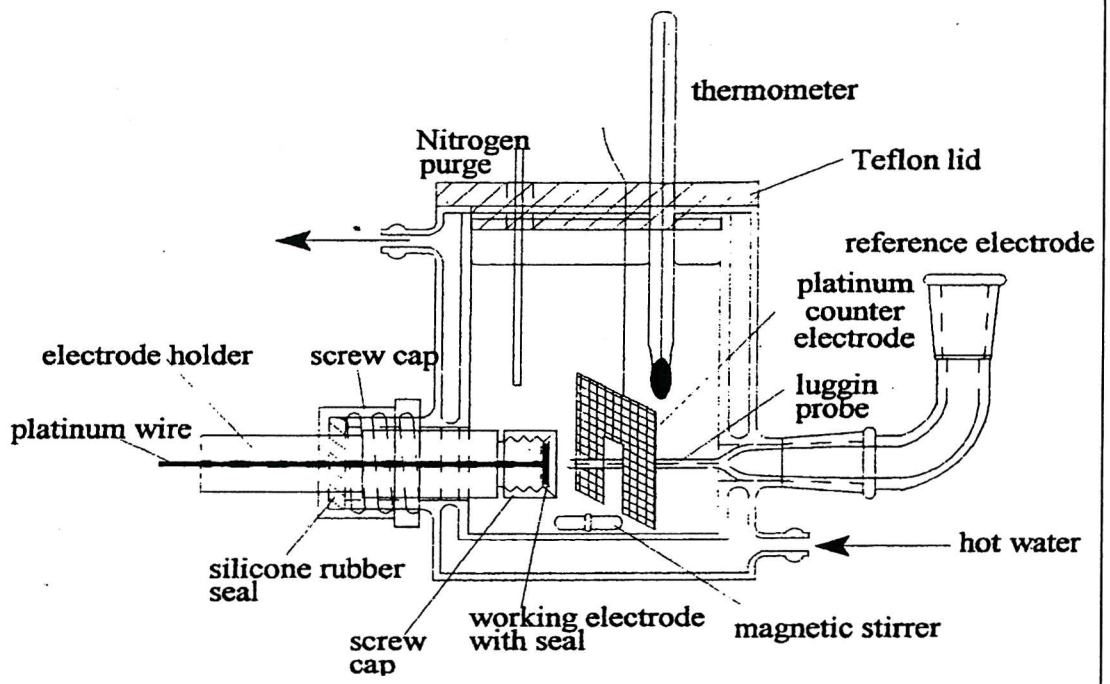

Figure 1: Scheme of the three electrode glass cell taken from reference [5].

4.2 Cyclic voltammetry

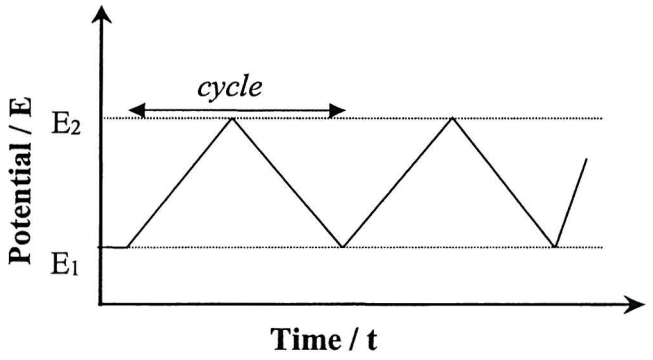

Figure 2: Variation of the applied potential as a function of time in a cyclic voltammetry experiment.

Cyclic voltammetry measures the current response (*I*) of the electrode under study as a function of the applied potential (*E*) using a potentiostat. The potential of the working

electrode is swept from E_1 to E_2 and back to E_1 at a scan rate (ν), as illustrated in Figure 2. At a corresponding oxidation or reduction potential electrochemical reactions occur involving a charge transfer to or from the working electrode and therefore, a current flow. This method was used to determine the oxidation potential of carbon monoxide on different supported Pt-based catalysts and to evaluate the electrochemically active surface area of the fuel cell electrodes. Before the development of these latter two points, a typical Pt cyclic voltammogram (CV) will be discussed in the following section.

4.2.1 A typical Platinum cyclic voltammogram

Figure 3 illustrates the CV of a Pt/C electrode when cycled in a solution of sulfuric acid. The electrochemical reactions that occur on the Pt sites are labelled in the figure and the corresponding equations are given in Table 2.

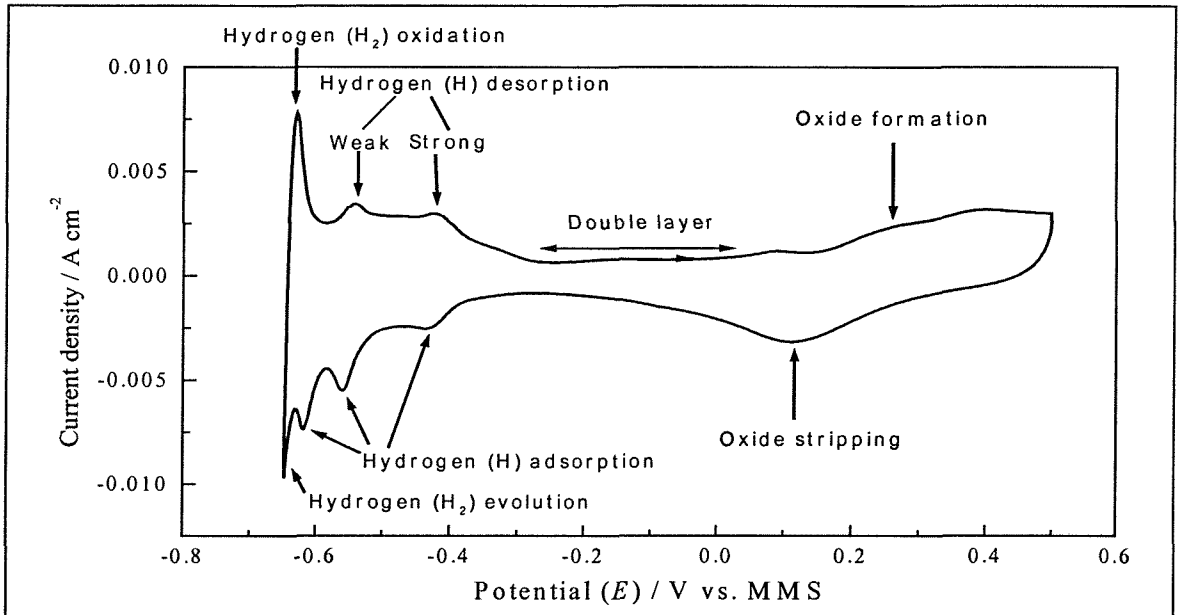

Figure 3: Cyclic voltammogram of a Pt/C electrode (electrode area 1 cm^2) cycled at 10 mV s^{-1} at 80 °C in 1 mol dm^{-3} H_2SO_4.

Hydrogen Adsorption / Desorption or hydride region:			
$Pt + H^+ + e^-$	⟷	$Pt\text{-}H_{ads}$	Equation 1
Hydrogen evolution			
$2H^+ + 2e^-$	⟷	H_2	Equation 2
Oxide formation/stripping:			
$Pt + H_2O$	⟷	$Pt\text{-}OH_{ads} + H^+ + e^-$	Equation 3

Table 2: Electrochemical reactions corresponding to a Pt/C electrode cycled in an acidic medium.

4.2.2 Evaluation of the Platinum Surface Area

The active platinum surface area was calculated from two different points of view. On one hand, the electrode platinum surface area (EPSA) enables one to evaluate the platinum area potentially available for the fuel cell reactions. On the other hand, the ElectroChemical Area (ECA) will reflect the platinum utilisation.

4.2.2.1 Practical procedure

A button electrode (1 cm^2) was boiled in triply distilled water prior to electrochemical studies to ensure a fully flooded state and placed in the glass electrochemical cell (Figure 1). The system was purged with nitrogen to remove oxygen from the system and, therefore, to prevent current produced by the oxygen reduction reaction from interfering with the reactions under study. The electrode potential was then swept from - 0.65 to 0.5 V vs. MMS at 10 mV s^{-1} until a stable cyclic voltammogram (similar to the one presented in Figure 3) was obtained. The potential was controlled by the Autolab potentiostat system.

The electrode potential was then held at - 0.55 V vs. MMS as carbon monoxide was bubbled directly through the electrolyte solution for 15 minutes. A successive nitrogen purge for 30 minutes was required to remove CO from the solution. Then, cyclic voltammograms were recorded between - 0.65 V and 0.5 V at a scan rate of 10 mV s^{-1}. A higher sweep rate would give rise to a larger pseudo-capacitance in the cyclic voltammogram. The characteristic features of the CVs are illustrated in Figure 4.

The absence of the hydride region in the potential range of - 0.55 V to - 0.3 V verifies that CO has poisoned the platinum electrode surface, as shown in Figure 4, first scan. As the potential rises from – 0.55 V to 0.5 V carbon monoxide leaves the electrode surface. A current flow, corresponding to a 2 electron charge transfer involved in the CO oxidation, is visible from 0 V up to 0.2 V, as shown in Figure 4, first scan. In this process, CO linearly bonded and / or bridge bonded reacts with water molecules from the solution to give CO_2, according to Equation 4 and Equation 5, respectively. Pt sites are then free from CO and combine with oxygen at 0.3 V to form Pt oxides (Equation 3). These are stripped off the surface on the backward sweep at 0.1 V. The adsorption and desorption of hydrogen (Equation 1) occurs on the backward sweep and the forward sweep of the second cycle, respectively. The CO peak is usually not present in the second cyclic voltammogram.

However, in some cases more than one cycle is required to remove residues remaining in the pores.

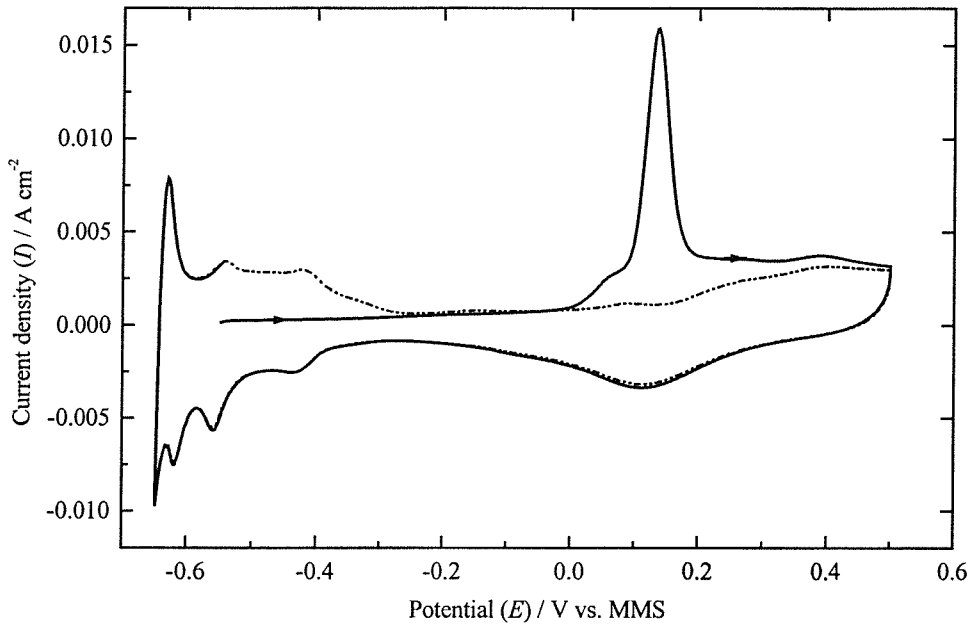

Figure 4: Cyclic voltammogram of a Pt supported on carbon electrode in 1 mol dm^{-3} sulphuric acid; 10 mV s^{-1}; Room temperature; (_____) first scan showing the CO stripping off the surface and (- - - -) second scan.

Pt - CO + H_2O	⟶	Pt + CO_2 + $2H^+$ + $2e^-$	Equation 4
$[Pt]_2$ - CO + H_2O	⟶	2Pt + CO_2 + $2H^+$ + $2e^-$	Equation 5

Table 3: Electrooxidation of CO on a Pt/C electrode cycled in an acidic medium.

4.2.2.2 Calculation

The active surface area of the platinum is calculated from the charge being consumed to oxidise CO. The charge is obtained by integration of the current density peak of the oxidation of CO. The scan rate was taken into account to convert the current density from a function of volts to a function of time. The electrode platinum surface area or EPSA is the ratio of the measured electrochemical charge and the charge that can be held by a polycrystalline platinum electrode. The observed charge for a monolayer of CO on a planar electrode is 420 μC cm^{-2} for linearly bonded CO and 210 μC cm^{-2} for bridge bonded CO [6], [7]. To determine the extent of linearly or bridge bonded CO, the hydrogen adsorption current can be taken as reference. The hydrogen adsorption charge is 210 μC cm^{-2} as

1 electron is involved in the electrochemical reaction. A charge transfer ratio (CO oxidation : H adsorption) of (2:1) indicates that CO is mostly linearly bonded. This has been demonstrated for the low loading of platinum catalysts [8] such as the ≤ 40 wt.% Pt, that are tested in this thesis.

The ElectroChemical Area or ECA allows for electrode fabrication such as the type of ionomer used and the platinum loading. Therefore, the ECA reflects the intrinsic properties of the catalyst and is defined as the ratio of the EPSA and the metal loading (Equation 7).

$$EPSA = \frac{\text{Measured CO charge } [\mu C/cm^2 \text{ geometric}]}{420\ [\mu C/cm^2\ Pt]} \quad \text{Equation 6}$$

$$ECA\ [m^2\ Pt/g\ Pt] = \frac{EPSA}{\text{Pt loading } [mg\ Pt.cm^{-2}] * 10} \quad \text{Equation 7}$$

4.3 Polarisation

Polarisation (or overvoltage) stands for the difference between the thermodynamic cell voltage and the measured cell voltage. Determination of the overvoltage required for the reaction to take place enables an evaluation of the catalyst performance. The polarisation curve consists of the measurement of the voltage as a function of the current density. Also, from the geometry of the cell, the electrolyte and the kinetics of the electrode reactions there arises an ohmic drop or *iR* polarisation, which will be removed from the data.

4.3.1 Practical procedure

A button electrode (1 cm^2) was boiled in triply distilled water prior to electrochemical studies to ensure a fully flooded state and was placed in the glass cell (Figure 1). A solution of 2 mol dm^{-3} methanol in 1 mol dm^{-3} H_2SO_4 was used. Polarisations were performed using a linear-sweep voltammetry technique at stationary current. The potential was swept from 0.3 to - 0.6 V in steps of 40 mV and the current recorded after a stabilisation time of 1 minute. All the data presented in the thesis were *iR* corrected using a current interrupt

method. When the current is interrupted for 10 μs the voltage drops; the ohmic resistance of the system was evaluated by the ratio of the potential drop over the current value. Typically, 5 data points were considered and the average value was taken from the polarisation data.

5 SOLID POLYMER FUEL CELL

The heart of a solid polymer fuel cell is the Membrane Electrode Assembly (MEA) where electrochemical reactions occur. The MEA is sandwiched between flow field plates, heating plates and current collector plates on either side, as shown in Figure 5. Single cells can be combined in series and give a so-called *stack.*

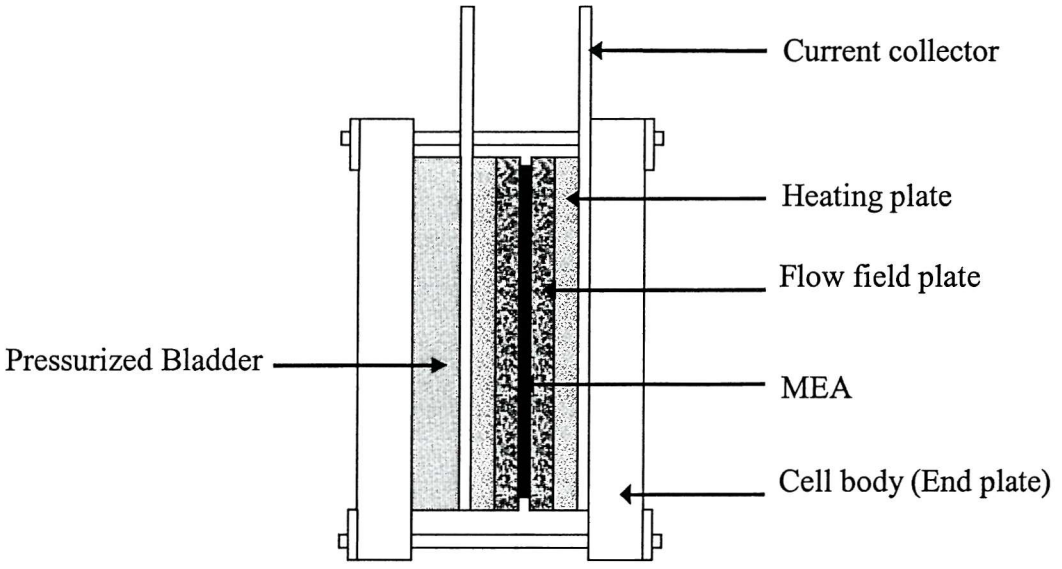

Figure 5: Schematic cross-section of a solid polymer fuel cell.

5.1 Components of a solid polymer fuel cell

5.1.1 Membrane Electrode Assembly (MEA)

An MEA combines anode, cathode and solid polymer electrolyte in a thin unit of a thickness of about 1 mm. At the anode electrode, hydrogen gas molecules are dissociated and adsorbed onto the catalyst (i). H_{ads} is then oxidised into protons and electrons (ii). The overall reaction occurs at a potential of 0 V vs. SHE (reaction (1)). Then, protons flow through the membrane while electrons travel through an external circuit towards the cathode

in order to be consumed in the reduction of oxygen to form water at a potential of 1.23 V vs. SHE (reaction (2)). The theoretical cell voltage is 1.23 V as it represents the difference between the cathode and anode potentials.

$H_2 + 2Pt$	⟶	$2Pt\text{-}H_{ads}$	(i)
$2Pt\text{-}H_{ads}$	⟶	$2Pt + 2H^+ + 2e^-$	(ii)
H_2	⟶	**$2H^+ + 2e^-$**	**E_0 =O V vs. SHE** (1)
$O_2 + 4H^+ + 4e^-$	⟶	**$2H_2O$**	**E_0 =1.23 V vs. SHE** (2)

5.1.1.1 Electrolyte Membrane

The solid polymer membrane is non-permeable to the reactant gases, hydrogen and oxygen, which prevents them from coming into contact. However, the membrane allows the protons to flow from the anode to the cathode whereas it is insulating against the electron flow. Protons migrate because of a concentration gradient and move by reorientating the dipolar water molecules [9]. Thus, the proton conductivity depends on the water content of the membrane.

The early membranes were hydrocarbon-type polymers (e.g. polystyrene sulfonic acid membranes) tested in the PEFCs used in the Gemini space flight programme. The major breakthrough has come with the development of perfluorinated sulfonic acid membranes (Nafion®) which are currently used in polymer fuel cells. The chemical structure of a cation exchange membrane, i.e. Nafion® is given in Figure 6 and consists of two main parts: a perfluorohydrocarbon backbone and a side chain.

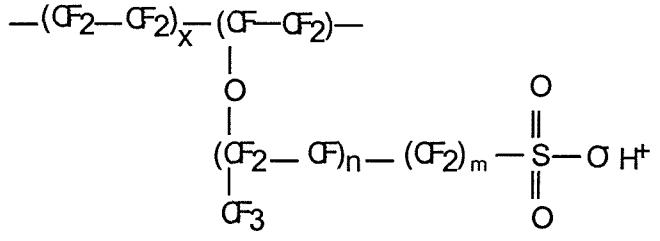

Figure 6: Chemical structure of the Nafion® membrane.

The backbone is a polymerised tetrafluoroethylene (TFE) monomer. The side chain is a perfluorinated vinyl polyether bonded to the PTFE backbone with sulfonic acid group at the end of the chain that enables ion exchange (i.e the proton moves freely in the membrane).

Such electrolyte membranes in fuel cells are typically 50 to 175 μm thick [10] and have similar proton conductivities to 1 mol dm^{-3} sulfuric acid. Acting as a diluted aqueous acid, the membrane has to be used under the boiling temperature of water. Such membranes provide high acidity due to the presence of the fluorocarbon groups (fluorine atom being electronegative) and the high stability of C-F bond in the electrochemical environment resists oxidative attack.

5.1.2 Fabrication of Membrane Electrode Assemblies

The fabrication of the MEA relies on a thorough contact between the membrane and the electrocatalyst spread onto the carbon substrate. The anode and the cathode electrodes (50 cm^2) were prepared as described in section 2.1; the cathode was based on a standard 40 wt.% Pt/XC-72R and the anode was made with 40 wt.% Pt/XC-72R or 40 wt.% Pt, 20 wt.% Ru/XC-72R and finally 40 wt.% Pt, 5 wt.% Mo/XC-72R. A Nafion®-115 membrane was sandwiched between the two electrodes and hot-pressed at 600 pound per inch gauge (psig) for 3 minutes at 180 °C. The latter temperature has to be above the glass transition temperature, i.e. when the polymer becomes viscous and the molecular chains can move relative to each other. This allows the polymer to make a good contact with the catalyst particles situated in the pores deeper in the layer. Therefore, the proton conductivity is enhanced.

5.1.3 Flow field plates

Flow field plates are generally made of graphite, which is highly conductive and corrosion resistant. A web of grooves designed in the inside allowing reactants to reach the MEA (i.e. the back of the electrodes) and product (water) to be collected. Prior to being supplied to the anode and cathode, hydrogen and air are humidified using an internal or external section. The humidifier consists of a Nafion®-117 membrane sandwiched between two flow field plates with deionised water distributed to one side of the membrane and reactant gas to the other side. The assembly is then located between two end plates and a bladder at one side, which allows internal pressurisation.

5.2 Performance of the solid polymer fuel cell

The following experiments have been conducted at Johnson Matthey Technology Center facilities. To assess the MEA performance a standard procedure was used.

5.2.1 Conditioning

The cell was conditioned overnight to assure a stable performance of the fuel cell. The current load was set at 25 mA and the cell temperature was 80 °C. The anode and cathode were pressurised at 30 psi and were supplied by H_2 and Air using fuel and oxidant stoichiometries of 1.5 and 2, respectively. The cell potential was recorded against time until a stable performance was certified. For such experimental conditions the usual response of the cell potential is expected to be around 0.7 V. Then two types of experiments were conducted which are degradation and polarisation.

5.2.2 Degradation

To study the poisoning effect of CO and CO_2, the anode was exposed to four different fuel reformate mixes, i.e. 100 ppm CO in H_2, 10 ppm CO in H_2, (40 ppm CO +25% CO_2) in H_2 and 25% CO_2 in H_2. The degradation of the cell was recorded by plotting the cell potential as a function of the time (Figure 7).

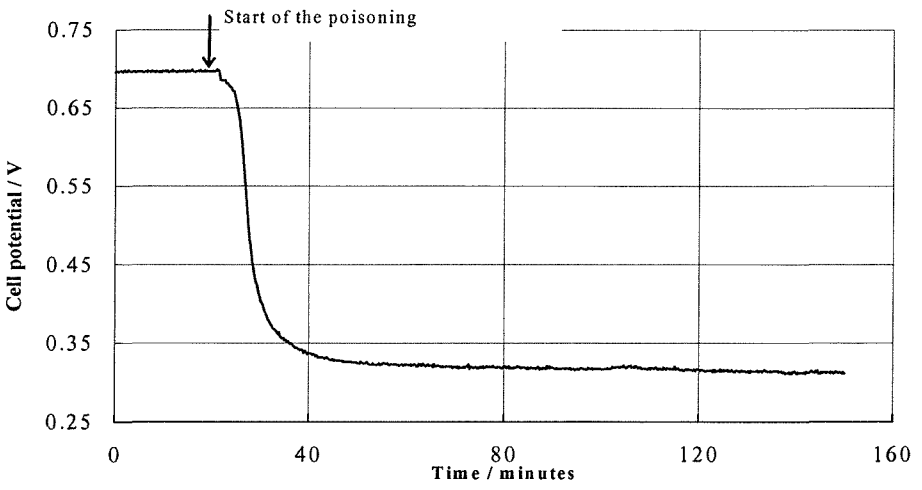

Figure 7: Degradation plot, i.e. E_{cell} vs. time for a Pt/C anode poisoned with a 40 ppm CO + 25 % CO_2 fuel reformate mix.

The cell voltage will drop few seconds after the incorporation of the poisoned reactant and will stabilise to a value that accounts for the cell degradation. After a stabilisation time of 30 minutes, the cell was allowed to recover under pure H_2. At least 2 hours are necessary for the cell to reach its initial conditioning potential. Such potential losses are related to the intrinsic properties of the catalyst itself used at the anode electrode.

5.2.3 Polarisation

Different factors such as the *activation*, *ohmic* and *concentration overpotentials* account for the decrease in cell voltage over the equilibrium potential. Figure 8 depicts a typical cell potential vs. current density plot.

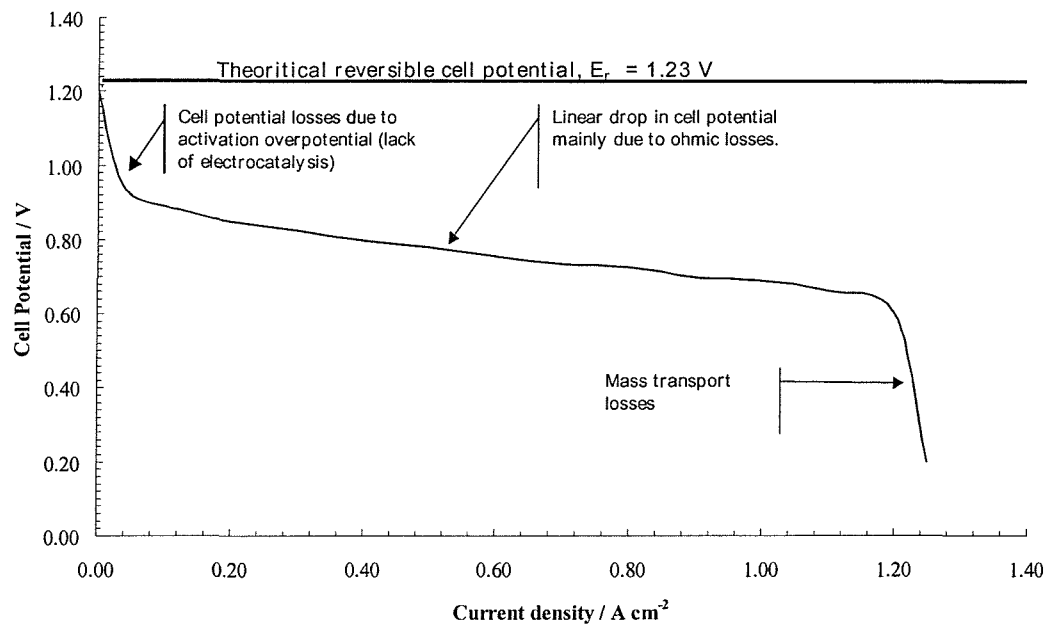

Figure 8: Typical cell potential vs. current density plot or polarisation curve.

The *activation* polarisation depends on the rate of the reaction (e.g. kinetics of the charge transfer) occuring at the anode and the cathode. Contrary to the cathode reaction, hydrogen oxidation occurs quickly at the anode. Therefore, the activation overpotential will be related to the oxygen reduction reaction more specifically. This potential loss depends on the electrocatalyst properties (i.e. the energy barrier of the reaction) and thus, the size and area of the catalyst will influence this voltage loss. Equation 8 describes the kinetics of the activated processes [11].

$$E_{cell} = (E_r + b \log i_o) - b \log i - iR_{membrane} \quad \text{Equation 8}$$

where E_r is the reversible cell potential, i_o is the exchange current density for oxygen reduction, b is the Tafel slope for oxygen reduction, i.e – 60 mV per decade, and R the resistance of the MEA and the hardware.

The *ohmic* polarisation (η_r) is directly proportional to the resistance existing in the cell, i.e. $\eta_r = iR$, where R is the internal resistance per cm^2 and combines the electronic resistance (flow of electrons) of the hardware of the cell and the ionic resistance (flow of protons) of the membrane. This controls the slope of the pseudo-linear region indicated in Figure 8. The ohmic losses are commonly determined by a current interrupt method. When the current is stopped the drop in potential allows the evaluation of the resistance according to Ohm's law. Also, based on iR corrected data recorded on pure oxygen the determination of i_o and $R_{membrane}$ is realised by a least-squares fit of Equation 8.

The end of the pseudo-linear region (at high current densities) markes the onset of the mass transport limitation or a slow diffusion of the oxygen through the cathode (to the catalyst sites). This is caused by an accumulation of the water molecules that are either produced at the cathode or transported from the anode to the cathode. Experimentally, the mass transport determination is based on the comparison of the cell performance when air and oxygen are the fuels used at the cathode side.

5.2.3.1 Practical procedure for polarisation measurement

Polarisation experiments were conducted for different anode reformate mixes, e.g. H_2 fuel and (40 ppm CO + 25 % CO_2) in H_2 without or with air bleed. In the latter case, oxygen was injected at 5% of the total fuel flow rate to restore the cell performance to that of the pure hydrogen. The cell temperature was set at 80 °C and the anode and cathode were pressurised at 30 psi. The cell load was changed manually from open circuit to 40 mA and the cell voltage recorded after a stabilisation time of 3 minutes for each load value. The corresponding iR drop was measured by the current interrupt method. The experiment was conducted by switching the gas reactant at the cathode from oxygen to air (to evaluate the mass transport limitation) for each load value.

6 EXTENDED X-RAY ABSORPTION FINE STRUCTURE (EXAFS)

The following section is not exhaustive, but more details can be found in references [12], [13].

6.1 General principles

A monochromatic X-ray beam passes through a material, which absorbs the photons at the energy ($h\nu$). The photon energy is defined by hc/λ, where h is Planck's constant, c is the velocity of light and λ is the photon wavelength. The incident intensity (I_o) of the x-ray beam will be attenuated according to Beer-Lambert law (Equation 9).

$$I = I_0 e^{-\mu x} \qquad \text{Equation 9}$$

Where μ is the absorption coefficient at the energy hν and x is the thickness of the sample.

The absorption of the photon by the material occurs due to the photoelectric effect. When the incoming photon with a large enough energy hits the atom, a core electron is ejected to an exited state or to the continuum (after the absorption edge), as illustrated in Figure 9. Then a core hole is created and filled by an upper state electron.

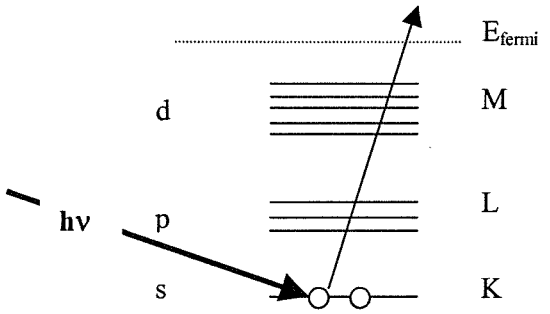

Figure 9: Photoelectric effect.

The X-ray absorption spectroscopy (XAS) experiment consists of the measurement of the linear absorption coefficient (μ) as a function of the photon energy. A typical XAS spectrum is shown in Figure 10 and can be divided in three main parts.

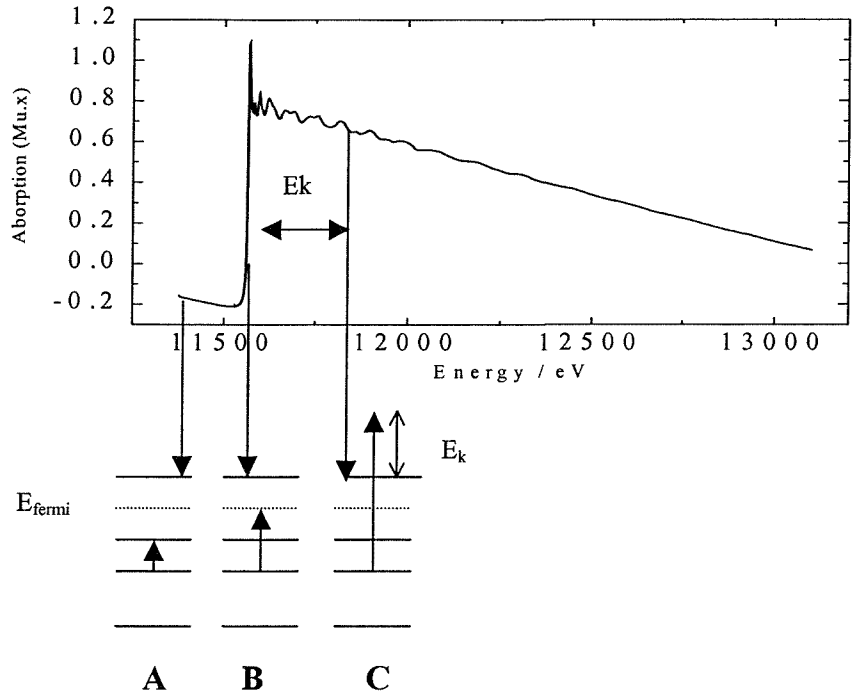

Figure 10: XAS spectrum of Pt foil recorded at Pt L_{III} edge and the corresponding photoelectric effect.

A - The photon energy is not large enough to excite or to ionise the electron of the element of interest.

B - The photon energy reaches the binding energy of an electronic level of one of the constituent element of the sample. The absorption coefficient increases abruptly. The energy region near the absorption threshold depends on the electronic structure of the sample. This so-called X-ray Absorption Near Edge Structure (XANES) is difficult to interpret as it is dominated by multiple scattering events, which will be described below.

C - The photon electron is ejected with a kinetic energy (E_k) which is given by:

$$E_k = h\nu - E_{binding}$$

About 50 eV above the absorption edge the photon electron has enough kinetic energy to become free of the absorber and scatters off the neighbouring atoms. The ejected photoelectron may be approximated by a spherical wave function. The wave vector of the outgoing photon electron (k) is given by Equation 10.

$$k = \frac{\sqrt{2mE_k}}{\hbar}$$ Equation 10

Where m is the mass of the electron and $\hbar$ is h/2π with h Planck's constant.

The linear absorption coefficient is proportional to the transition probability of the initial state $|i\rangle$ to the final state $|f\rangle$ according to Fermi's Golden rule (Equation 11).

$$\mu \equiv \sum_f \left|\langle f|\vec{\varepsilon}\cdot\vec{r}|i\rangle\right|^2 \delta(E_i - E_f - h\nu)$$ Equation 11

Where $\vec{\varepsilon}$ is the electric field polarisation vector of the photon, $\vec{r}$ is the coordinate vector of the electron, E_i is the initial energy and E_f is the final energy.

With, $|f\rangle = |backscattered\rangle + |outgoing\rangle$

The Equation 11 demonstrates that the linear absorption coefficient is modulated by the final state wave function (i.e. the backscattered photoelectron wave). The scattering of the outgoing photoelectron wave off the surrounding neighbours of the exited atom interferes with the outgoing photoelectron wave giving rise to the oscillations in the EXAFS spectrum. When changing the photon energy the wave vector changes according to Equation 10. As shown in Figure 11 the interferences are then either in phase (constructive) or out of phase (destructive) depending on the kinetic energy of the photoelectron wave and generate the oscillations of the absorption coefficient. These oscillations can then be expressed by Equation 12.

$$\chi(h\nu) = \frac{\mu(h\nu) - \mu_0(h\nu)}{\mu_0(h\nu)}$$ Equation 12

With $\mu(h\nu)$: total absorption coefficient at the energy $h\nu$

$\mu_0(h\nu)$: smooth atomic background (no scattering from neighbouring atoms) at the energy $h\nu$.

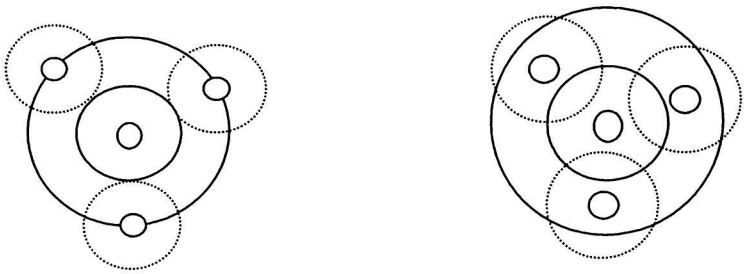

Figure 11: Schematic of a constructive (left) and destructive (right) interference; outgoing wave is indicated by a solid line and backscattered wave by a dotted line. The lines represent the peaks in the amplitude of the photoelectron wave.

The outgoing photoelectron may use a single or a multiple scattering path (Figure 12) to return to the absorbing atom. If the free electron wavelength is much larger than the inter-atomic distance in the sample the photoelectron may take multiple scattering paths with neighbouring atoms before it has lost all its energy. In the case of single scattering the electron scatters one time with a neighbouring atom and returns to the absorber atom.

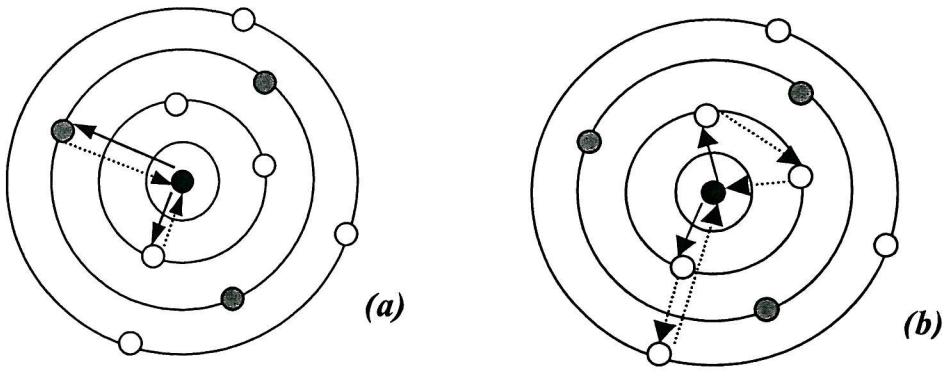

Figure 12: Schematic representation of the single *(a)* and multiple *(b)* scatterring; black filled circle is the absorbing atom, grey and unfilled circles the neighbours; forward scattering is indicated by solid arrows and backscattering by dashed arrows.

6.2 EXAFS formula

$$\chi(k) = \sum_{j=1}^{Shells} A_j(k)\sin\delta_j(k) \qquad \text{Equation 13}$$

with $$A_j(k) = \frac{N_j}{kR_j^2} S_o^2 F_j(k) e^{-2k^2\sigma_j^2} e^{-2R_j/\lambda(k)}$$

and $$\sin\delta(k) = \sin(2kR_j + \varphi_j(k))$$

where N_j is the number of atoms of type j at the distance R_j from the absorber atom

$F_j(k)$ is the magnitude of the backscattering from the jth atom

$\delta_j(k)$ is the phase shift resulting from the backscattering off the jth atom

S_o is the amplitude reduction factor reflecting multi-electron effects and central atom shake-up and shake-off due to relaxation processes after photo-ionisation

$e^{-2k^2\sigma_j^2}$ accounts for the finite life time of the exited state

λ is the mean free path of the electron

σ^2_j is the relative mean squared disorder along the distance between the absorbing atom and the backscattering atom due to thermal and static motions

k is the electron wave number defined by Equation 10

The EXAFS formula as expressed in Equation 13 results from the derivation of the wave function (Equation 11) based on a plane wave approximation [14]. Thereby, a single scattering mode where the atomic radii are much smaller than the interatomic distances has been assumed. This simplification over the spherical wave is sufficient to describe and analyse the experimental EXAFS signals. However, to analyse the data properly at low k value (i. e. XANES region) and to reflect the contribution of the neighbouring atoms at longer interatomic distances a curved wave approximation will be required to take into account multiple scattering processes. The EXAFS formula describes the sum of the interference patterns scattered off all the neighbouring atoms through the sine wave term, sin $\delta(k)$. An amplitude term $A_j(k)$ contains the coordination numbers (N_j) and the disorder parameter (σ^2). The argument of the sine function consists of the interatomic distances (R_j) between the absorber atom and the scatterer as well as a phase factor $\varphi_j(k)$. This phase factor (or phase shift experienced by the electron in the scattering process) is expressed as follows:

$$\varphi_j(k) = 2\varphi_{absorber}(k) + \varphi_{backscatterer}(k)$$

6.3 Data analysis

To extract $\chi(k)$ from the raw data several consecutive steps are used. The steps are pre-edge substraction, determination of the inner potential, background substraction and conversion from *Energy*-space to *k*-space. But the first task is to extract $\chi(E)$ from the experimental curve. As χ(E) is a function of the linear absorption coefficient (Equation 14) it is convenient to normalise the data in *Energy*-space.

$$\chi(E) = \frac{\mu(E) - \mu_0(E)}{\mu_0(E)} \qquad \text{Equation 14}$$

With $\mu_0(E)$ the linear absorption coefficient of the isolated atom.

6.3.1 Data normalisation process

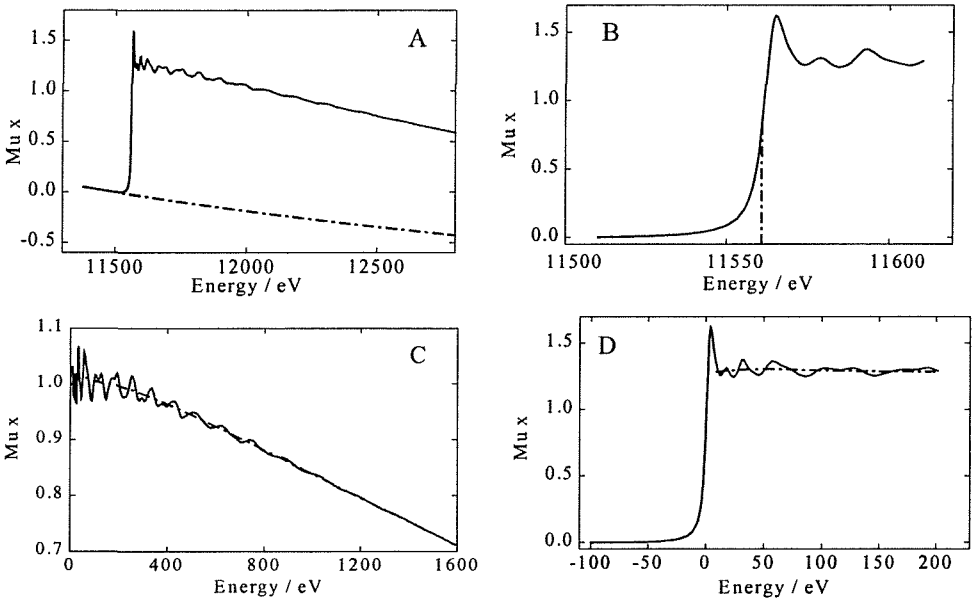

Figure 13: A) Pre-edge substraction, B) Inner potential, C) Background substraction, D) Normalisation.

The *pre-edge substraction* removes the absorption of the electron from shells other than the one under study and from other elements in the sample. This involves a fitting of the data

before the edge using a polynomial function and extrapolation of this fit in the data region as shown in Figure 13A.

The *inner-potential* (E_0) which accounts for the transformation into *k*-space is chosen at a point half way down the edge (i.e. inflection point or maximum of the first derivative), as shown in Figure 13B.

The *background substraction* illustrated in Figure 13C involves fitting a cubic spline function as expressed in Equation 15. Four parameters have to be defined: SM (smoothing parameter), WE (weighting factor) fixed at 0.075 and Start (about 10 to 20 eV above the edge) and End energies (in order to determine the number of points). Also, attention has to be taken not to remove some of the EXAFS signal (the spline should not have oscillations with frequencies similar to those of the EXAFS oscillations). This spline that approximates the smooth background is substracted from the experimental data and the EXAFS oscillations are then obtained.

$$\sum_{i=1}^{NPts} \frac{(\mu x_i - Bck_i)^2}{e^{-WEk_i^2}} \leq SM \qquad \text{Equation 15}$$

Since the EXAFS signal reflects the contribution of all the target element atoms from the irradiated volume, the experimental spectrum must be normalised to take into account the concentration (proportional to the amplitude). Thereby, the spectrum will be *normalised* per absorber atom by division of the total absorption data by the edge step at 50 eV after the absorption edge (Figure 13D). This energy point has to be chosen far enough from the threshold value (far from the Near Edge structure) in order to avoid any distortion in the amplitude of the EXAFS oscillations.

The $\chi(E)$ spectrum is then available and will be simply converted into *k*-space according to Equation 16. The final $\chi(k)$ is shown in Figure 14.

$$k = \sqrt{\left(\frac{8\pi^2 m}{h^2}\right) * (h\nu - E_0)} \qquad \text{Equation 16}$$

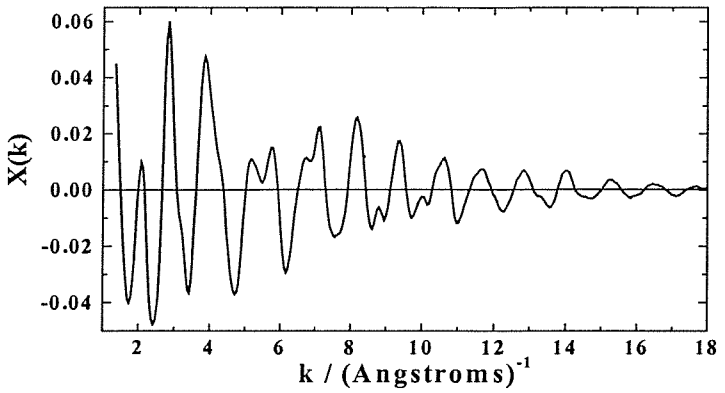

Figure 14: χ(k) extracted from the XAS spectrum.

6.3.2 Fourier transformation

Sayers *et al.* proposed a Fourier transform method to analyse the EXAFS oscillations [14]. The function is given by Equation 17.

$$\Phi_n(R) = \frac{1}{\sqrt{2\pi}} \int_{k_{min}}^{k_{max}} k^n \chi(k) e^{i2kR} dk \qquad \text{Equation 17}$$

The Fourier transform (FT) is a complex function defined by the imaginary part, useful for accurate determination of the interatomic distances, and by the absolute part (envelope) corresponding to the number of neighbours and disorder parameter. Figure 15 illustrates the radial distribution function (i.e. the absolute part of the Fourier transform) with peaks corresponding to scattering from atoms at each scattering distances R_j, i.e. at each coordination shell radius. However, the distances observed at the maxima of the FT amplitude for each shell do not correspond accurately to the real distance. This is caused by the dephasing φ_j(k), in the sine function.

In addition, k^n-weighting of the Fourier transform can be used to distinguish between high and low Z scatterers around the absorber atom. An element with low mass (like oxygen) will scatter mainly at low *k*-values, while platinum (high mass) will scatter significantly at higher *k*-values. This method emphases the important scatterer in a specific region.

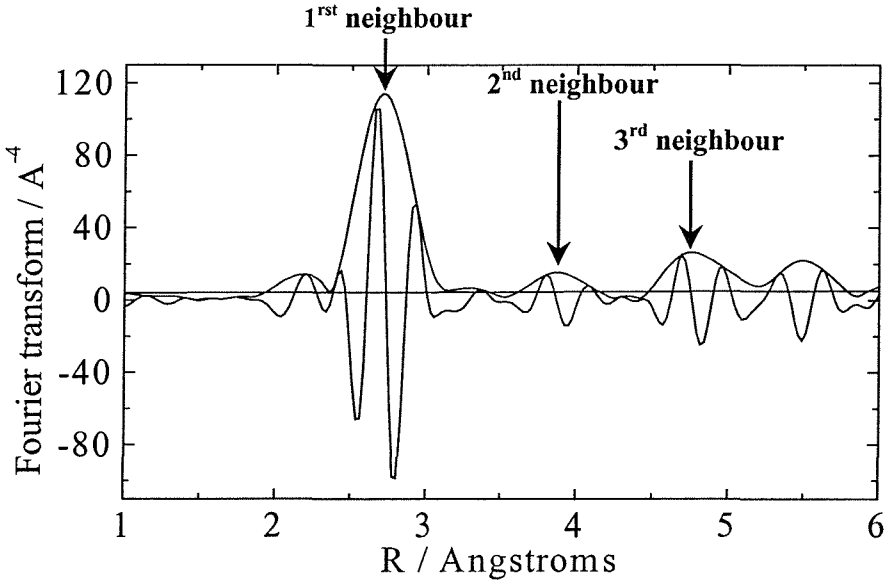

Figure 15: Fourier transform of the χ(k).

6.3.3 Data analysis programs

The EXAFS spectra collected at the Synchrotron Radiation Source (S.R.S.) were analysed using computer programs available on the XRSSERV1 computer (a Unix operating system) at Daresbury Laboratory. The dataset as collected is a list of the values of the various detectors collected at each point in the spectrum. These points are defined by the position of the monochromator in millidegrees. A calibration of these data is required and is completed with the EXCALIB program. The *x*-scale has to be turned into Energy by converting the millidegree scale into eV. Also, the *y*-scale is turned into absorption by dividing the reference reading (I_o) by the signal reading (I_t) and taking the log value for transmission experiments or by dividing the signal reading (I_t) by the reference reading (I_o) for the fluorescence data. Further, background substraction (energy calibration, pre-edge and post-edge background substraction and edge step normalisation) of the initialised spectra was performed using the EXBROOK program based on a smooth polynomial curve. Finally, the curve fitting of the k^3-weighted data was completed using the EXCURV98 program based on the curve wave approximation. In this, the exited atom wave function is modelled by the next element up the periodic table (Z+1) in the presence of a 2p core hole. The curve fitting of the data was achieved in *k*-space where coordination number (*N*), distance to the nearest

neighbouring atom (R), the Debye-Waller term ($2\sigma^2$) and the shift in the Fermi energy (E_f) were refined. The refinement involves least-squares minimisation of the fit index such that:

$$\phi_{EXAFS} = \sum_i^N \omega_i^2 \left(\chi_i^{\exp}(k) - \chi_i^{th}(k)\right)^2$$

$$\text{with } \omega_i = \frac{k_i^n}{\sum_j^N \left|\chi_j^{\exp}(k)\right|}$$

where $\chi^{\exp}(k)$ and $\chi^{th}(k)$ are the experimental and theoretical EXAFS, N the number of data points and k the magnitude of the photoelectron wave vector.

The goodness of the fit can be indexed with an R_{EXAFS} factor:

$$R_{EXAFS} = \sum_i^N \frac{\left(\left|\chi_i^{\exp}(k) - \chi_i^{th}(k)\right|\right)}{\sigma_i} \times 100\%$$

where σ is the variation in the path length.
A value around 20 to 30% is normally considered to be a reasonable fit.

6.4 Experimental Set-Up

6.4.1 Source of X-rays

The main equipment used to produce X-rays for XAS studies is the synchrotron radiation source (S.R.S) illustrated in Figure 16. The SRS consists of a beam of electrons orbiting at relativic speeds in a storage ring. The intensity of the X-rays is 10^4 –10^6 times greater than a conventional X-Ray tube. Therefore, the acquisition time for an experiment will be largely reduced and the ratio of signal to noise will be improved as it is proportional to the square root of the X-ray intensity.

Electrons are emitted from a heated filament and accelerated under high vacuum in the LINAC (LINear ACcelerator). Bunches of electrons are injected in the booster ring and accelerated under high vacuum, i.e. 10^{-7} Torr to the required speed (almost the speed of light) and energy, up to 600 MeV. Electrons are stored in the storage ring where they circulate under ultra high vacuum (10^{-9}-10^{-10} Torr). The energy is ramped to 2 GeV in the storage ring.

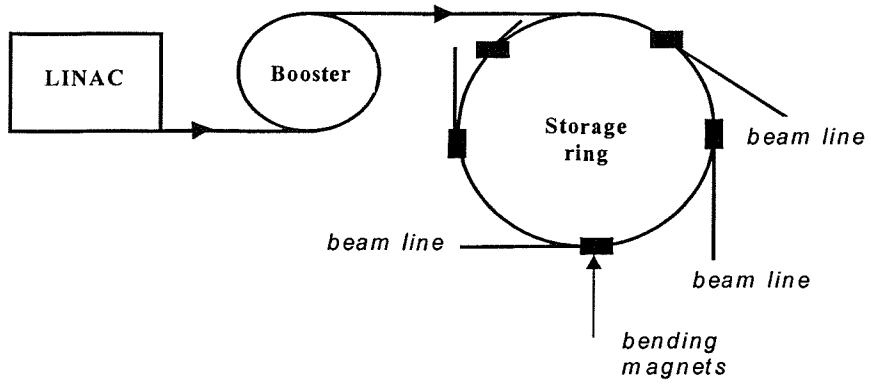

Figure 16: Schematic of a Synchrotron Radiation Source (SRS).

Since the accelerated electrons are constantly emitting electromagnetic radiation, a constant supply of energy through a Radio Frequency generator is required to maintain them in orbit. Also, an electron in a circular orbit experiences an acceleration towards the centre of the orbit and, as a result emits radiation in an axis perpendicular to the motion. Thereby, the emission of the electron is made tangential to the storage ring. The bending magnets (dipoles) provide the desired polychromatic radiation profile (e.g. from IR to Soft x-ray) by modulating the path-way of the electron beam (i.e. electrons are forced to deviate from their straight path to a curved track). Other magnetic structures are for many experiments more effective sources of radiation than the ring bending magnets as the energy distribution of synchrotron radiation is enhanced . Multipole magnets such as undulators or wigglers may be inserted into straight sections of a storage ring and give rise to shorter radius curvature of the orbit caused by their stronger magnetic field. Within the wiggler or undulator the electron beam is periodically deflected. However, no net deflection or displacement of the electron beam occurs. A wiggler forces the electron beam to execute a trajectory with a smaller local radius of curvature than in the dipole bending magnets by using a larger local magnetic field. Thus, the effect of the wiggler on the emitted spectrum is to increase the critical energy and to shift the overall spectrum to higher energies. As the angular deflection of the electron beam matches the angular emission of the radiation from each pole to the acceptance of the synchrotron radiation beam line, enormous enhancements of the brightness compared to the ring bending magnets may be obtained. Also the radiation from many poles can be collected in a small angular cone for one experiment.

An undulator is a periodic electromagnetic structure which forces electrons to oscillate transversally in a given plane (planar undulator) or to describe a helix along its mean path

(helical undulator). Its design aims for the production of quasi-monochromatic synchrotron radiation. The angular deflection of the electron beam is now kept smaller or equal to the natural emission angle of the synchrotron radiation. Interference effects in undulator radiation result in peaks at one or few wavelengths [13]. Undulator devices are commonly used for soft X-ray experiments whereas wigglers for hard X-ray experiments.

6.4.2 Transmission XAS experiment

The transmission detection mode is the most commonly used in order to perform XAS experiments. The experimental setup is illustrated in Figure 17.

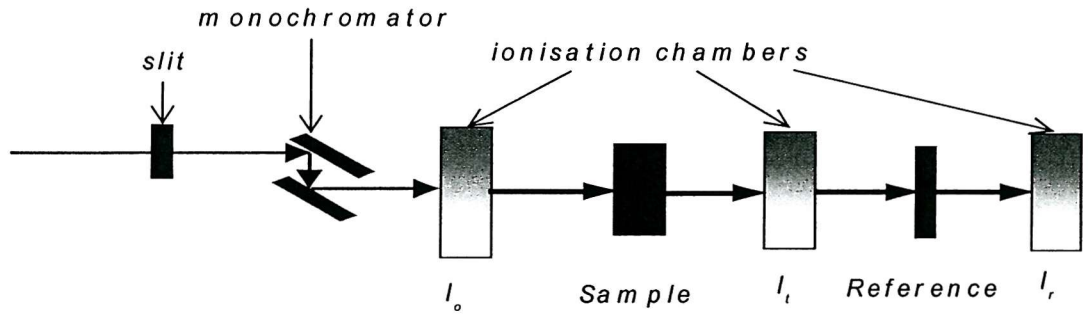

Figure 17: Schematic of the experimental setup of the transmission detection mode.

The size of the white X-ray beam emitted from the synchrotron is reduced upon passing through the *slit* and thus is collimated. Thus, the energy resolution of the monochromator is improved since the acceptance angle of the monochromator crystals is narrower than the synchrotron opening angle.

The *monochromator* consists of two parallel crystals, which are separated according to the equation 2Dcosθ, where D is the distance between the two crystals. Due to their low X-ray absorbance, silicon crystals (close to that of the perfect crystal) are often used. The energy is selected by Bragg reflection off the crystal surfaces, such that:

$$\lambda = \frac{2d}{n}\sin\theta$$

where d is the spacing between the crystal planes, θ the incidence angle of the radiation and n the order of reflection.

Usually, the first order of reflection is used and the energy distribution (i.e. intensity vs. energy) is described by a Gaussian distribution. The width of the Gaussian peak gives the resolution of the EXAFS spectrum. The higher harmonics of a selected energy are removed by detuning the angle of the second crystal to leave 50% of the maximum exiting intensity at the Pt L_{III} edge or 60% at the Ru K edge. This is possible because of the small acceptance angle of the higher order reflections. The vertical displacement of the beam entering and exiting the monochromator allows the installation of a beam stop to block the rejected white light from striking the sample. However, as the monochromator is scanned, the beam will be displaced vertically. The sample height must , therefore, be adjusted accordingly to account for this displacement, otherwise non-uniformities in the sample will increase noise levels in the data.

The *ionisation chambers* (detectors) are filled with noble gas mixtures such as He, Ne and Ar. These consist of two metallic plates with a potential difference between them, typically 500 V. The first one I_0 absorbs about 20% of the incoming photons whereas the second one I_t absorbs 80%. A third ion chamber placed at the end of the setup measures the transmitted beam I_r following a reference material or foil. This is useful for internal calibration of the X-ray beam energy when small edge shifts occur. Each energy range will require a specific gas mixture in order to obtain a linear response of the ionisation chambers. The intensity of the detectors is recorded by a data acquisition system.
The transmission detection mode is suitable for the investigation of concentrated samples whereas the fluorescence detection mode is for dilute systems.

6.4.3 Fluorescence XAS experiment

The fluorescence radiation results from the filling of the core hole generated by the absorption of an X-ray photon. The energy of this radiation is characteristic of the absorbing element and is less than the original exciting radiation. Also, the fluorescence EXAFS signal consists of a small fraction of the total absorption only which is proportional to the incident intensity such that:

$$\mu(E) = \frac{I_{fluorescence}}{I_0}$$

Therefore, the isolation of the EXAFS from the background (e.g. elastically and Compton scattered radiation that is present at higher energy than the fluorescent signal) is performed

by a solid state detector. This device allows single photon counting and therefore, the discrimination of the signal from the background.

The fluorescence experimental set-up is illustrated in Figure 18. The sample is turned 45° to the incident beam to maximise the fluorescence signal/solid angle seen by the detector. By detecting just the fluorescent signal from the atom of interest the ratio signal/noise is improved.

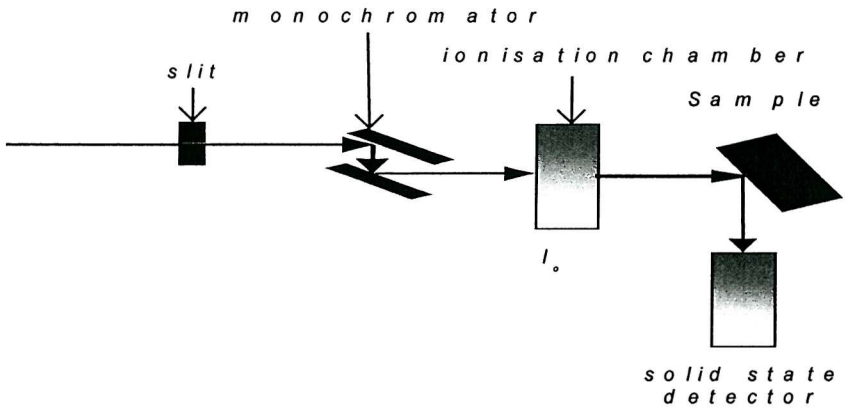

Figure 18: Schematic of the experimental setup of the fluorescence detection mode.

6.4.4 XAS experimental procedure

The X-Ray absorption spectra were collected on Wiggler station 9.2 of the Synchrotron Radiation Source at Daresbury. The ring operated at 2.0 GeV and the current range was 100-250 mA. A double crystal monochromator, i.e. Si (220) was detuned to 50% at the Pt edge and to 60% at the Ru K or Mo K edges to minimise the higher harmonics. Spectra were recorded at room temperature in transmission detection mode at the Pt L_{III} and L_{II} edges or fluorescence detection mode at the Ru K and the Mo K edges, respectively.

Firstly, the *in situ* XAS measurements were done with an electrochemical cell based on the design reported by Herron *et al.* [15] and illustrated in Figure 19. The main characteristics of the cell are that the X-ray beam passes through the working electrode as the X-ray windows are made of an X-ray transparent polymer or Kapton film. A button electrode (2.5 cm^2) was boiled in triply distilled water prior to EXAFS measurement to ensure a fully flooded state. Then, the working electrode was placed between a gold wire current collector (back of the electrode) and layers of filter paper presoaked with a solution 1 mol dm^{-3} H_2SO_4 (catalyst side of the electrode). The assembly was then sandwiched

between the two acrylic parts (i.e. cell body). A thin layer of flowing electrolyte (i.e. 1 mol dm^{-3} H_2SO_4) allowed the removal of gas bubbles within the system. A platinum gauze counter electrode was situated in the electrolyte and the reference electrode (Mercury/Mercurous sulfate) was connected via a salt bridge filled with the electrolyte solution. Spectra were recorded at successive potentials within the potential window, - 0.6 to 0.4 V vs. MMS.

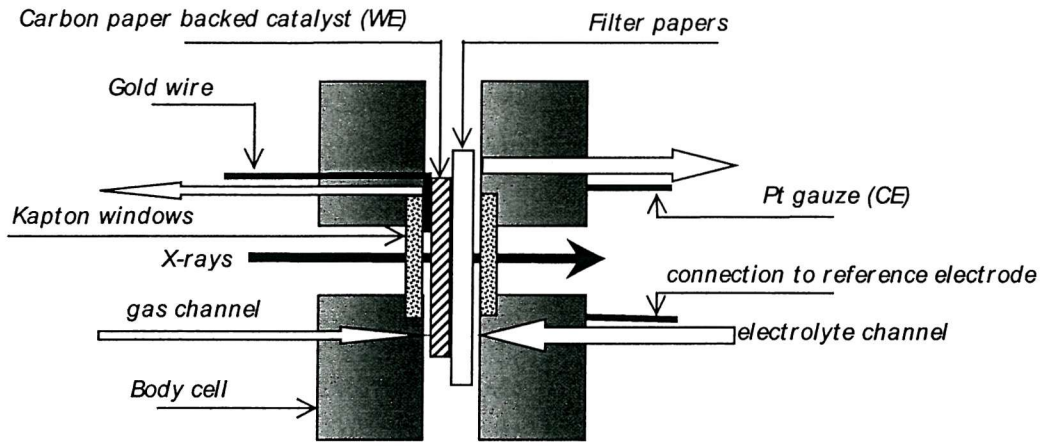

Figure 19: Schematic cross-section of the electrochemical EXAFS cell.

Secondly, *ex situ* EXAFS measurements were completed using the as prepared catalyst powders or electrodes. Prior to EXAFS measurements the appropriate quantity of sample powder was mixed with boron nitride to obtain an edge jump of 0.3 to 1. The mass M (*g*) of catalyst required was calculated according to the following equation:

$$M = \frac{A \ln\left(\frac{I_o}{I}\right)}{\sum_i f_i \left(\frac{\mu}{\rho}\right)_i}$$

where A is the sample area scaled in cm^2, f_i is the weight fraction of the ith element in the sample and $(\mu/\rho)_i$ is the mass absorption coefficient of the ith element at the wavelength of interest scaled in $cm^2\ g^{-1}$.

The mass absorption coefficient has been reported for all the atoms of the periodic table by McMaster *et al.* [16].

7 REFERENCES

[1] Stiles, A. B., *Catalyst supports and supported catalysts. Theoritical and applied concepts*; Butterworths: Boston, 1987.

[2] Keck, L.; Buchanan, J. S.; Hards, G. A.; U.S., 1991; Vol. 5; pp 161.

[3] Bard, A. J.; Faulkner, L. R., *Electrochemical techniques*; Wiley-Interscience: New York, 1979.

[4] Greef, R.; Peat, R.; Peter, L.; Pletcher, D.; Robinson, J., *Instrumental Methods in Electrochemistry*; Ellis Horwood Limited: Chichester, 1985.

[5] Hogarth, M. P. *The development of the Direct Methanol Fuel Cell*; Ph. D, Newcastle upon Tyne, 1995.

[6] Bett, J.; Kinoshita, K.; Routsis, K.; Stonehart, P., *J. Catal.*, **1973**, *29*, 160.

[7] Beden, B.; Lamy, C.; De Tacconi, N. R.; Arvia, A. J., *Electrochimica Acta,* **1990**, *35*, 691.

[8] Ralph, T. R.; Hards, G. A.; Keating, J. E.; Campbell, S. A.; Wilkinson, D. P.; Davis, M.; St-Pierre, J.; Johnson, M. C., *J. Electrochem. Soc.,* **1997**, *144*, 3845.

[9] Bockris, J. O. M.; Reddy, A. K. N. *Modern electrochemistry*; Plenum, Ed.: New York, 1970; pp 481-484.

[10] Murphy, O. J.; Hitchens, G. D.; Manko, D. J., *J. Power Sources,* **1994**, *47*, 353.

[11] Mosdale, R.; Srinivasan, S., *J. Electrochem. Soc.,* **1994**, *49*, 117.

[12] Koninsberger, D. C.; Prins, R., *X-Ray Absorption: Principles, Applications, Techniques of EXAFS, SEXAFS, and XANES*; Wiley: New York, 1988.

[13] Abruna, H. D., *Electrochemical Interfaces: Modern Techniques for In-Situ Interface Characterisation*; VCH Publishers: New York, 1995; pp 3-54.

[14] Sayers, D. E.; Stern, E. A.; Lytle, F. W., *Phys. Rev. Lett.,* **1971**, *27*, 1204.

[15] Herron, M. E.; Doyle, S. E.; Pizzini, S.; Roberts, K. J.; Robinson, J.; Hards, G.; Walsh, F. C., *J. Electroanal. Chem.,* **1992**, *324*, 243.

[16] McMaster, H.; Kerr Del Grande, N.; Mallet, J. H.; Hubbell, J. H., *Compilation of X-ray Cross-Sections, National Bureau of Standards, for calculation of x-ray cross sections*; http://www.csrri.iit.edu/periodic-table.html

CHAPTER THREE : EXAFS STUDY OF PT-RU/C FUEL CELL CATALYSTS

1 INTRODUCTION

X-ray Absorption Spectroscopy (XAS) offers the unique ability to simultaneously probe both the electronic and structural parameters under *in situ* electrochemical conditions with element specificity. The analysis of the L_{III} and L_{II} absorption edges of Pt using the near edge part of the spectra (XANES) provides a direct measure of Pt 5 d band vacancies per atom. The post edge region of the spectrum (50-1500 eV after the edge position) referred to as the Extended X-ray Absorption Fine Structure (EXAFS) provides information on the short range atomic order (bond distances, coordination numbers). In relation to Polymer Electrolyte Membrane Fuel Cell (PEMFC) catalysts, *in situ* XAS has been shown to be very useful. Herron *et al.* have demonstrated the utility of *in situ* EXAFS measurements for the characterisation of surface oxides formed on a dispersed Pt/C catalysed fuel cell electrode [1]. Other XAS studies of small supported platinum particles have identified the type and concentration of species on the electrode surface for oxygen reduction [2]. Chang *et al.* have speculated that Pt aggregates during electrochemical reactions in 1 M $HClO_4$ as evidenced by the structural changes [3]. This technique has also been applied to binary carbon supported alloys of Pt with first row transition elements for oxygen reduction [4], [5] and for hydrogen oxidation [6]. The alloys were shown to possess higher Pt 5 d band vacancies per atom and shorter Pt-Pt bond distances as compared to Pt/C. McBreen *et al.* have shown a contraction of the Pt-Pt bond distances from 2.77 Å to values between 2.71 Å and 2.73 Å due to the presence of Ru in the particle [7]. Also, the interaction of the alloying element can be clearly seen in the EXAFS data. Borgna *et al.* have demonstrated an interference phenomenom in the EXAFS spectra of Pt-Sn bimetallic catalyst [8]. From the interference between the two pairs of atoms (Pt and Sn) with similar distances (2.77 and 2.75 Å) a short distance peak around 2.2 Å arises in the uncorrected Fourier transform of the EXAFS spectrum. They have ascribed this peak to the coexistence of unalloyed Pt and alloyed PtSn species.

In this chapter *in situ* XAS results obtained for Pt-Ru/C electrocatalysts are presented. The effect of the heterometallic interaction on the EXAFS arising from the first coordination

sphere was probed by collecting data at both the Pt L_{III} and Ru K absorption edges. An interference between the backscattering from Pt and Ru neighbours was observed and the effect of this interference on the EXAFS data is discussed.

2 EXPERIMENTAL

2.1 Material and experimental conditions

Platinum based carbon supported electrocatalysts (Table 1) were formulated into anode fuel cell electrodes using the method described in chapter 2, section 2.1. The higher loading electrodes (5 mg Pt cm^{-2}) were placed in the electrochemical cell with X-Ray transparent windows as described in chapter 2, section 6.4.4. *In situ* EXAFS measurements were conducted in transmission detection mode at the Pt L_{III} and the Ru K edges. The data were recorded at room temperature in 1 mol dm^{-3} sulfuric acid according to the experimental procedure fully detailled in chapter 2, section 6.4.2.

Catalyst	**wt.% Pt**	**wt.% Ru**
Pt/C	40	/
Pt-Ru/C (A)	40	20
Pt-Ru/C (B)	40	20

Table 1 : Nominal loading of metal (wt.%) in the supported on carbon catalysts.

2.2 Data analysis

Data reduction of the raw spectra and the extraction of the structural parameters were completed with the EXBROOK and EXCURV98 programmes [9]. This was fully described in chapter 2, section 6.3.3.

3 RESULTS

In order to avoid contributions from the oxidation of the electrocatalysts the electrode was reduced by applying a potential of - 0.6 V vs. MMS. In addition, the EXAFS data were k^3-weighted to minimise the residual contribution of low Z neighbours (e.g. O or C) to the EXAFS. This enables the emphasis of the Pt or Ru scatterers in the first coordination sphere.

3.1 Pt L_{III} edge

3.1.1 Pt/C and Pt foil

Figure 1 shows the k^3-weighted EXAFS data recorded at the Pt L_{III} edge and the corresponding Pt phase corrected Fourier transform (FT) in panels (a) and (b), respectively, for a Pt foil and the Pt/C catalyst.

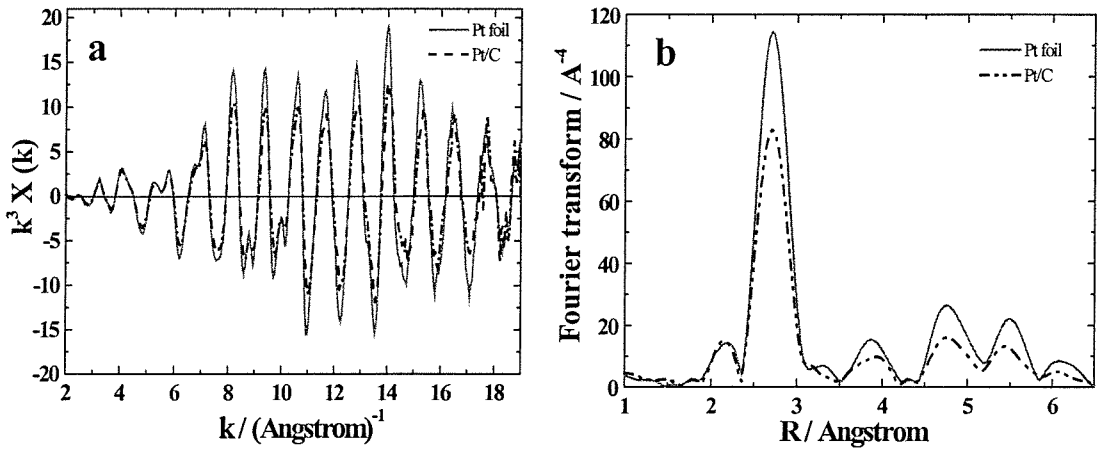

Figure 1 : (a) k^3-weighted experimental data at the Pt L_{III} edge for Pt/C (dotted line) recorded at - 0.6 V *vs.* MMS in 1 mol dm^{-3} H_2SO_4 at RT and for the Pt foil (solid line). (b) k^3-weighted Pt phase corrected Fourier Transform of data of spectra (a).

The similarity between the functional form of the EXAFS amplitude measured from the reference and the Pt/C catalyst over the entire k range (Figure 1, panel (a)) reflects that the Pt center is coordinated predominantly to metal scatterers in the nanoparticles [10]. Also, a reduction in the backscattering amplitude can be clearly seen for the Pt/C compared to the foil. The radial distribution function obtained by Fourier transformation of the EXAFS data of the Pt/C describes similar shell features up to about 5.5 Å compared to that of the Pt

reference (Figure 1, panel (b)). Therefore, the supported nanoparticles adopt the cubic face centered (*fcc*) structure. However, over the entire *R* range the magnitude of the FT decreases for the supported platinum particles compared to that of the Pt reference. The first backscattering shell due to Pt is characterised by two features: a main peak at 2.76 Å and a short distance peak at 2.15 Å. The latter does not correspond to a real metal bond distance (Pt-X), but is inherent to scattering by Pt neighbours in the first shell.

The structural parameters extracted from the EXAFS data using a *fcc* model structure are listed in Table 2 and 3 and a comparison is sketched in Figure 2. Smaller coordination numbers and similar interatomic distances have been fitted for Pt/C compared to that of Pt reference, i.e. $N1_{(Pt\text{-}Pt)r} = 12$ against $N1_{(Pt\text{-}Pt)Pt/C} = 9$. This is consistent with the decrease in amplitude observed previously in the Chi(*k*) and the FT plots. Thereby, Pt/C consists of smaller particles compared to that of bulk platinum.

SHELLS		N	R / Å	$2\sigma^2$ / Å^2
1	Pt-Pt	12	2.765 (0.001)	0.011 (0.001)
2	Pt-Pt	6	3.908 (0.011)	0.015 (0.002)
3	Pt-Pt	24	4.803 (0.006)	0.016 (0.001)

Table 2 : Structural parameters extracted from EXAFS data of Pt foil ; R :26%. (errors are given in brackets)

SHELLS		N	R / Å	$2\sigma^2$ / Å^2
1	Pt-Pt	9.1 (0.7)	2.755 (0.003)	0.011 (0.001)
2	Pt-Pt	4.4 (2.4)	3.912 (0.005)	0.016 (0.004)
3	Pt-Pt	7.1 (2.2)	4.798 (0.004)	0.012 (0.003)

Table 3 : Structural parameters extracted from EXAFS data of Pt/C ; R :23%.

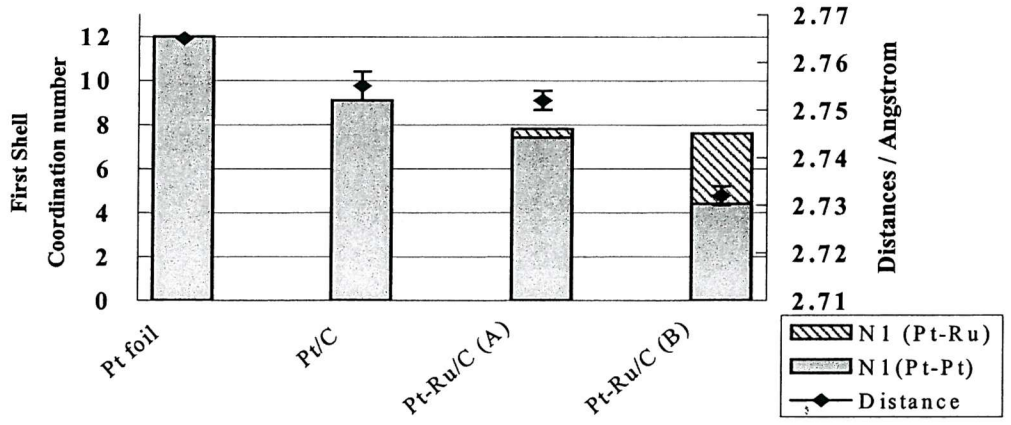

Figure 2 : Comparison of the first shell coordination number (*N1*) and the inter-atomic distance (R1(Pt-Pt)).

3.1.2 Pt/C and Pt-Ru/C

3.1.2.1 Pt-Ru/C (A)

The backscattering amplitude of the EXAFS data of the Pt-Ru/C (A) electrocatalyst is reduced along the entire *k* range compared to that of the Pt/C as shown in Figure 3, panel (a). This is particularly true for *k* values between 5 to 11 $Å^{-1}$.

The radial distribution function of the Pt-Ru/C (A) describes a similar fcc structure as that of Pt/C (Figure 3, panel (b)). Also, it is important to notice the absence of the 'satellite' peak at 2.15 Å for Pt-Ru/C (A) and the decreased amplitude along the entire *R* range.

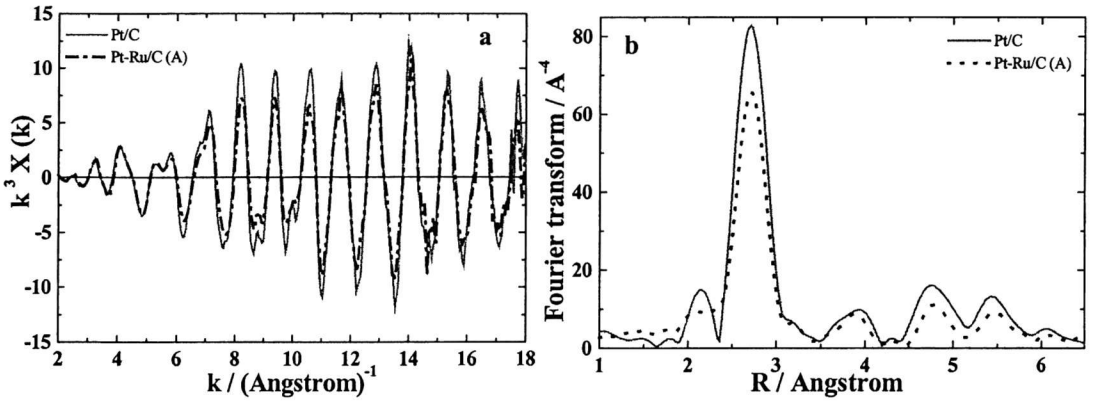

Figure 3 : (a) k^3-weighted experimental data at the Pt L_{III} edge for Pt/C (solid line) and Pt-Ru/C (A) (dotted line) recorded at – 0.6 V *vs.* MMS in 1 mol dm^{-3} H_2SO_4 at RT. (b) k^3-weighted Pt phase corrected Fourier Transform of data of spectra (a).

The best fits using a fcc model have been achieved with a heterometallic bonding (Pt-Ru) in the first shell (Table 4). This provides direct evidence of the formation of bimetallic nanoparticles. A smaller coordination number (e.g. $N1_{[(Pt\text{-}Pt)+(Pt\text{-}Ru)]}$: 7.8) and similar interatomic distances have been obtained compared to that of Pt/C (Table 2) as illustrated in Figure 2.

SHELLS		N	R / Å	$2\sigma^2$ / Å^2
1	Pt-Pt	7.4 (0.6)	2.752 (0.002)	0.012 (0.001)
2	Pt-Ru	0.4 (0.1)	2.689 (0.003)	0.003 (0.001)
3	Pt-Pt	3.1 (1.5)	3.897 (0.012)	0.016 (0.004)

Table 4 : Structural parameters extracted from EXAFS data of Pt-Ru/C(A) ; R : 22%.

3.1.2.2 Pt-Ru/C (B)

The k^3-weighted EXAFS data (Figure 4, panel (a)) and the corresponding Pt phase corrected FT (Figure 4, panel (b)) of the Pt-Ru/C (B) catalyst are dramatically different to those of Pt/C catalyst. Over the entire k range the backscattering amplitude is decreased. A phase shift is observed in the k range 5-11 Å^{-1} and a phase cancellation occurs at 10 Å^{-1}, which generates a node in the envelope curve (The envelope has been defined as the absolute part of the FT). Furthermore, the magnitude of the radial distribution function due to the metal scatterers around the Pt absorber is reduced significantly along the entire R range. The first shell dominant peak at 2.76 Å decreases to about 25% of its maximum and the short distance peak at 2.15 Å increases by around 50% over the Pt/C magnitude FT.

SHELLS		N	R / Å	$2\sigma^2$ / Å^2
1	Pt-Pt	4.4 (0.3)	2.732 (0.002)	0.011 (0.001)
2	Pt-Ru	3.2 (0.3)	2.710 (0.002)	0.013 (0.001)
3	Pt-Pt	1.9 (1.0)	3.850 (0.014)	0.017 (0.004)

Table 5 : Structural parameters extracted from EXAFS data for Pt-Ru/C(B) ; R : 25%.

The best fit of the EXAFS data was obtained with two (Pt-Pt) and one (Pt-Ru) contribution using a fcc model. The corresponding structural parameters are presented in Table 5. The average coordination number ($N(Pt\text{-}Ru)_{Pt\text{-}Ru/C(B)}$: 3.2) and the inter-atomic distance ($R(Pt\text{-}Ru)_{Pt\text{-}Ru/C(B)}$: 2.71 Å) reflect the large Ru contribution in the first coordination sphere. In addition, the (Pt-Pt) contribution in the first shell is defined by a smaller coordination number ($N_{Pt\text{-}Pt}$: 4.4) and shorter inter-atomic distance ($R_{Pt\text{-}Pt}$: 2.732 Å) compared to that of

the Pt/C (see Figure 2). Therefore, bimetallic particles with such rich Ru alloy content provide smaller Pt particles at the same Pt loading. Also, the interaction of Ru in the nanoparticle induces a distance contraction of the second (Pt-Pt) shell : $R(Pt\text{-}Pt)_{Pt/C}$: 3.91 Å compared to $R(Pt\text{-}Pt)_{Pt\text{-}Ru/C(B)}$: 3.85 Å.

The Pt-Ru/C (B) is, thus, a more well mixed alloy catalyst compared to that of Pt-Ru/C (A).

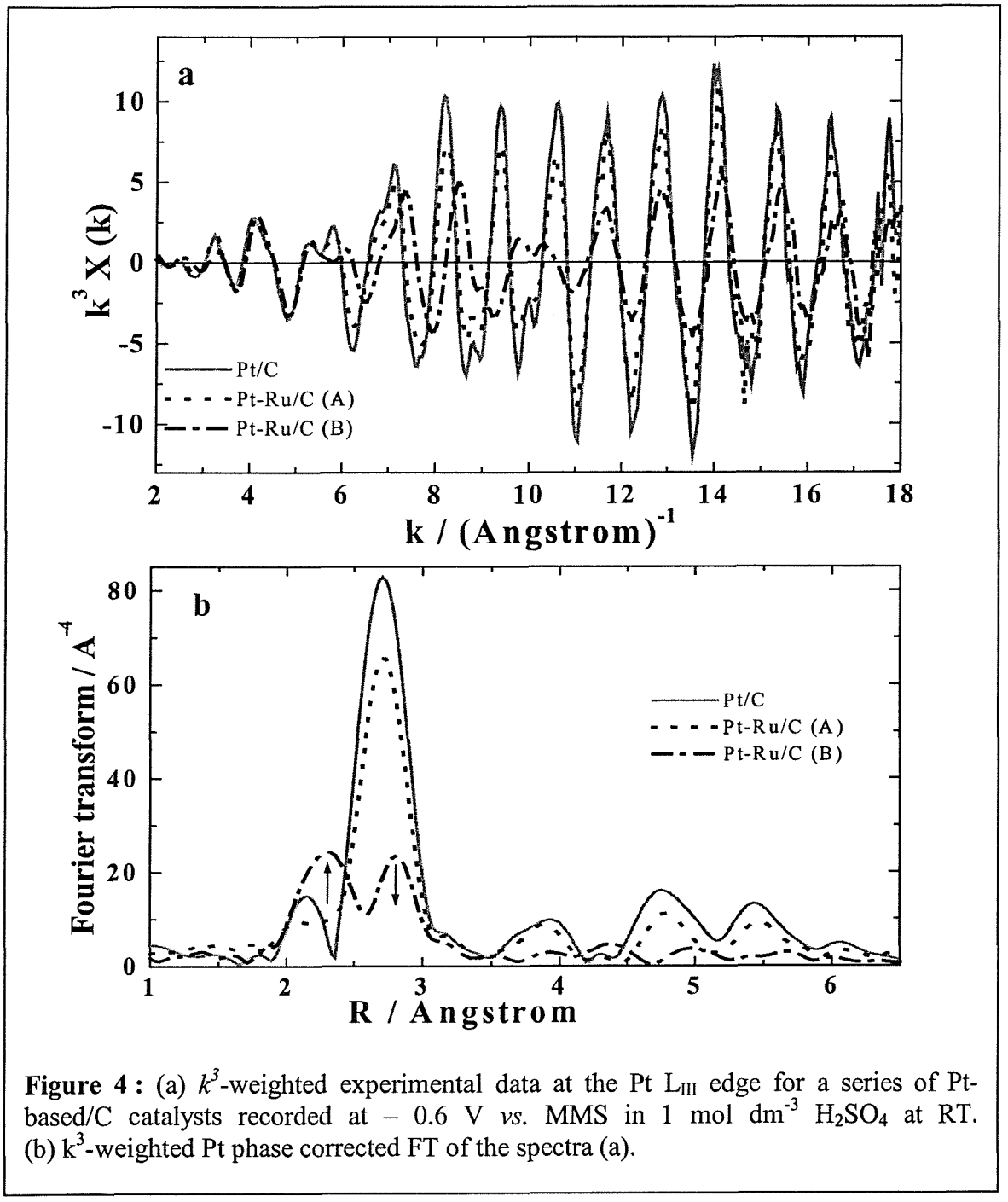

Figure 4 : (a) k^3-weighted experimental data at the Pt L_{III} edge for a series of Pt-based/C catalysts recorded at – 0.6 V *vs.* MMS in 1 mol dm^{-3} H_2SO_4 at RT. (b) k^3-weighted Pt phase corrected FT of the spectra (a).

Higher coordination spheres (i. e. R>3.5Å) illustrate a loss of Pt backscatterering character compared to that of the two previous catalysts. The fitting of the second Pt shell was obtained with rather large error values and a large Debye-Waller factor. The high surface atom composition gives rise to greater disorder (higher Debye-Waller factor) due to an increase of the surface vibrational amplitudes [11] and the presence of small fraction of non-fcc particles.

3.2 Ru K edge

To assess the uniformity of the intermixing of the alloying element in the nanoparticles, EXAFS data were also recorded at the Ru K edge. If the alloy is well mixed, the (Ru-Pt) first coordination shell should match that of the (Pt-Ru) for a (1 :1) alloy. The k^3-weighted EXAFS data of the Pt-Ru/C catalysts illustrate a large reduction in the backscattering amplitude compared to that of Ru powder (Figure 5). This is consistent with the small particle size in the catalysts and the low Ru content over the nominal composition of the catalyst. However, the functional form of the EXAFS amplitude suggests that Ru center is coordinated predominantly by metal scatterers in the nanoparticles. Also, no clear difference in phase or amplitude of the EXAFS data is observed between both Pt-Ru/C catalysts.

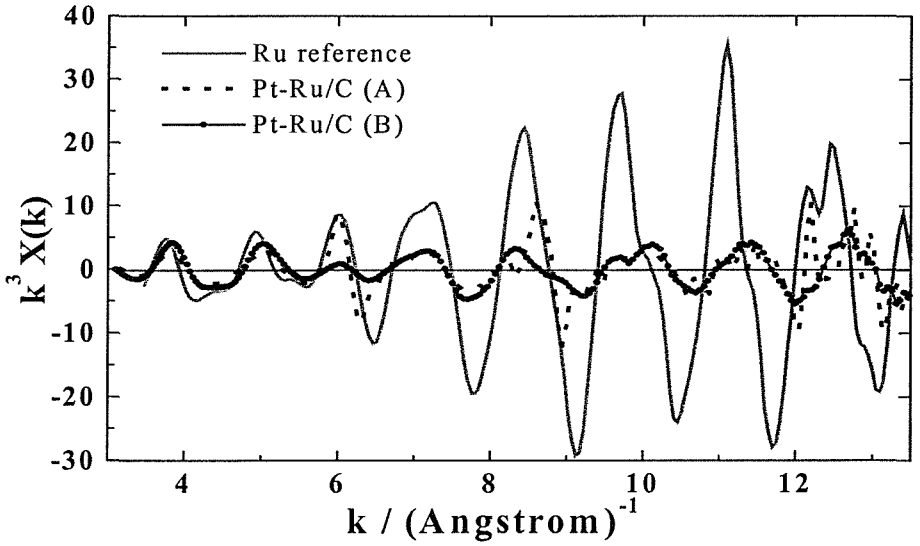

Figure 5 : k^3-weighted experimental data at the Ru K edge of Pt-Ru/C catalysts recorded at – 0.6 V *vs.* MMS in 1 mol dm^{-3} H_2SO_4 at RT and of Ru powder.

The k^3-weighted Ru phase corrected FTs of the EXAFS data are shown in Figure 6. To aide comparison with the Pt-Ru alloy supported catalysts, the FT of the Ru powder spectrum was scaled down by a factor of 4.5. Over the entire R range significant changes in the radial distribution around the Ru center atom are observed (Figure 6). For the Ru powder a dominant first shell peak at 2.68 Å and two longer distance peaks at 3.78 Å and 4.75 Å were ascribed to the (Ru-Ru) contributions. This is consistent with the hexagonal close packed (hcp) structure of Ru metal and the structural parameters extracted listed in Table 6.

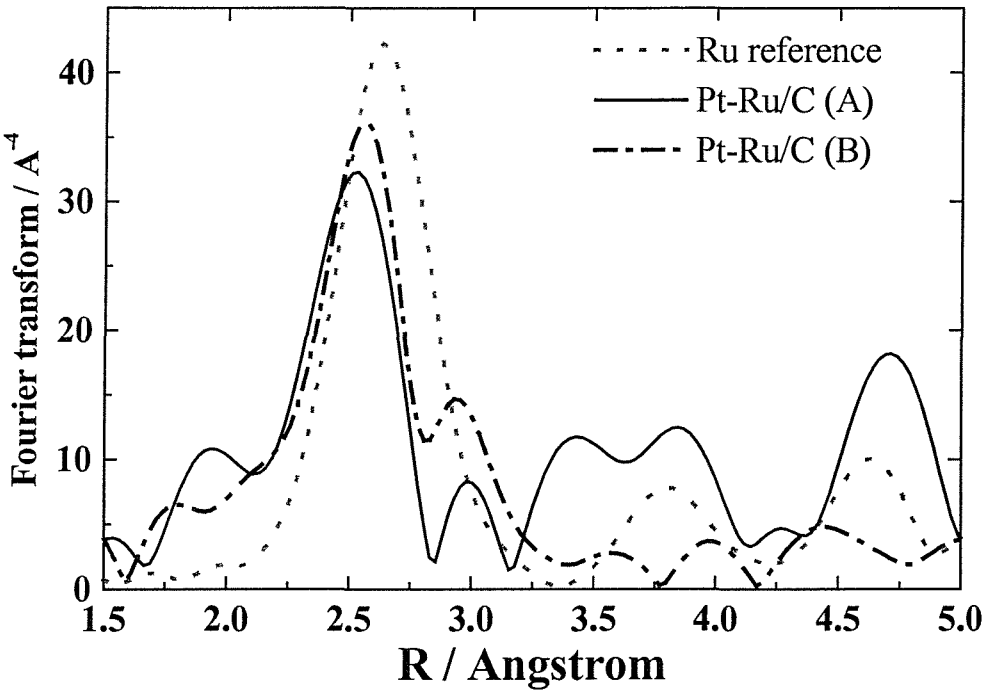

Figure 6 : k^3-weighted Ru phase corrected Fourier Transforms of the data shown in Figure 5. Note that the amplitude of FT for the Ru reference has been divided by a factor of 4.5 for comparison.

A longer distance peak in the first coordination shell (i.e. 2.94 Å) is visible for the Pt-Ru supported on carbon nanoparticles. This peak related to the apparent splitting of the first shell peak, where the position of the maximum shifts slightly towards shorter distances (i.e. 2.5 Å). This phenomenom is more pronounced for the Pt-Ru/C (A) than for Pt-Ru/C(B), where Ru was found more alloyed to Pt at Pt L_{III} edge.

The best fits of the EXAFS data for both catalysts were achieved with the heterometallic contribution (Ru-Pt) in the first coordination sphere (Table 7 and Table 8). In this, N(Ru-Pt) = 0.9 for Pt-Ru/C (A) and N(Ru-Pt) = 3.5 for Pt-Ru/C (B). A higher average

coordination number was found at the Ru K edge compared to that of Pt L_{III} edge for the sample (A). Furthermore, the fit of the EXAFS data was completed with a R_{EXAFS} value which was rather high, i.e. $R_{EXAFS} = 77\%$. This is caused by the poor data quality and the low Ru content in the sample itself. In constrast, the average coordination number at the Ru K edge for the sample (B) is consistent with that determined at the Pt L_{III} edge, i.e. N(Ru-Pt) = 3.5 against N(Pt-Ru) = 3.2, respectively.

The higher coordination shells exhibit significant distortion compared to that of the Ru powder and were difficult to fit.

SHELLS		N	R / Å	$2\sigma^2$ / Å^2
1	Ru-Ru	12	2.678 (0.002)	0.010 (0.001)
2	Ru-Ru	6	3.784 (0.003)	0.011 (0.002)

Table 6 : Structural parameters extracted from EXAFS data recorded at Ru K edge for the Ru reference ; R : 37%.

SHELLS		N	R / Å	$2\sigma^2$ / Å^2
1	Ru-Ru	4.1 (1.2)	2.658 (0.026)	0.015 (0.001)
2	Ru-Pt	0.9 (1.5)	2.688 (0.040)	0.005 (0.005)

Table 7 : Structural parameters extracted from EXAFS data recorded at Ru K edge for Pt-Ru/C(A) at – 0.6 V *vs.* MMS ; R : 77%.

SHELLS		N	R / Å	$2\sigma^2$ / Å^2
1	Ru-Ru	3.9 (0.6)	2.652 (0.005)	0.014 (0.002)
2	Ru-Pt	3.5 (0.6)	2.699 (0.005)	0.002 (0.001)

Table 8 : Structural parameters extracted from EXAFS data recorded at Ru K edge for Pt-Ru/C(B) at – 0.4 V *vs.* MMS ; R : 31%.

4 DISCUSSION

The results presented above have shown interference between Ru and Pt in the EXAFS spectrum at the Pt L_{III} edge and the Ru K edge. The apparent splitting of the first shell peak

in the FT can be regarded as a fingerprint of the presence of a heterometallic contribution in the first coordination sphere. In order to understand this phenomenom simulations have been conducted at both edges. To emphasize the interaction of the heterometallic contribution in the first coordination sphere, a Fourier filter was applied over a restricted range of *R*, 1.5 - 3.2 Å. The variation of the metallic composition between Pt and Ru was adjusted for an average coordination number of 8 atoms. This value corresponds to the average number of neighbours in the first shell for the Pt/C catalyst. This model was produced at fixed interatomic distances such that Pt-Pt = 2.77 Å, Ru-Ru = 2.68 Å and Pt-Ru = 2.71 Å.

4.1 Simulation at the Pt L_{III} edge

The simulated k^3-weighted EXAFS data of the isolated first shell are presented in Figure 7 and the corresponding phase uncorrected, Pt phase corrected and Ru phase corrected FTs are presented in Figure 8 A, B and C, respectively.

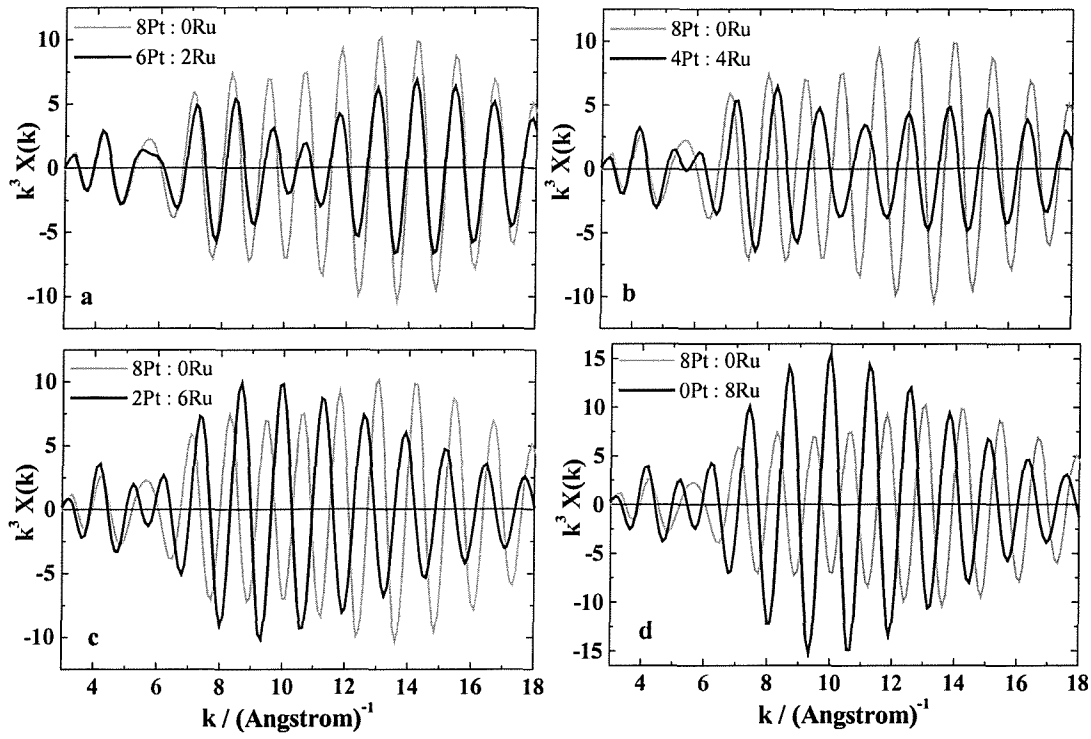

Figure 7 : Comparison of simulated k^3-weighted Chi(k) data for different Pt and Ru compositions in the first coordination sphere.

The presence of Ru backscatterers in the first shell reduces the Chi(k) plot amplitude between 9 and 11 $Å^{-1}$ in particular and to a lesser extent at higher k values (i. e. $k > 11$ $Å^{-1}$) (Figure 7, panel (a)). The general reduction in amplitude of the Chi(k) plot has been attributed to the difference in backscattering amplitude from the two neighbours, Pt and Ru. The theoretical values of the backscattering amplitude reported by Teo and Lee [12] have been plotted as shown in Figure 9. As the magnitude of the backscattering amplitude of Ru is greater than that of Pt at low k, a larger fraction of Ru in the first coordination sphere will contribute to an increase in the Chi(k) amplitude (Figure 7, panels (c) and (d)) in the region $k < 12$ $Å^{-1}$.

The theoretical values of the backscattering phase shift from Pt and Ru are plotted in Figure 10. These values are valid at a fixed distance, equal to the covalent bond distance of the pure element Ru-Ru and Pt-Pt. At about k ~10 $Å^{-1}$ the phase shifts differ by approximately π radians. This causes a near cancellation of the backscattering from the two neighbour types. This phenomenom is most pronounced for a number of Ru neighbours representing the 1/3 of the first coordination sphere as represented in Figure 7, panel (a). Moreover, for an equal numbers of Pt and Ru neighbouring atoms in the first cordination shell the period of the EXAFS oscillations is seen to change (Figure 7, panel (b)). The reduction in amplitude and phase cancellation are consistent with the experimental EXAFS data shown previously in Figure 4, in panel (a).

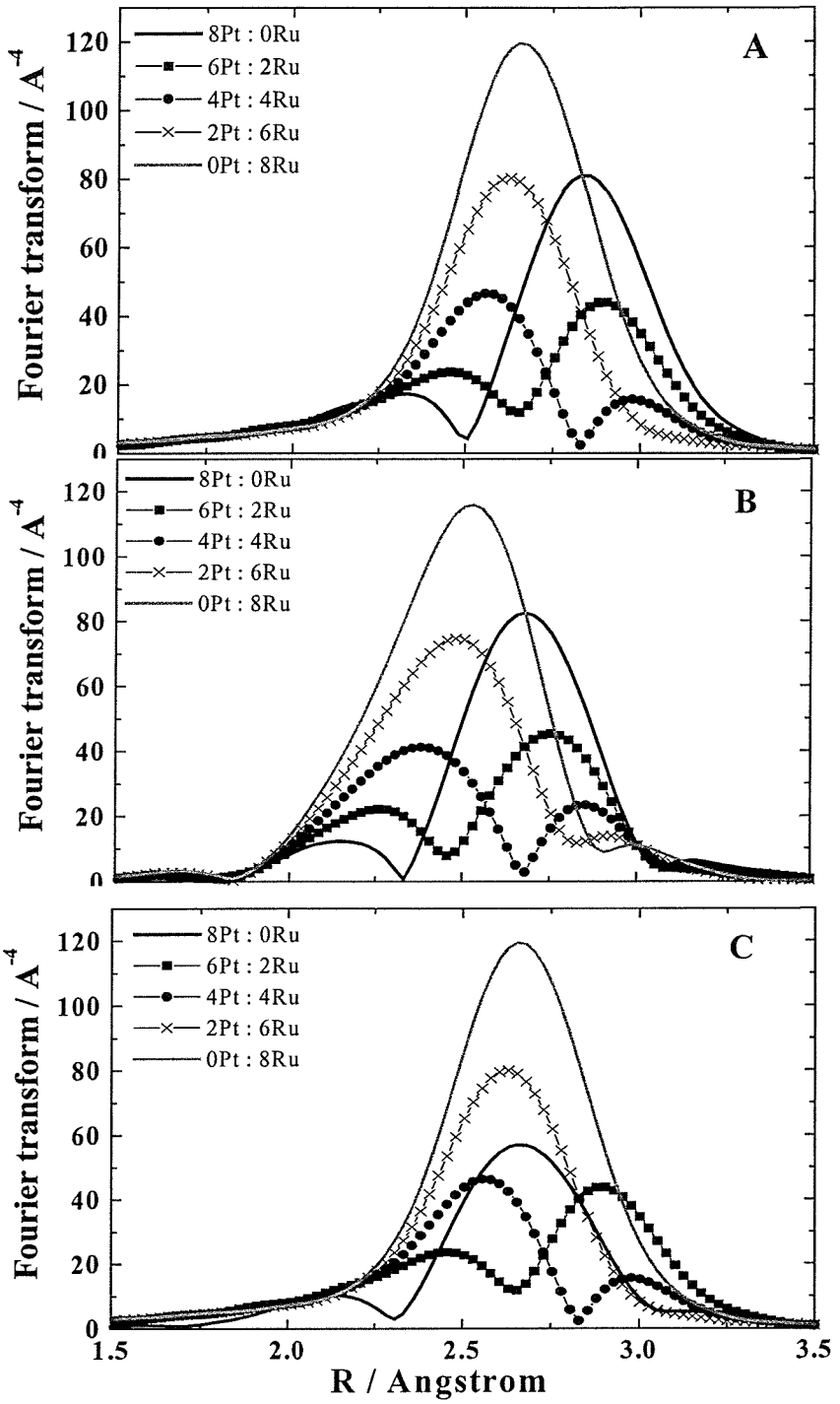

Figure 8 : k^3-weighted Fourier Transform at Pt the L_{III} edge of simulated EXAFS spectra ; (A) phase uncorrected ; (B) Pt phase corrected ; (C) Ru phase corrected.

	PEAK POSITION / Å					
Atomic ratio (Pt : Ru)	**Pt phase correction**		**Ru phase correction**		**No phase correction**	
8 : 0	2.16	2.68	2.16	2.67	2.34	2.84
6 : 2	2.26	2.76	2.45	2.89	2.45	2.89
4 : 4	2.38	2.84	2.56	2.98	2.56	2.98
2 : 6	2.48	2.92	2.63	/	2.63	/
0 : 8	2.53	2.99	2.66	/	2.66	/

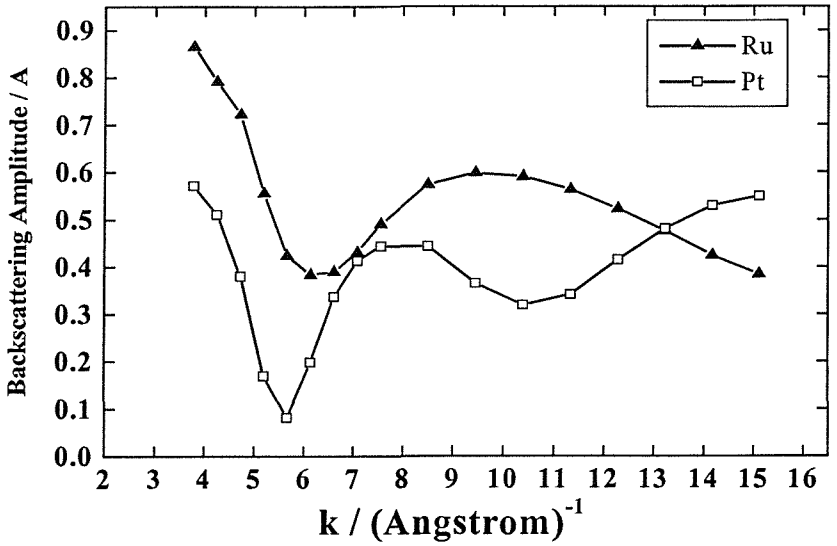

Figure 9 : Theoretical backscattering amplitude for Pt and Ru atom after Teo and Lee [12].

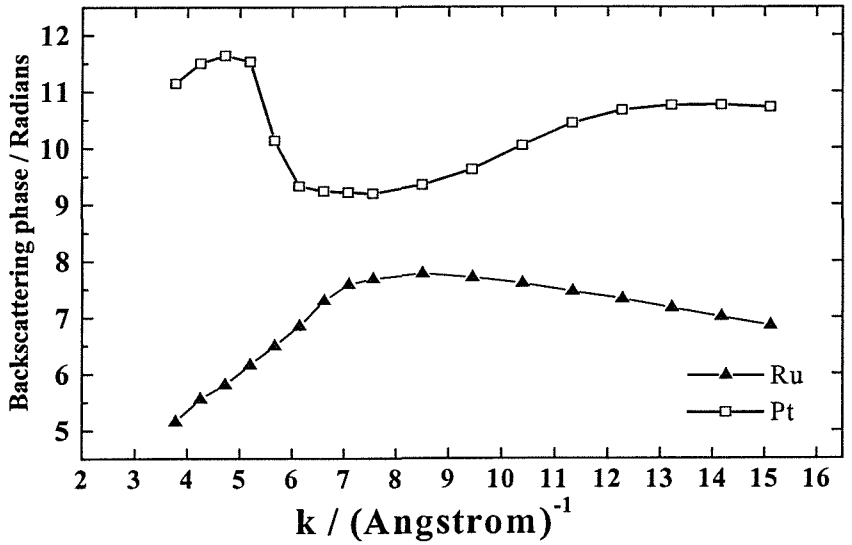

Figure 10 : Theoretical backscattering phase of Ru and Pt atom after Teo and Lee [12].

4.2 Simulation at the Ru K edge

Similar to that of Pt L_{III} edge data, simulations were performed at the Ru K edge. The gradual increase of the number of Pt atoms coordinated to a Ru center absorber atom gives rise to a significant decrease in the scattering amplitude in the *k* range 5 – 10 $Å^{-1}$ (Figure 11, panel (a)) and then to a phase shift (Figure 11, panel (b)). Panels (c) and (d) illustrate that larger (Ru-Pt) contributions provide a phase shift and an increase in amplitude over the

entire k range. The experimental Chi(k) plots (Figure 5) do not show such drastic changes as the Ru content in the bimetallic particles remains low compared to that of the Ru powder.

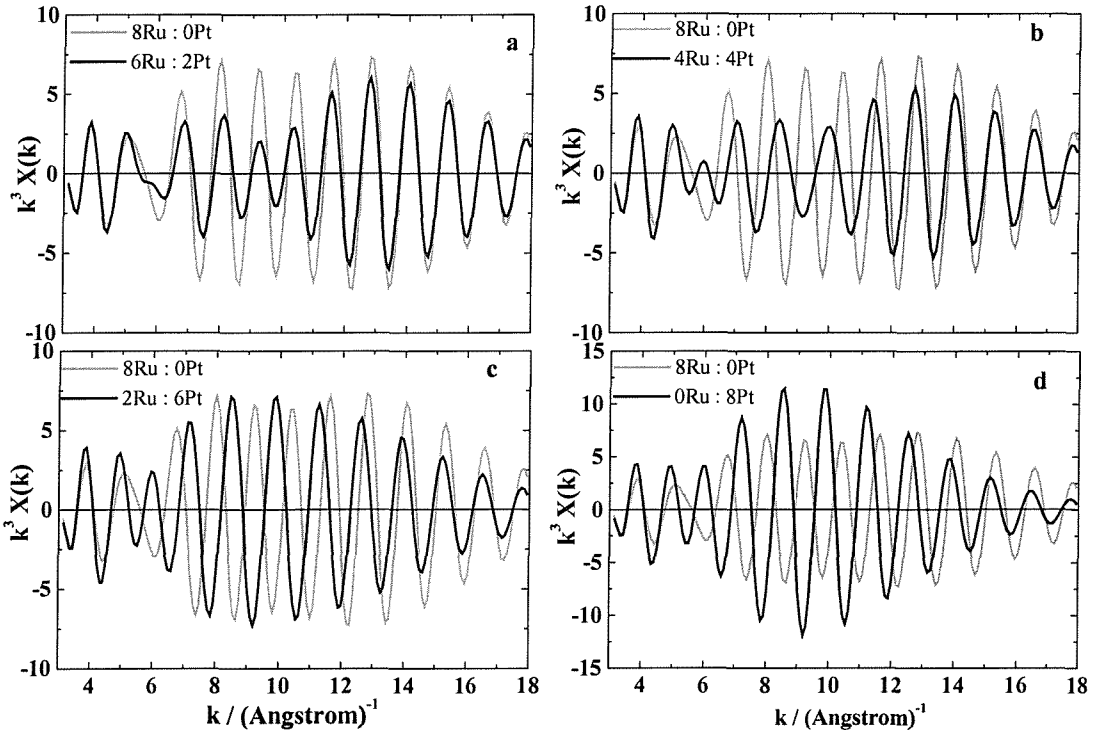

Figure 11 : Comparison of k^3-weighted Chi(k) plot at the Ru K edge for different compositions of Pt and Ru in the first coordination sphere.

The k^3-weighted phase uncorrected FT (Figure 12 A) clearly shows a splitting of the first shell peak as the (Ru-Pt) contribution becomes greater in the first coordination shell. The original dominant peak at 2.68 Å splits in two peaks (i. e. 2.3 and 2.7 Å) and finally appears as one peak at 2.4 Å. The origin of this apparent splitting is attributed to phase cancellation by scattering from the two neighbour types. As seen in Figure 11, a phase cancellation in the Chi(k) occurs at k = 6 $Å^{-1}$ and 9 $Å^{-1}$. Unlike the simulation at the Pt L_{III} edge, the radial distribution is quite sensitive to the phase correction applied.

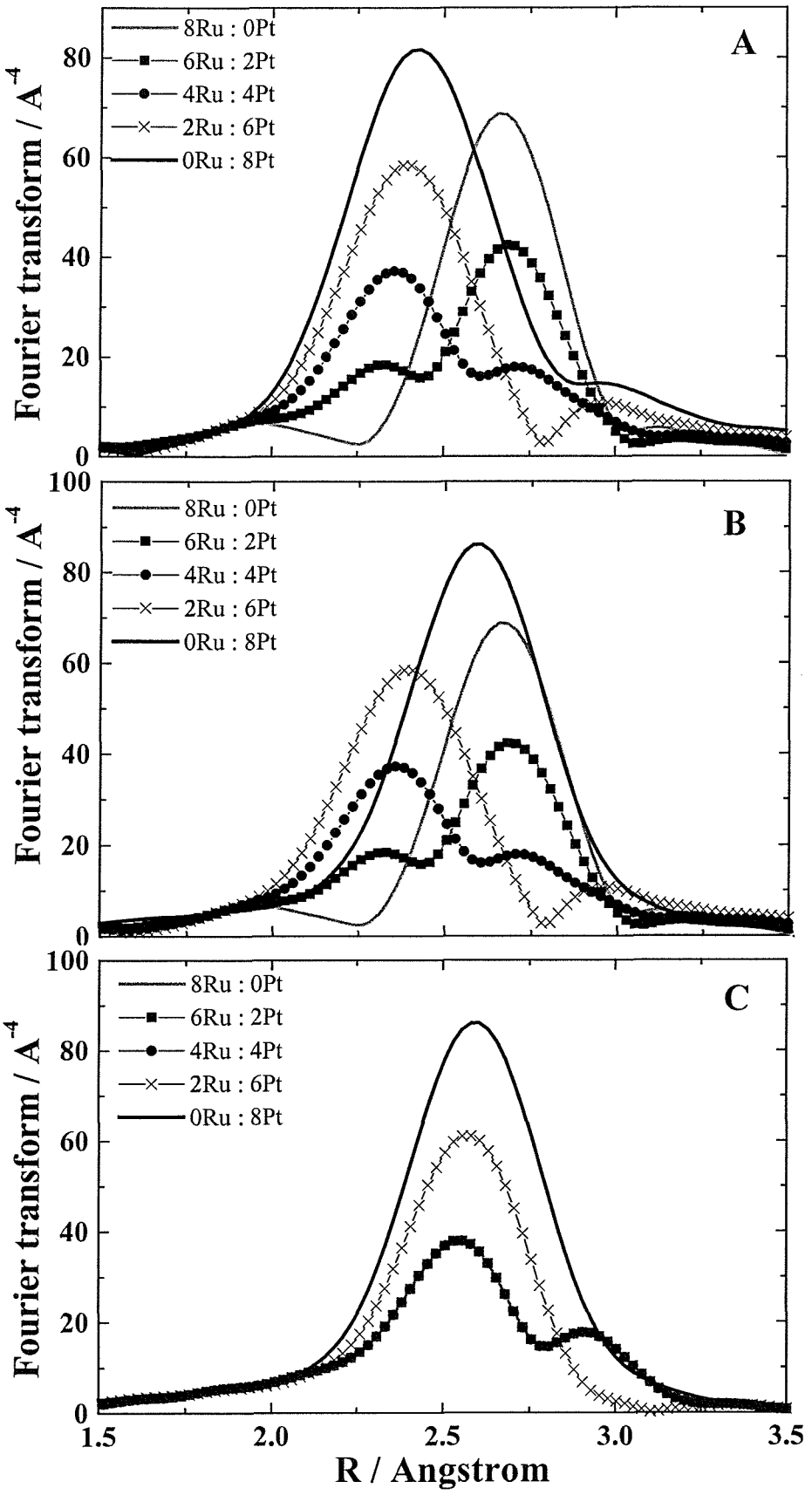

Figure 12 : k^3-weighted Fourier Transform at Ru K edge ; (A) phase uncorrected ; (B) Ru phase corrected ; (C) Pt phase corrected, with 8 Ru, 6 Ru and 4 Ru having the same radial distribution in the graph (C).

	PEAK POSITION / Å					
Atomic ratio (Ru : Pt)	**Ru phase correction**		**Pt phase correction**		**No phase correction**	
8 : 0	2.00	2.67	2.55	2.92	2.00	2.67
6 : 2	2.32	2.69	2.55	2.92	2.32	2.69
4 : 4	2.32	2.72	2.55	2.92	2.36	2.72
2 : 6	2.39	2.96	2.57	/	2.40	2.97
0 : 8	2.60	/	2.60	/	2.43	/

Table 9 : Peak positions from the k^3-weighted Fourier transforms of the simulated EXAFS data at the Ru K edge.

5 CONCLUSION

The interference between Ru and Pt in the EXAFS spectrum of Pt-Ru bimetallic particles has been evidenced at both edges, i. e. Pt L_{III} and Ru K edge. The apparent splitting of the first coordination shell of the Fourier transform is not simply related to the presence of a second neighbour distance within the shell (i.e. Pt-Ru and Ru-Pt contribution). Instead, the splitting is caused by phase cancellation of the EXAFS around 10 $Å^{-1}$. At this energy the backscattering from the Pt and Ru neighbours are about 180° out of phase with one another. The results illustrate the necessity of full analysis of the EXAFS data in assigning peaks in the Fourier transform to real coordination distances. However, the results also demonstrate that an observation of splitting of the first shell peak may be used as a quick 'finger print' of a more well mixed PtRu alloy. The finger print is more clear when the EXAFS data is obtained at Pt L_{III} edge, as the shape of the Fourier transform is less sensitive to the phase correction applied.

6 REFERENCES

[1] Herron, M. E.; Doyle, S. E.; Pizzini, S.; Roberts, K. J.; Robinson, J.; Hards, G.; Walsh, F. C., *J. Electroanal. Chem.*, **1992**, *324*, 243.

[2] Weber, R. S.; Peickert, M.; DallaBetta, R. A.; Boudart, M., *J. Electrochem. Soc.*, **1988**, *135*, 2535.

[3] Chang, J.-R.; Lee, J.-F.; Lin, S. D.; Lin, A. S., *J. Phys. Chem. B*, **1995**, *99*, 14798.

[4] Mukerjee, S.; Srinivasan, S.; Soriaga, M. P.; McBreen, J., *J. Phys. Chem. B*, **1995**, *99*, 4577.

[5] Mukerjee, S.; Srinivasan, S.; Soriaga, M. P.; McBreen, J., *J. Electrochem. Soc.*, **1995**, *142*, 1409.

[6] Mukerjee, S.; McBreen, J., *J. Electrochem. Soc.*, **1996**, *143*, 2285.

[7] McBreen, J.; Mukerjee, S., *J. Electrochem. Soc.*, **1995**, *142*, 3399.

[8] Borgna, A.; Stagg, S. M.; Resasco, D. E., *J. Phys. Chem. B*, **1998**, *102*, 5077.

[9] Binsted, N., Excurv98: Computer programme CCLRC Daresbury Laboratory, 1998.

[10] Koninsberger, D. C.; Prins, R., *X-Ray Absorption: Principles, Applications, Techniques of EXAFS, SEXAFS, and XANES*; Wiley: New York, 1988.

[11] Marques, E. C.; Sandstrom, D. R.; Lytle, F. W.; Greegor, R. B., *J. Chem. Phys.*, **1982**, *77*, 1027.

[12] Teo, B.-K.; Lee, P. A., *J. Am. Chem. Soc.*, **1979**, *101*, 2815.

CHAPTER 4 : POTENTIAL DEPENDANCE OF THE EXAFS OF PT-BASED FUEL CELL CATALYSTS.

1 INTRODUCTION

The study of the structure and the morphology of small metal particles of the order of 10 Å in size is a difficult task, but is of major importance for the catalysis field as the activity and selectivity of small metal crystal particles depends on the surfaces involved in the reaction. The most appropiate tools used include high resolution electron microscopy (HREM), to yield information on the atomic arrangement and the nature of defect structures such as twin planes and stacking faults, and transmission electron microscopy (TEM), to yield information about morphology and surfaces in projection [1]. HREM studies of Ru clusters prepared on a carbon support have demonstrated these to be in both hexagonal close packed and cubic close packed structures [2]. Bimetallic clusters are commonly used in the heterogeneous catalysis technology. The inhomogeneity of these catalysts due to the segregation of one of the components creates difficulty in probing their structure. Therefore, atomic core electron spectroscopy is required to characterise such species. For instance, Liang *et al* .[3] have demonstrated the presence of Re in the fcc form through the study of the Pt-Re supported on silica using anomalous X-Ray diffraction with a synchrotron radiation source. The formation of the new structure of Re has been explained by the epitaxial growth of Re on Pt. Duff *et al.* have reported the usefulness of using combined HREM and EXAFS techniques for the study of colloidal platinum [4]. Indeed, whereas the contraction of the Pt-Pt coordination distance for small platinum particles in solution was observed using EXAFS, the information of short range defects and minority structure were seen using the HREM technique.

The poorly crystallised materials that are often used in battery and fuel cell applications exhibit weak or even no X-ray diffraction patterns. Therefore, EXAFS appears as the most suitable tool to yield short range information [5]. The shape, structure and size of these nanoparticles may be easily determined using the EXAFS technique and it provides complementary informations to the XRD technique which provides long range information.

In the previous chapter, it has been clearly shown that the EXAFS technique allows the evaluation of the degree of alloying of the secondary metal, M, to Pt in the carbon supported nanoparticles. The difference in the backscattering phase and amplitude between the two atoms with similar distances disrupts the symetrical feature of the main peak in the Fourier transform. Also, the efficacity of the EXAFS technique is based on the possibility of studying the fuel cell material under electrochemical conditions. Therefore, the aim of this chapter is to study the effect of the electrode potential on the structure of the homometallic and bimetallic carbon supported particles used in the anode of the polymer electrolyte fuel cell. Furthermore, the geometrical parameters will be complimented by an electronic investigation using white line analysis.

2 EXPERIMENTAL

2.1 Materials

A series of platinum-based supported on carbon electrocatalysts, Pt/C, PtRu/C and PtMo/C, were supplied by Johnson Matthey and are referenced in Table 1, with their corresponding nominal metallic composition and XRD parameters.

Catalyst powders were formulated into anode fuel cell electrodes using the experimental procedure described in Chapter 2, section 2.2. Prior to XAS measurements, electrodes were

boiled in triply distilled water to ensure a fully flooded state, and, thus, good ionic conductivity through the solid polymer electrolyte.

	COMPOSITION		XRD PARAMETERS	
CATALYSTS	wt. %Pt	wt. %M*	Crystallite size /nm	Lattice parameter / Å
Pt/C	40	/	4.0	3.92
Pt-Ru/C (A)	40	20	3.2	3.90
Pt-Ru/C (B)	40	20	2.4	3.86
Pt-Mo/C	40	20	2.4	3.92
Pt-MoO_x/C	40	5	2.9	3.91

Table 1 : Nominal metal loading (wt.%) of the carbon supported catalysts and the corresponding XRD parameters. (M^*) is secondary metal corresponding to either Ru or Mo.

2.2 XAS experiments

In situ (i.e. electrochemically treated catalyst) and *ex situ* (i.e. as prepared catalyst powder) EXAFS experiments were conducted on wiggler station 9.2 at Daresbury Laboratory, as described in Chapter 2, section 6.4.4. Data were recorded at the Pt L_{III} and L_{II} edges using the transmission detection mode and at the Mo K edge using the fluorescence detection mode. The Ru K edge data were presented in the previous chapter and will be referred to in the discussion in this chapter.

2.3 Data analysis

The smooth background was removed from the EXAFS spectra using the EXBROOK program and the structural parameters were extracted from the normalised spectra using EXCURV98 program [6], as explained in Chapter 2, section 6.3.

White line analysis was done using the XDAP program [7] and the method for the white line calculation will be described below in section 3.2.1.

3 RESULTS

3.1 EXAFS of the electrocatalysts as function of potential

EXAFS spectra were collected at different potentials in order to investigate the influence of the electrode potential on the structure of the electrocatalysts. The potential was set to the following values : - 0.6, - 0.4, - 0.1 and 0.3 V vs. MMS, to correspond to the hydride region, the post-hydride region, the double layer region and the oxide region, respectively. The electrochemical reactions occuring at these different potentials have been explained previously for a platinum based electrode cycled in an acidic medium in Chapter 2, Figure 2. The cyclic voltammograms for the Pt-M/C electrodes (where M = Ru or Mo) are presented in Figure 1 and will be studied in more detail later in Chapter 6. Though less resistive, these CVs are representative of those recorded in the thin layer electrochemical cell XAS cell. However, the major electrochemical feature of these carbon supported bimetallic catalysts is the presence of a large pseudo-capacitance over the entire potential range. This phenomenom is caused by the redox process that occurs on the oxidised M element. This is most pronounced for the Pt-Ru/C catalyst and to a lesser extent for the Pt-Mo/C catalyst. In addition, a first reversible electrochemical system at – 0.65 V vs. MMS and a second at – 0.3 V vs. MMS which are related to the desorption of the molybdenum hydride bronze H_yMoO_x of the lattice that could be formed by the 'spillover' of hydrogen from Pt sites to Mo [8] (Equation 1a) and the Mo(VI)/Mo(IV) redox couple (Equation 1b), characterise the Pt-Mo/C electrode cycled in 1 mol dm^{-3} sulfuric acid.

$$H_xMoO_3 \rightarrow MoO_3 + x\,H^+ + x\,e^- \qquad \text{Equation 1a}$$

$$MoO_3 + 4\,H^+ + 4\,e^- \rightarrow MoO_2 + 2\,H_2O \qquad \text{Equation 1b}$$

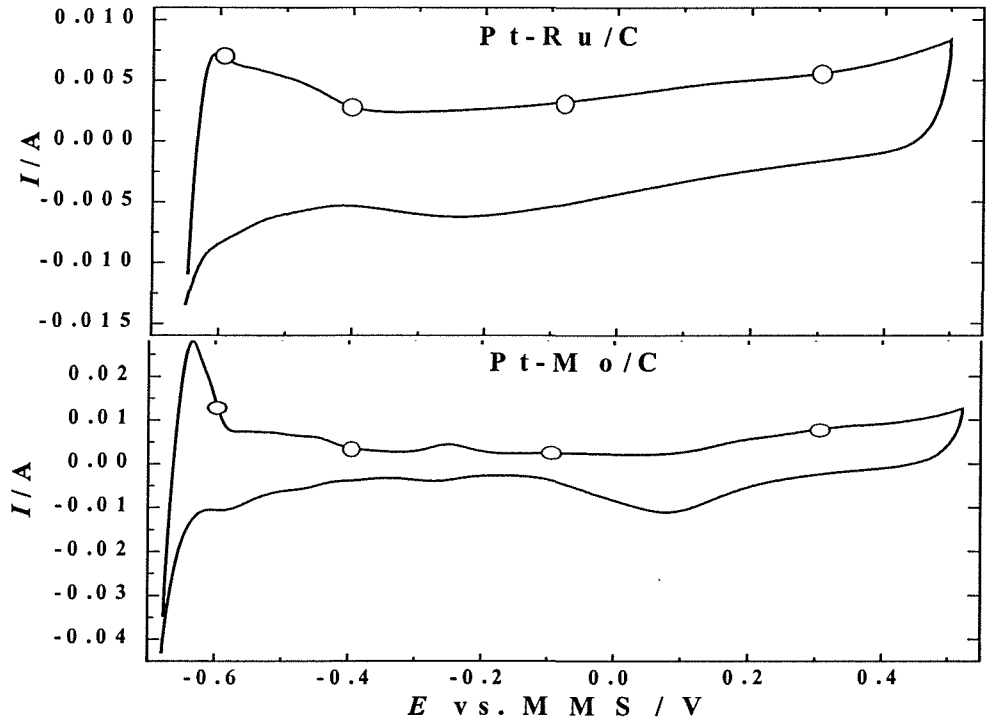

Figure 1 : Cyclic voltammogram of a Pt-Ru/C electrode (top) and a Pt-Mo/C electrode (bottom) in 1 mol dm^{-3} H_2SO_4 at 80°C at a scan rate of 10 mV s^{-1}. The symbols indicate the potentials where the EXAFS spectra were recorded.

The structural parameters, i.e. coordination numbers (N), interatomic distances (R) and disorder parameter ($2\sigma^2$), extracted from the EXAFS data recorded at the Pt L_{III} edge for the carbon supported Pt, Pt-Ru(A), Pt-Ru(B), Pt-Mo and Pt-MoO_x electrodes are presented, overleaf, as function of potential in Tables 2, 3 ,4, 5 and 6, respectively. Also, Figure 2, 3, 4, 5 and 6 show the k^3-weighted experimental data and the corresponding Pt phase corrected FTs at - 0.6 V (in panels (a) and (b)) and at 0.3 V (in panels (c) and (d)) for each of the catalysts; the solid lines correspond to the experimental data and the dotted lines to the fits.

POTENTIAL / V VS. MMS	SHELLS		N	R / Å	$2\sigma^2$ / Å^2
- 0.6	**1**	**Pt-Pt**	**9.1 (0.7)**	**2.755 (0.003)**	**0.011 (0.001)**
R : 23%	2	Pt-Pt	4.4 (2.4)	3.912 (0.005)	0.016 (0.004)
E_f : - 12 eV	3	Pt-Pt	7.1 (2.2)	4.798 (0.004)	0.012 (0.002)
- 0.4	**1**	**Pt-Pt**	**8.6 (0.7)**	**2.757 (0.002)**	**0.011 (0.001)**
R : 23%	2	Pt-Pt	4.2 (2.3)	3.912 (0.013)	0.016 (0.004)
E_f : - 12 eV	3	Pt-Pt	7.4 (2.3)	4.795 (0.006)	0.013 (0.002)
- 0.1	**1**	**Pt-Pt**	**8.4 (0.7)**	**2.760 (0.003)**	**0.011 (0.001)**
R : 22%	2	Pt-Pt	3.6 (2.2)	3.912 (0.013)	0.015 (0.005)
E_f : -13 eV	3	Pt-Pt	7.3 (2.1)	4.797 (0.006)	0.012 (0.002)
+ 0.3	**1**	**Pt-Pt**	**8.2 (0.7)**	**2.760 (0.003)**	**0.011 (0.001)**
R : 25%	2	Pt-Pt	3.6 (2.1)	3.912 (0.067)	0.015 (0.005)
E_f : -13 eV	3	Pt-Pt	7.9 (2.6)	4.799 (0.006)	0.013 (0.002)
	4	Pt-O	0.2 (0.5)	2.018 (0.146)	0.020 (0.070)

Table 2 : Fit parameters for the Pt/C electrode as a function of potential.

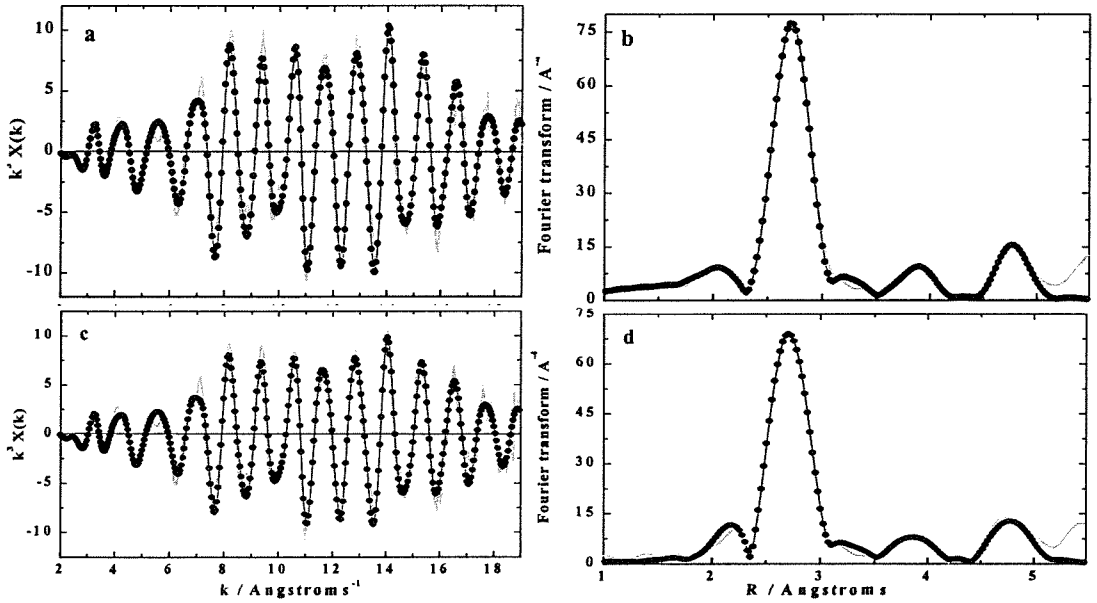

Figure 2 : (a) and (c) k^3-weighted experimental data for Pt/C electrode in 1 mol dm^{-3} H_2SO_4 at – 0.6 V and 0.3 V, respectively (solid line) and fits (dotted line). (b) and (d) Pt phase corrected Fourier transforms of the data and fits of spectra in (a) and (c).

POTENTIAL / V VS. MMS	SHELLS		N	R / Å	$2\sigma^2$ / Å^2
- 0.6	**1**	**Pt-Pt**	**7.4 (0.6)**	**2.752 (0.002)**	**0.012 (0.001)**
R : 22%	2	Pt-Ru	0.4 (0.1)	2.689 (0.003)	0.003 (0.001)
E_f : - 12 eV	3	Pt-Pt	3.1 (1.5)	3.897 (0.012)	0.016 (0.004)
	4	Pt-Pt	4.8 (1.8)	4.795 (0.007)	0.013 (0.002)
- 0.4	**1**	**Pt-Pt**	**7.8 (0.6)**	**2.747 (0.002)**	**0.013 (0.001)**
R : 22%	2	Pt-Ru	0.4 (0.1)	2.689 (0.003)	0.003 (0.001)
E_f : - 12 eV	3	Pt-Pt	2.3 (1.1)	3.891 (0.012)	0.013 (0.003)
	4	Pt-Pt	4.3 (1.8)	4.787 (0.007)	0.013 (0.003)
- 0.1	**1**	**Pt-Pt**	**7.8 (0.6)**	**2.750 (0.002)**	**0.013 (0.001)**
R : 22%	2	Pt-Ru	0.5 (0.1)	2.683 (0.003)	0.003 (0.001)
E_f : -12 eV	3	Pt-Pt	3.5 (1.7)	3.896 (0.010)	0.018 (0.003)
	4	Pt-Pt	4.4 (1.7)	4.797 (0.008)	0.013 (0.003)
+ 0.3	**1**	**Pt-Pt**	**7.0 (0.7)**	**2.757 (0.004)**	**0.012 (0.001)**
Ef : -12	2	Pt-Ru	0.9 (0.7)	2.713 (0.017)	0.012 (0.009)
R : 22%	3	Pt-Pt	2.2 (0.9)	3.910 (0.008)	0.012 (0.003)
E_f : - 12 eV	4	Pt-Pt	4.7 (1.8)	4.800 (0.008)	0.014 (0.003)
	5	Pt-O	0.2 (0.3)	2.010 (0.090)	0.020 (0.047)

Table 3 : Structural parameters for Pt-Ru/C (A) electrode as function of potential.

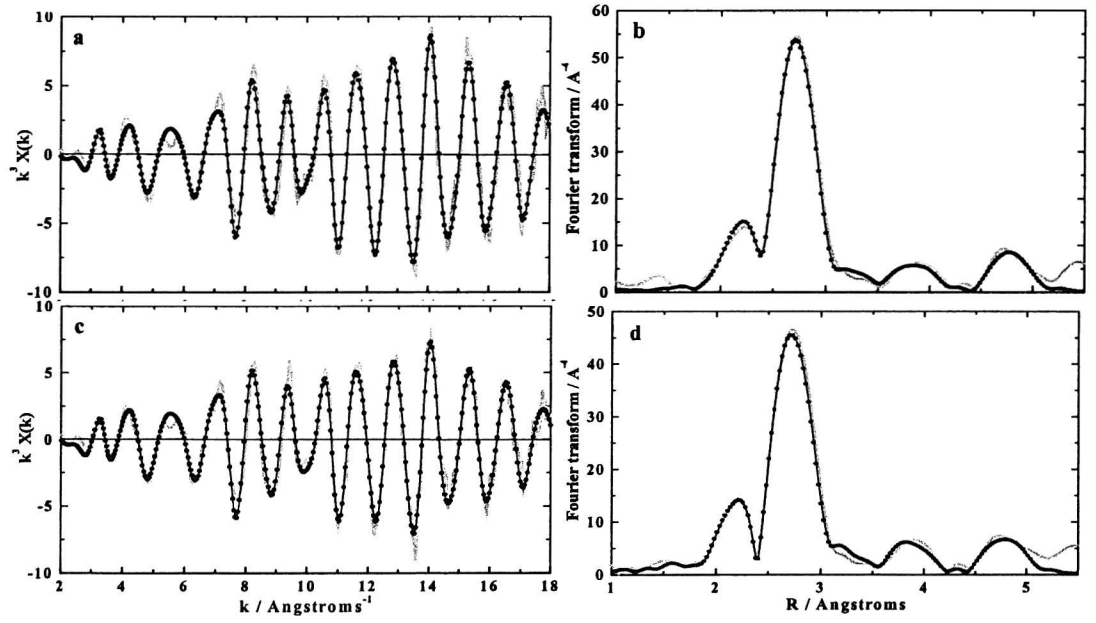

Figure 3 : (a) and (c) k^3-weighted experimental data for Pt-Ru/C (A) electrode in 1 mol dm^{-3} H_2SO_4 at – 0.6 V and 0.3 V, respectively (solid line) and fits (dotted line). (b) and (d) Pt phase corrected Fourier transforms of the data and fits of spectra in (a) and (c).

POTENTIAL / V VS. MMS	SHELLS		N	R / Å	$2\sigma^2$ / Å^2
- 0.6	**1**	**Pt-Pt**	**4.4 (0.3)**	**2.732 (0.002)**	**0.011 (0.001)**
R : 25%	2	Pt-Ru	3.2 (0.3)	2.710 (0.002)	0.013 (0.000)
E_f : - 12 eV	3	Pt-Pt	1.9 (1.0)	3.850 (0.014)	0.017 (0.004)
- 0.4	**1**	**Pt-Pt**	**4.5 (0.3)**	**2.732 (0.002)**	**0.011 (0.001)**
R : 25%	2	Pt-Ru	3.2 (0.3)	2.708 (0.002)	0.013 (0.000)
E_f : - 13 eV	3	Pt-Pt	1.9 (1.0)	3.846 (0.014)	0.017 (0.004)
- 0.1	**1**	**Pt-Pt**	**4.6 (0.4)**	**2.732 (0.002)**	**0.012 (0.001)**
R : 29%	2	Pt-Ru	3.2 (0.3)	2.710 (0.003)	0.013 (0.000)
E_f : - 11 eV	3	Pt-Pt	3.0 (2.0)	3.839 (0.020)	0.022 (0.008)
+ 0.3	**1**	**Pt-Pt**	**3.8 (0.3)**	**2.734 (0.002)**	**0.011 (0.001)**
R : 29%	2	Pt-Ru	2.8 (0.3)	2.717 (0.002)	0.012 (0.000)
E_f : - 12 eV	3	Pt-Pt	2.9 (1.7)	3.842 (0.013)	0.022 (0.007)
	4	Pt-O	0.5 (0.3)	2.019 (0.045)	0.029 (0.029)

Table 4 : Structural parameters for Pt-Ru/C (B) electrode as function of potential.

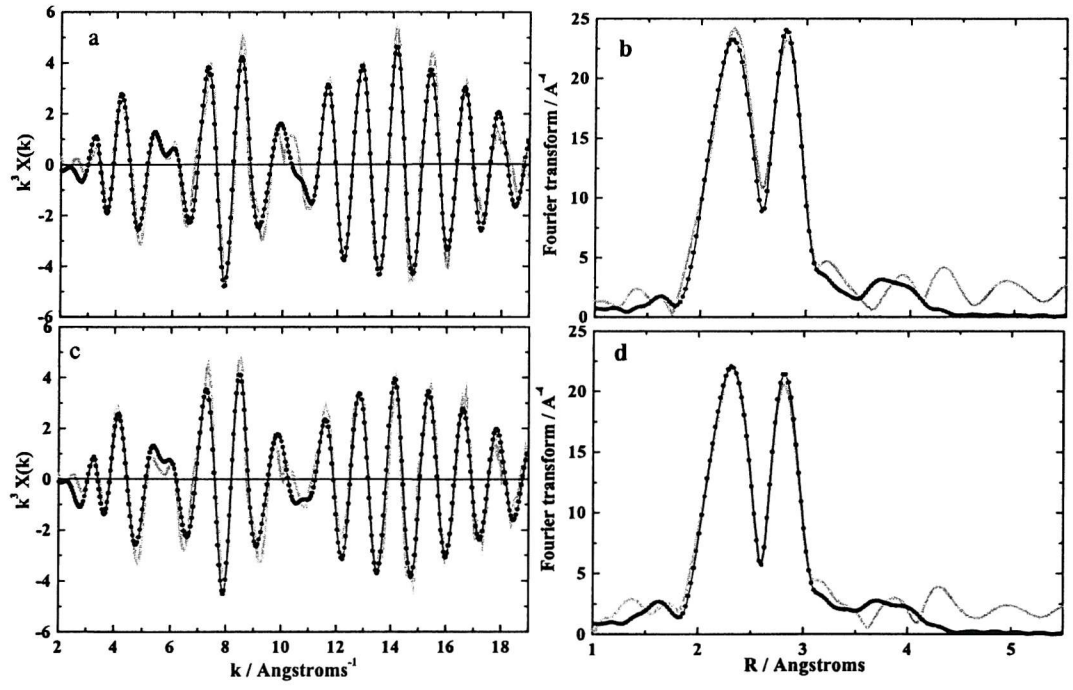

Figure 4 : (a) and (c) k^3-weighted experimental data for Pt-Ru/C (B) electrode in 1 mol dm^{-3} H_2SO_4 at – 0.6 V and 0.3 V, respectively (solid line) and fits (dotted line). (b) and (d) Pt phase corrected Fourier transforms of the data and fits of spectra in (a) and (c).

POTENTIAL / V VS. MMS	SHELLS		N	R / Å	$2\sigma^2$ / Å^2
- 0.6	**1**	**Pt-Pt**	**4.8 (0.5)**	**2.748 (0.006)**	**0.012 (0.001)**
R : 33%	2	Pt-Mo	1.8 (0.6)	2.739 (0.010)	0.012 (0.003)
Ef : - 14 eV	3	Pt-Pt	2.0 (0.8)	3.862 (0.018)	0.016 (0.005)
- 0.4	**1**	**Pt-Pt**	**5.2 (0.8)**	**2.743 (0.009)**	**0.013 (0.001)**
R : 38%	2	Pt-Mo	1.7 (0.9)	2.736 (0.015)	0.012 (0.006)
Ef : - 13 eV	3	Pt-Pt	2.2 (1.3)	3.851 (0.014)	0.015 (0.005)
- 0.1	**1**	**Pt-Pt**	**5.1 (0.7)**	**2.747 (0.014)**	**0.012 (0.001)**
R : 38%	2	Pt-Mo	1.8 (0.8)	2.741 (0.014)	0.012 (0.005)
Ef :- 13 eV	3	Pt-Pt	2.0 (1.2)	3.849 (0.012)	0.014 (0.004)
+ 0.3	**1**	**Pt-Pt**	**5.3 (0.7)**	**2.744 (0.009)**	**0.013 (0.001)**
R : 35 %	2	Pt-Mo	1.8 (0.8)	2.738 (0.014)	0.012 (0.005)
Ef : - 11 eV	3	Pt-Pt	2.4 (1.4)	3.853 (0.010)	0.018 (0.006)
	4	Pt-O	0.4 (0.5)	2.015 (0.084)	0.035 (0.050)
Ex situ	**1**	**Pt-Pt**	**4.4 (0.9)**	**2.752 (0.008)**	**0.012 (0.001)**
R : 35 %	2	Pt-Mo	2.0 (1.2)	2.753 (0.016)	0.014 (0.006)
Ef : - 14 eV	3	Pt-Pt	1.7 (1.6)	3.910 (0.020)	0.013 (0.006)
	4	Pt-O	0.6 (0.8)	2.030 (0.090)	0.024 (0.050)

Table 5 : Structural parameters for the Pt-Mo/C electrode as function of potential.

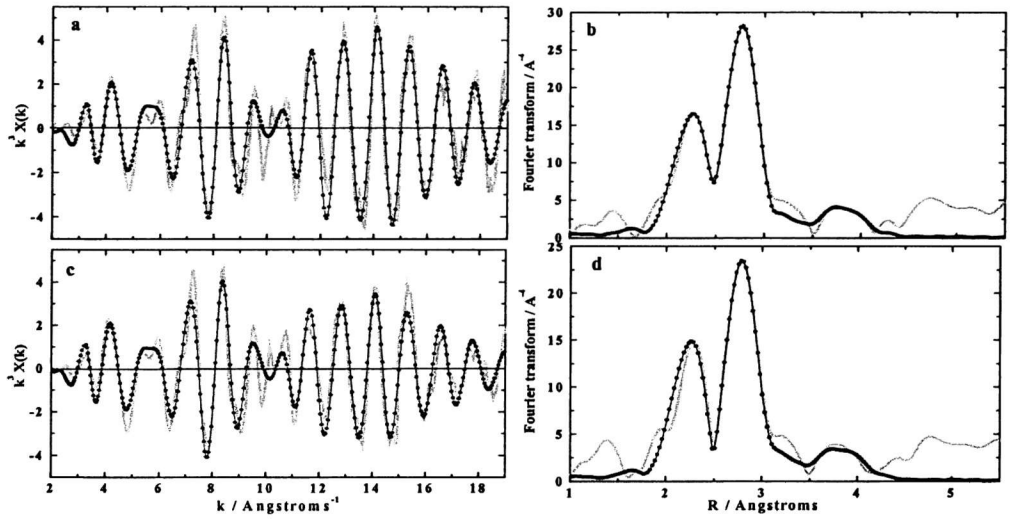

Figure 5 : (a) and (c) k^3-weighted experimental data for Pt-Mo/C electrode in 1 mol dm^{-3} H_2SO_4 at – 0.6 V and 0.3 V, respectively (solid line) and fits (dotted line). (b) and (d) k^3-weighted Fourier transforms of the data and fits of spectra in (a) and (c)

POTENTIAL / V VS. MMS	SHELLS		N	R / Å	$2\sigma^2$ / Å^2
- 0.6	**1**	**Pt-Pt**	**6.8 (0.6)**	**2.745 (0.005)**	**0.013 (0.001)**
R : 22 %	2	Pt-Mo	0.7 (0.6)	2.716 (0.019)	0.010 (0.008)
E_f: -12 eV	3	Pt-Pt	2.7 (1.3)	3.873 (0.012)	0.017 (0.004)
	4	Pt-Pt	4.3 (1.7)	4.772 (0.009)	0.015 (0.003)
- 0.4	**1**	**Pt-Pt**	**6.8 (0.7)**	**2.744 (0.006)**	**0.013 (0.001)**
R : 22 %	2	Pt-Mo	0.7 (0.7)	2.720 (0.022)	0.003 (0.001)
E_f: -12 eV	3	Pt-Pt	2.7 (1.3)	3.873 (0.013)	0.017 (0.004)
	4	Pt-Pt	5.2 (2.2)	4.763 (0.011)	0.018 (0.004)
- 0.1	**1**	**Pt-Pt**	**6.8 (0.6)**	**2.749 (0.005)**	**0.013 (0.001)**
R : 23 %	2	Pt-Mo	1.0 (0.8)	2.683 (0.003)	0.003 (0.001)
E_f: -13.5 eV	3	Pt-Pt	3.2 (1.6)	3.876 (0.014)	0.020 (0.005)
	4	Pt-Pt	4.3 (1.7)	4.772 (0.009)	0.015 (0.003)
+ 0.3	**1**	**Pt-Pt**	**6.1 (0.3)**	**2.751 (0.003)**	**0.014 (0.001)**
R : 32%	2	Pt-Mo	0.8 (1.0)	2.729 (0.007)	0.010 (0.001)
Ef : -13 eV	3	Pt-Pt	1.2 (0.2)	3.851 (0.009)	0.009 (0.001)
	4	Pt-Pt	3.3 (0.9)	4.776 (0.013)	0.014 (0.002)
	5	Pt-O	0.5 (0.1)	2.010 (0.015)	0.025 (0.017)
Ex situ	**1**	**Pt-Pt**	**5.6 (1.3)**	**2.747 (0.010)**	**0.014 (0.002)**
R : 31%	2	Pt-Mo	0.9 (1.0)	2.732 (0.041)	0.013 (0.002)
Ef : -12 eV	3	Pt-Pt	1.6 (1.2)	3.910 (0.021)	0.013 (0.007)
	4	Pt-Pt	2.1 (1.0)	4.779 (0.021)	0.012 (0.008)
	5	Pt-O	0.7 (0.4)	2.006 (0.042)	0.014 (0.016)

Table 6 : Structural parameters for the Pt-MoO_x/C electrode as function of potential.

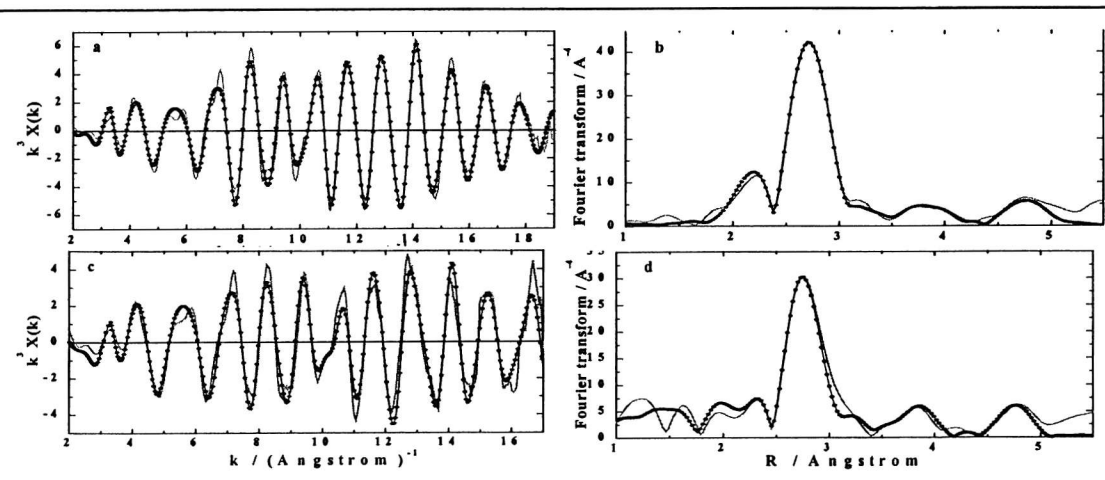

Figure 6 : (a) and (c) k^3-weighted experimental data for Pt-MoO_x/C electrode in 1 mol dm^{-3} H_2SO_4 at - 0.6 V and 0.3 V, respectively (solid line) and fits (dotted line). (b) and (d) k^3-weighted Fourier transforms of the data and fits of spectra in (a) and (c)

Figure 7 illustrates the evolution of the first shell coordination number (N_1) for the series of Pt-based electrodes as the potential increases. The value of N_1 for a Pt-M/C type catalyst is the sum of the contribution of the Pt and of the alloying element, M, within the first coordination sphere, i.e. N_1(Pt-Pt) + N_1(Pt-M). Independent of the nature of M, carbon supported bimetallic catalysts exhibit a smaller first shell coordination number than N_1 obtained for the Pt/C catalyst.

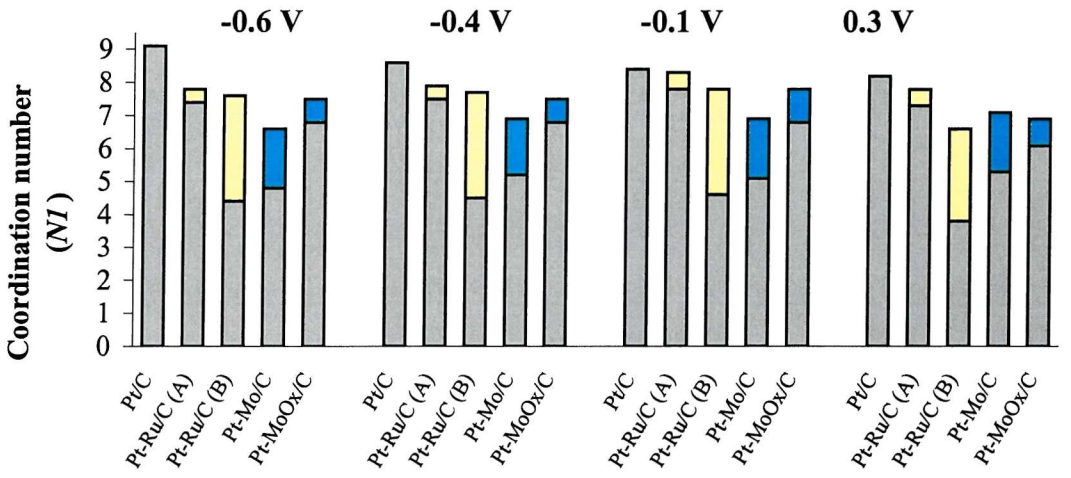

Figure 7 : Partition of the contribution of the Pt (gray) and the alloying element M, Ru (yellow) or Mo (blue) in the first coordination sphere as function of potential. All potentials vs. MMS.

In parallel, Figure 8 overviews the evolution of the Pt-Pt first shell coordination distance, R_1(Pt-Pt), as the potential increases for each electrodes. The greater the contribution of the alloying element is in the first coordination sphere, the smaller R_1(Pt-Pt) becomes. From this observation arises the following classification order : R_1(Pt/C) ≅ R_1(Pt-Ru/C(A)) > R_1(Pt-Mo/C) ≅ R_1(Pt-MoO_x/C) > R_1(Pt-Ru/C(B)), where the Pt-Pt inter-atomic distances vary between 2.73 Å and 2.75 Å (Table 2 to Table 5). Such structural changes due to the alloying element in the first coordination sphere were previously observed for the Pt-Ru/C electrodes at the potential of – 0.6 V (cf chapter 3).

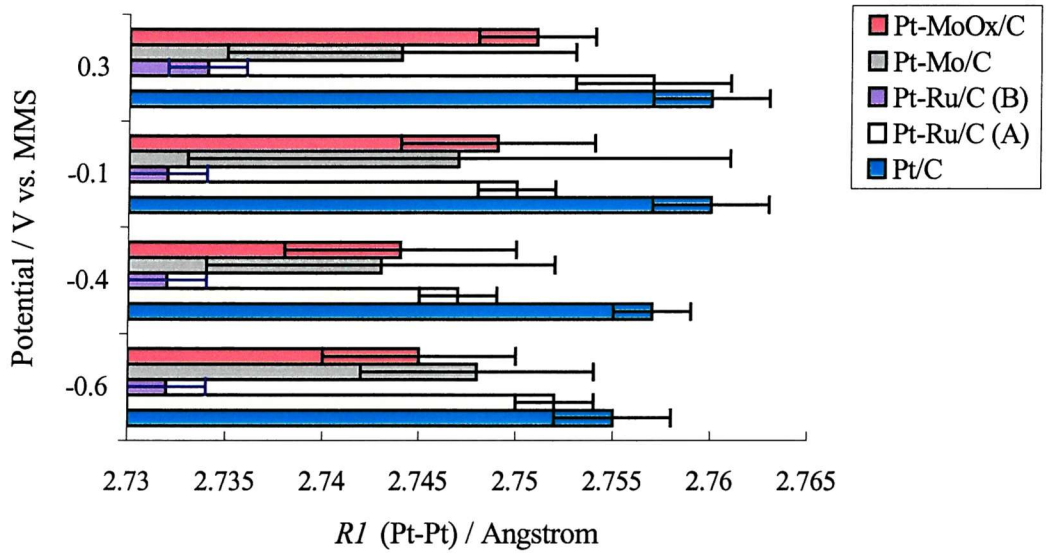

Figure 8 : Comparison of the interatomic distance R_1(Pt-Pt) for Pt-based electrodes as function of potential.

After having observed the alloying effect on the structure of the carbon supported nanosized particles, the following parts of this result section will detail the potential dependance for each of the electrode.

3.1.1 Pt/C electrocatalyst

The structural parameters for the Pt/C catalyst change when changing the applied electrode potential (Table 2). The most significant change is that the average first shell coordination number (N_1) decreases when the potential is swept towards more positive values, i.e. N_1(Pt-Pt)$_{-0.6\ V}$ = 9 and N_1(Pt-Pt)$_{+0.3\ V}$ = 8 (Figure 7). This agrees well with the decrease in the amplitude of the main peak of the FT (at 2.76 Å) observed in Figure 2 (compare panels (b) and (d)) as has been previously reported [9]. This phenomenom can be attributed to the exchange of Pt neighbours for O neighbours as the oxide is formed on the surface of the Pt particles at oxidative potentials. The best fit of the EXAFS data at 0.3 V has been obtained with a Pt-O coordination distance at 2 Å in addition to the Pt-Pt coordination distances. The large uncertainty of the fit parameters can be ascribed to the dominance of the

backscattering phase shift and amplitude of Pt neighbouring atoms over that of O neighbouring atoms. However, as mentioned before, the contribution of low Z neighbouring atoms, that scatter at low k values, can be emphasise by k^1-weighing the data. Figure 9 shows k^1-weighted experimental data (panels (a) and (c)) and FTs (panels (b) and (d)) at - 0.6 V and 0.3 V. The change of symetry and the decrease of the main peak indicate the presence of the contribution of O at 2 Å at 0.3 V (compare panels (b) and (d)).

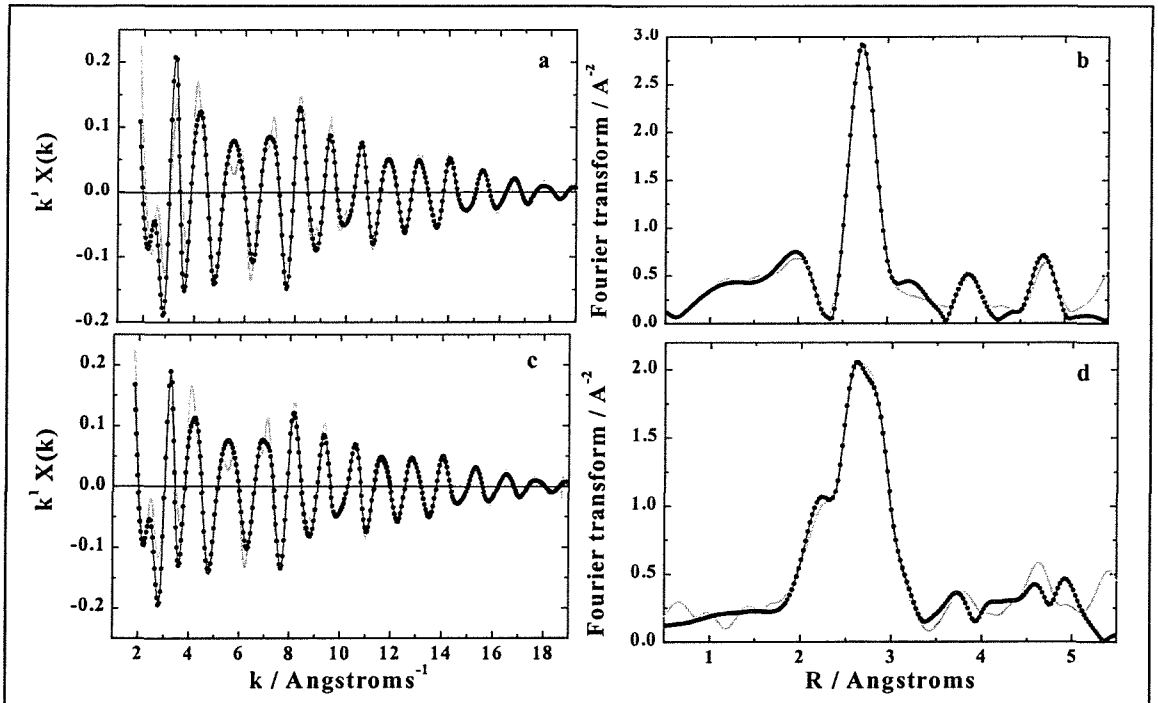

Figure 9 : (a) and (c) k^1-weighted experimental data for Pt/C electrode in 1 mol dm^{-3} H_2SO_4 at – 0.6 V and 0.3 V, respectively (solid line) and fits (dotted line). (b) and (d) Pt phase corrected Fourier transforms of the data and fits of spectra in (a) and (c).

As illustrated in Figure 8 the interatomic distances of the first (Pt-Pt) shell are slightly extended when changing the applied electrode potential, i.e. R_1(Pt-Pt) = 2.755 Å at – 0.6 V rises to 2.760 Å at 0.3 V vs. MMS. However, within the error of the fit, no significant potential dependance can be assumed. The shape and amplitude of the higher Pt-Pt

coordination distances, above 3.5 Å, together with the fit parameters remain similar when changing the electrode potential.

3.1.2 Pt-Ru/C electrocatalysts

Previous analysis of the EXAFS data recorded at – 0.6 V have shown very different structural parameters between the Pt-Ru/C (A) and (B) electrocatalysts (cf chapter 3). The Pt-Ru/C (B) sample was described as the more well mixed alloy with shortened interatomic distances R_1(Pt-Pt) and smaller coordination number N_1(Pt-Pt) in the first coordination shell compared to that of the sample (A).

When the applied electrode potential varies from the hydride region to the double layer region (e.g. – 0.6 to – 0.1 V), the coordination number (Figure 7) and the interatomic distance (Figure 8) of the first Pt-Pt shell remain similar for both Pt-Ru/C samples. This is also true for the Pt-Ru coordination number and the Pt-Ru interatomic distances (Figure 10).

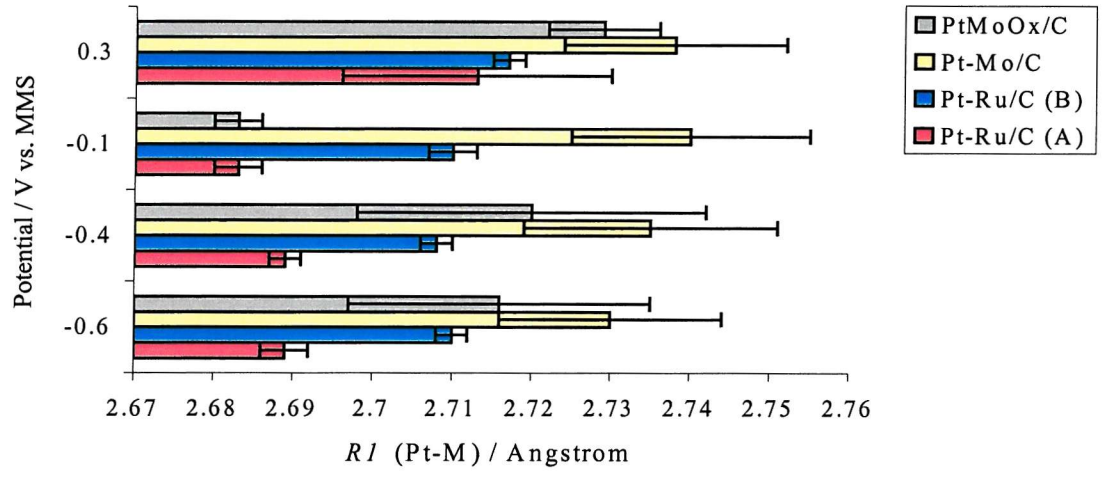

Figure 10 : Comparison of the first shell interatomic distance (Pt-M) as function of potential.

At the potential of oxide formation, N_1 decreases for both Pt-Ru/C electrodes. This corresponds to a decrease in both N_1(Pt-Pt) as indicated by the decrease in amplitude of the main peak of k^3-weighted Pt phase corrected Fourier transforms in Figure 3 and Figure 4

(compare panels (b) and (d)) and N_1(Pt-Ru). However, this is more pronounced for Pt-Ru/C (B), e.g. N_1 = 7.6 at – 0.6 V and N_1 = 6.6 at 0.3 V. Also, the best fits of the EXAFS data were achieved with one (Pt-O) coordination distance at 2.0 Å which is consistent with the Pt-O distance obtained for Pt/C electrode. Figure 11 and Figure 12 show the k^1-weighted EXAFS data and Pt phase corrected FTs for Pt-Ru/C (A) and (B), respectively. Although the backscattering amplitude decreases, the O scattering effect is attenuated compared to that of Pt/C at the oxidation potential. This is caused by the fact that Ru scatterers at low k values.

In addition, Figure 8 shows that the R_1(Pt-Pt) distance expands as the particles are oxidised as does the R(Pt-Ru) as shown in Figure 10. This is particurlay true for type (A) when R(Pt-Ru) increased from 2.68 Å to 2.71 Å. Therefore, the presence of the oxides affect the backscattering due to Ru as indicated by large error of the fit parameters of the Pt-Ru shell for type (A) as well as the larger disorder parameter.

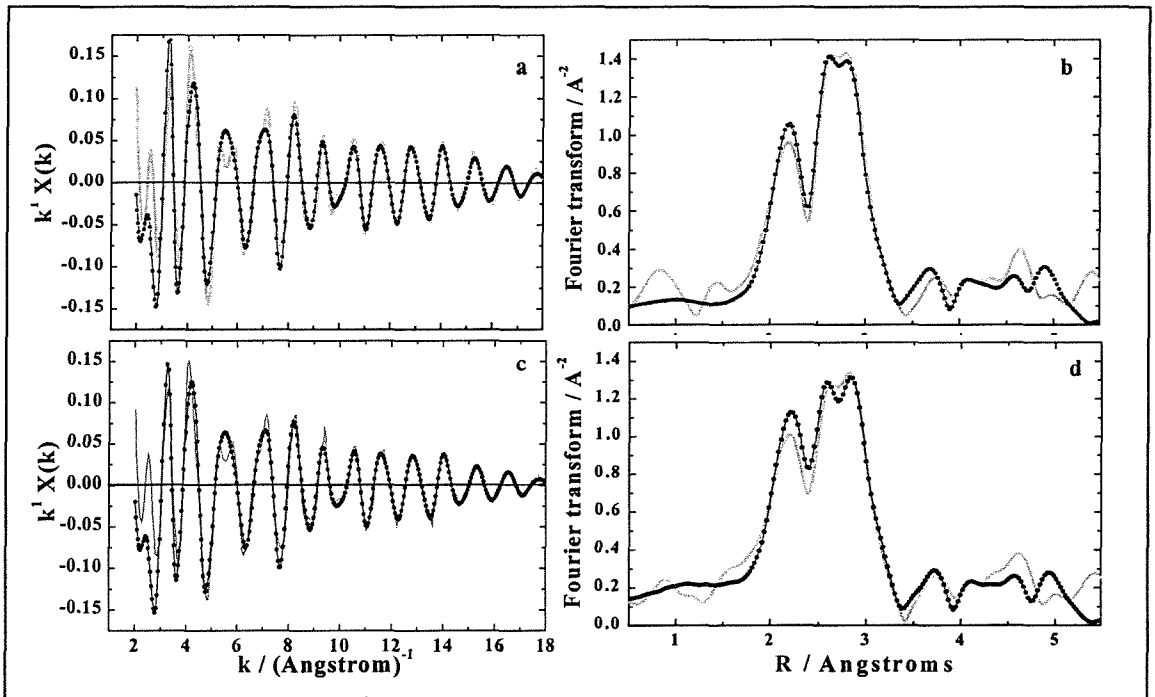

Figure 11 : (a) and (c) k^1-weighted experimental data for Pt-Ru/C (A) electrode in 1 mol dm^{-3} H_2SO_4 at – 0.6 V and 0.3 V, respectively (solid line) and fits (dotted line). (b) and (d) Pt phase corrected Fourier transforms of the data and fits of spectra in (a) and (c).

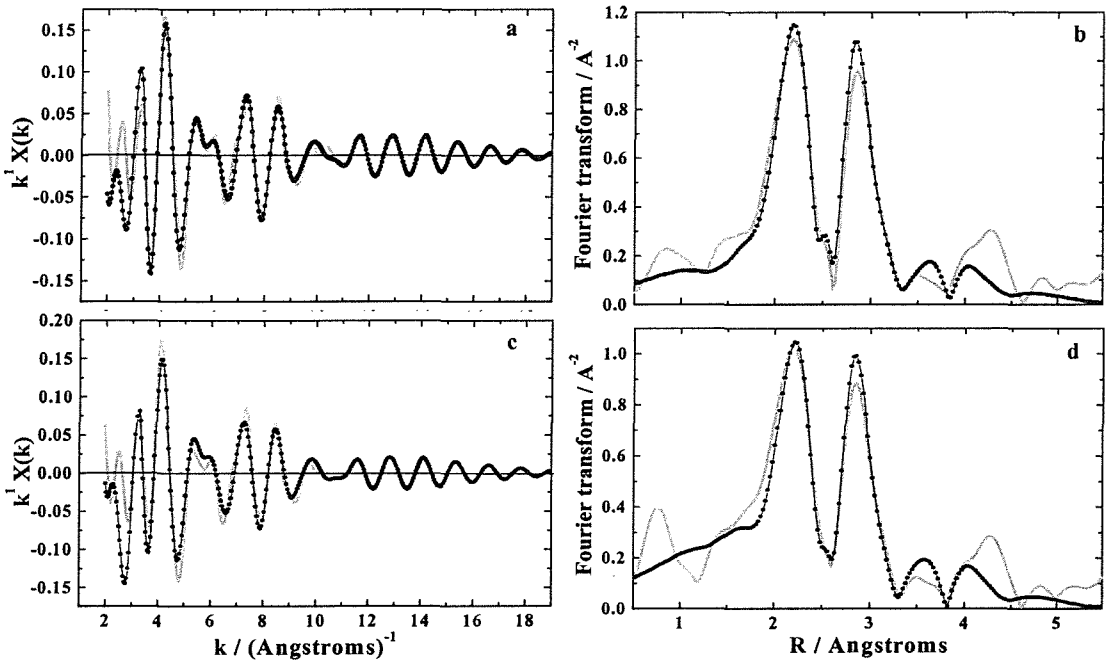

Figure 12 : (a) and (c) k^1-weighted experimental data for Pt-Ru/C (B) electrode in 1 mol dm^{-3} H_2SO_4 at – 0.6 V and 0.3 V, respectively (solid line) and fits (dotted line). (b) and (d) Pt phase corrected Fourier transforms of the data and fits of spectra in (a) and (c).

3.1.3 Pt-Mo/C electrocatalyst

The k^3-weighted EXAFS data of the Pt-Mo/C electrode recorded at the Pt L_{III} edge shows a phase cancellation at about 10 $Å^{-1}$ (Figure 13, panel (a)), when compared to the Pt/C electrode. Subsequently the Fourier transform exhibits a splitting of the main peak (Figure 13, panel (b)) as indicated by the presence of two peaks, i.e. 2.2 Å and 2.7 Å when compared to that of the Pt/C electrode. This latter phenomenom has been previously ascribed to the presence of the secondary element (in chapter 3), namely Mo, in the first coordination sphere and more specifically, to the beating in the phase between the two backscattering atoms (e.g. Pt and Mo) having similar Pt bond distances (e.g. 2.75 Å and 2.68 Å).

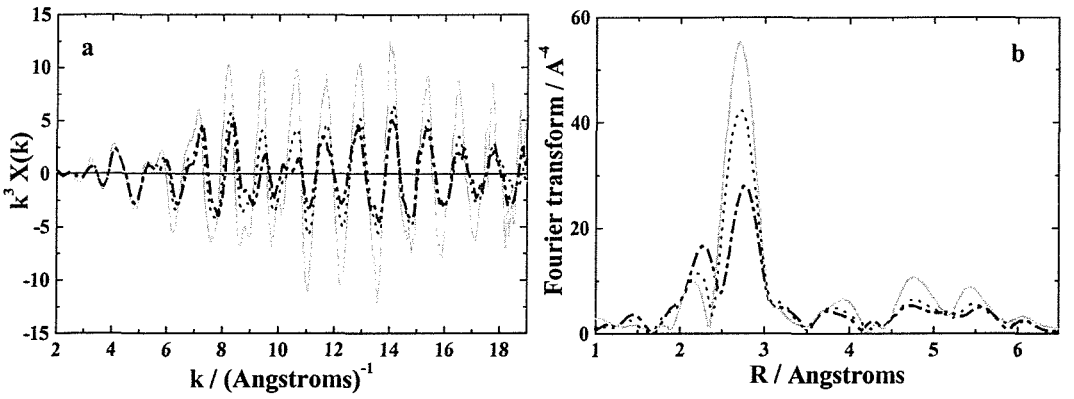

Figure 13 : (a) k^3-weighted experimental data recorded at the Pt L_{III} edge at RT in 1 mol dm^{-3} H_2SO_4 at – 0.6 V vs. MMS and (b) k^3-weighted Pt phase corrected Fourier transform for a Pt/C (solid line), Pt-Mo/C (dashed line) and $PtMoO_x$/C (dotted line) electrode. (the amplitude of the FT for Pt/C electrode has been divided by 1.5 to ensure comparison with Pt-Mo/C electrodes).

Further, the best fits of the EXAFS data were completed with a Pt-Mo contribution in addition to the Pt-Pt contribution in the first coordination shell (Table 5). Thus, the Pt central atom is surrounded by up to 2 Mo nearest neighbouring atoms at a distance of 2.74 Å and about 5 Pt nearest neighbouring atoms at a distance of 2.75 Å. In addition, the average coordination number of the Pt-Pt first shell is smaller compared to that obtained for Pt/C electrode, i.e. $N_1(\text{Pt-Pt})_{\text{Pt/C}} = 9.1$ against $N_1(\text{Pt-Pt})_{\text{Pt-Mo/C}} = 4.8$ at – 0.6 V. Also, the interatomic distance (Pt-Pt) is slightly shortened compared to that obtained for the Pt/C electrode, i.e. $R_1(\text{Pt-Pt})_{\text{Pt/C}} = 2.76$ Å against $R_1(\text{Pt-Pt})_{\text{Pt-Mo/C}} = 2.75$ Å at – 0.6 V. As a result, the Pt-Mo/C electrocatalyst consists of smaller platinum particles than those for the Pt/C electrocatalyst. Amongst the series of catalysts investigated the Pt-Mo/C provides the smallest first coordination shell as shown in Figure 7. The shape and the amplitude of the FT (Figure 13, panel (b)) for the higher Pt shells (e.g. $R > 4.2$ Å) is disrupted from the fcc structure model when compared to that of the Pt/C. Thereby, the interaction of the backscattering phase of the Pt and Mo atoms makes the fit of the longer distance shells difficult.

The complementary study that was realised at the Mo K edge presents a rich Pt environment around the Mo central atom. The best fit of the EXAFS data was completed with one Mo-Pt coordination distance and one Mo-O coordination distance, as seen in Table 7 below.

Moreover, the k^2-weighted phase uncorrected FT for the Pt-Mo/C electrode differs drastically from that of the Mo foil at Mo K edge, as illustrated in Figure 14. Thereby, the crystallite structure of the Pt-Mo/C does not correspond to the body centered cubic (bcc) structure of the Mo bulk.

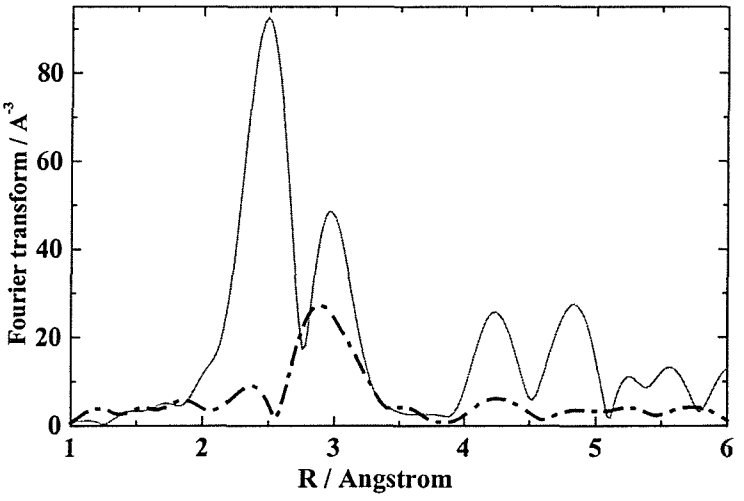

Figure 14 : k^2-weighted phase uncorrected Fourier transform at the Mo K edge for the Mo foil (----) and for the Pt-Mo/C (- . - . -) electrode at – 0.6 V.

POTENTIAL / V VS. MMS	SHELLS		N	R / Å	$2\sigma^2$ / Å^2
- 0.6	1	Mo-Pt	4.3 (0.3)	2.732 (0.007)	0.013 (0.001)
R : 44 %, E_f : - 5 eV	2	Mo-O	0.6 (0.2)	1.947 (0.022)	0.011 (0.007)
- 0.1	1	Mo-Pt	3.9 (0.5)	2.749 (0.006)	0.012 (0.002)
R : 44 %, E_f : -10 eV	2	Mo-O	0.8 (0.4)	1.867 (0.033)	0.012 (0.021)
Open circuit	1	Mo-Pt	4.0 (0.4)	2.740 (0.009)	0.013 (0.001)
R : 55 %, E_f : - 6 eV	2	Mo-O	0.7 (0.1)	1.715 (0.016)	0.003 (0.003)
	3	Mo-O	0.4 (0.2)	1.964 (0.028)	0.002 (0.005)

Table 7 : Fit parameters for the Pt-Mo/C catalyst as function of potential at Mo K edge.

These contributions consist of about 4.8 Pt neighbouring atoms at 2.73 Å and 0.5 O neighbouring atoms at 1.95 Å at the reduction potential. Both Pt-Mo and Mo-Pt coordination distances from the fits at the two edges agree with one another. An additionnal shorter Mo-O coordination distance, i.e. 1.72 Å has been obtained for the data recorded at the open circuit potential. Figure 15 shows clearly the predominance of this short oxygen distance in the k^2-weighted experimental data and the corresponding FT, in panels (e) and (f), respectively. Also, changes occur at - 0.1 V, where the Mo-Pt coordination distance expands and the Mo-O coordination distance shrinks (Table 7).

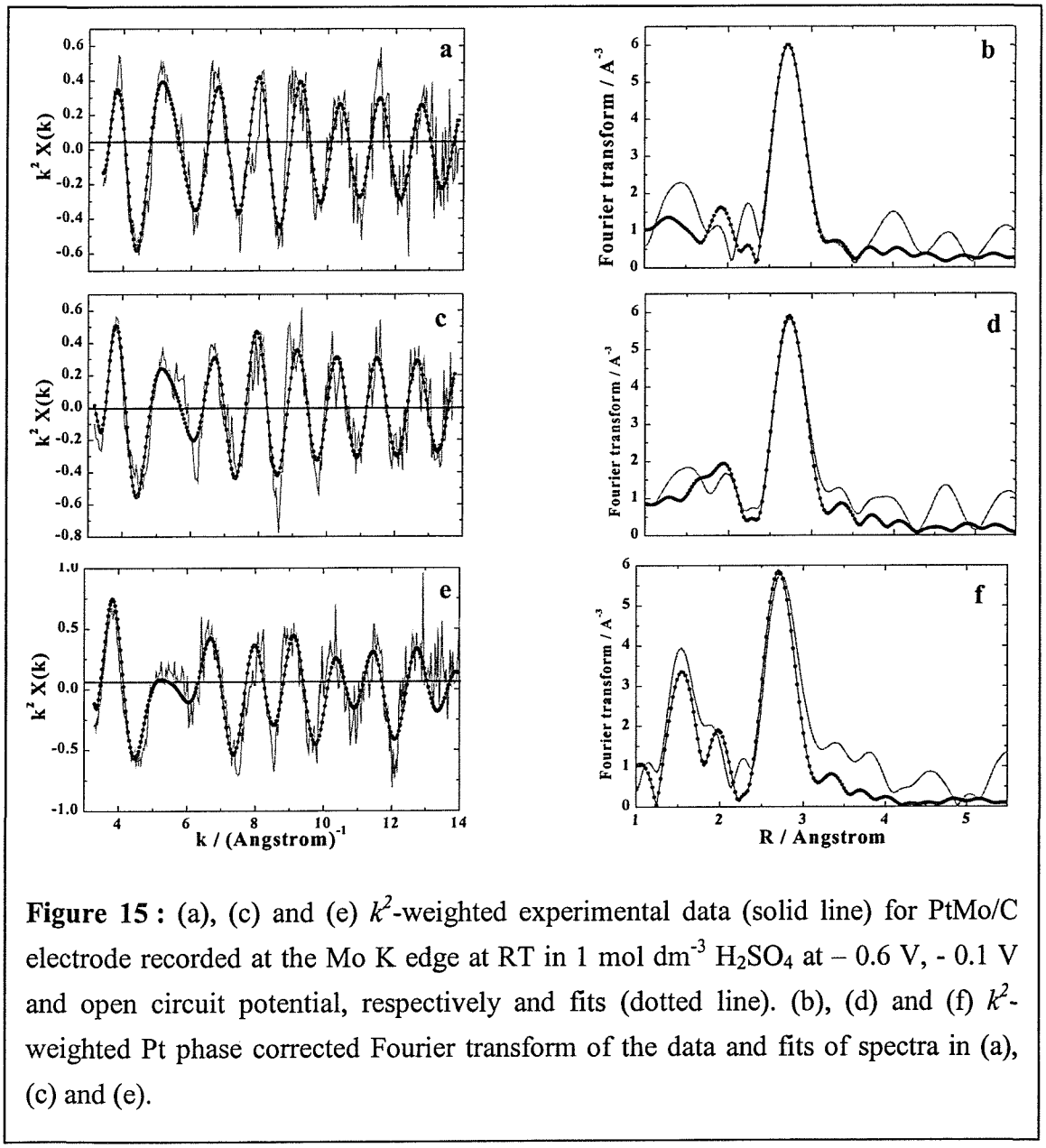

Figure 15 : (a), (c) and (e) k^2-weighted experimental data (solid line) for PtMo/C electrode recorded at the Mo K edge at RT in 1 mol dm^{-3} H_2SO_4 at – 0.6 V, - 0.1 V and open circuit potential, respectively and fits (dotted line). (b), (d) and (f) k^2-weighted Pt phase corrected Fourier transform of the data and fits of spectra in (a), (c) and (e).

Figure 5 shows k^3-weighted experimental data at the Pt L_{III} edge for PtMo/C electrode at -0.6 V and 0.3 V, in panels (a) and (c), respectively, and Pt phase corrected Fourier transform of the data and fits of the spectra in (a) and (c), in panels (b) and (d), respectively. The backscattering amplitude due to Pt neighbouring atoms between 10 $Å^{-1}$ and 19 $Å^{-1}$ is clearly reduced at the potential of oxidation (compare (a) and (c)), so does the amplitude of the main peak of the FT (compare (b) and (d)). This phenomenon is in agreement with a decrease of the first shell Pt-Pt coordination number as previously described for the Pt-based electrodes. However, the best fits of the EXAFS data were obtained with no change in the corresponding N_1 values (Table 5), i.e. N_1(Pt-Pt) = 5 and N_1(Pt-Mo) = 1.8.

3.1.4 Pt-MoOx/C electrocatalyst

The best fit of the EXAFS data recorded at the Pt L_{III} edge were achieved with three Pt-Pt coordination distances and a Pt-Mo distance (Table 6). Compared to the former higher Mo loading electrode, similar first shell Pt-Pt coordination distances (i.e. 2.75 Å) and larger first shell Pt-Pt coordination number have been observed. Also, N_1(Pt-Pt) decreases as the potential reaches 0.3 V. This is consistent with the decrease in the amplitude of the EXAFS data and the amplitude of the main peak of the FT, as shown in Figure 6, in panels (c) and (d), respectively. Therefore, Pt-MoO_x/C is sensitive to the oxide formation. Also, it should be noticed that the Pt-Mo coordination distance has been shortened at –0.1 V. Unfortunately it is not possible to compare this distance with that obtained at the Mo K edge, as the data are not available at –0.1 V. Also, the best fit of the EXAFS data recorded at the Mo K edge was obtained with one Mo-Pt and one Mo-O shell at – 0.6 V (Table 8).

POTENTIAL / V VS. MMS	SHELLS		N	R / Å	$2\sigma^2$ / $Å^2$
- 0.6	1	Mo-Pt	5.2 (0.4)	2.728 (0.006)	0.013 (0.001)
R : 51 %, E_f : - 11 eV	2	Mo-O	0.7 (0.2)	1.939 (0.024)	0.010 (0.006)
Ex-situ	1	Mo-Pt	2.9 (0.4)	2.747 (0.010)	0.012 (0.001)
R : 50 %, E_f : - 11 eV	2	Mo-O	1.1 (0.1)	1.737 (0.012)	0.005 (0.002)
	3	Mo-O	0.6 (0.2)	1.966 (0.024)	0.002 (0.004)

Table 8 : Fit parameters for the Pt-MoOx/C catalyst as function of potential at Mo K edge.

Both Pt-Mo and Mo-Pt coordination distances from the fits at the two edges agree with one another. The predominance of the Mo-O short coordination distance for the *ex-situ* data can be clearly seen in Figure 16. The predominance of the O is clearly seen at low k and low R values in panels (c) and (d), respectively. Whereas the decrease in the amplitude corresponds well with the decrease of the Mo–Pt coordination number.

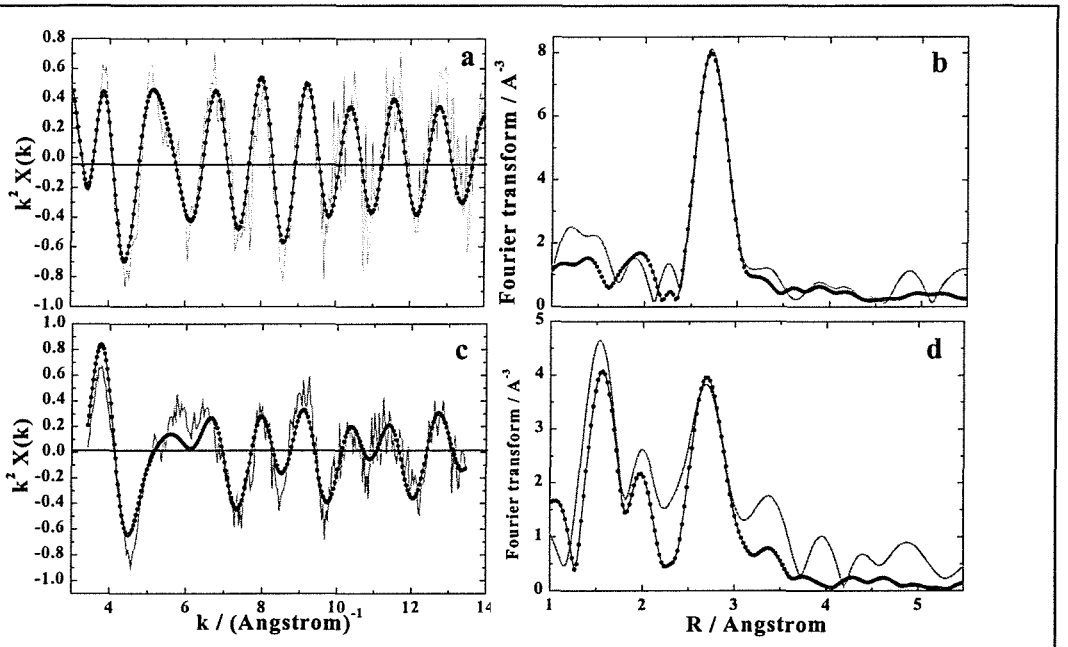

Figure 16 : (a) and (c) k^2-weighted experimental data (solid line) for PtMoOx/C electrode recorded at the Mo K edge at RT in 1 mol dm^{-3} H_2SO_4 at – 0.6 V and ex-situ, respectively and fits (dotted line). (b) and (d) k^2-weighted Pt phase corrected Fourier transform of the data and fits of spectra in (a) and (c).

Figure 17 shows the Mo K edge XANES spectra for the Pt-Mo/C and Pt-MoO_x/C electrode as a function of potential in panels (a) and (b), respectively. The edge position is shifted positive to the Mo foil, indicating that Mo is oxidised. This is particurlarly true for the Pt-MoO_x/C electrode. Furthermore, the comparison of the XANES at – 0.6 V and 0.3 V reflects a change in the change in the edge threshold feature, i.e a shoulder is visible at half the height of the edge. This indicates a change in the Mo valence. An *in situ* XANES investigation of the reduction and oxidation of MoO_{3-x} has reported that the spectra may be modelled by the linear combinaison of two Mo phases, MoO_2 and MoO_3 [10]. This enables

the characterisation of the Mo close to an oxidation state of (+IV) at – 0.6 V and close to (+VI) at 0.3 V for the Pt-MoO_x/ catalyst. However, very little variation is observed for the PtMo/C catalyst, compare panels (a) and (b)

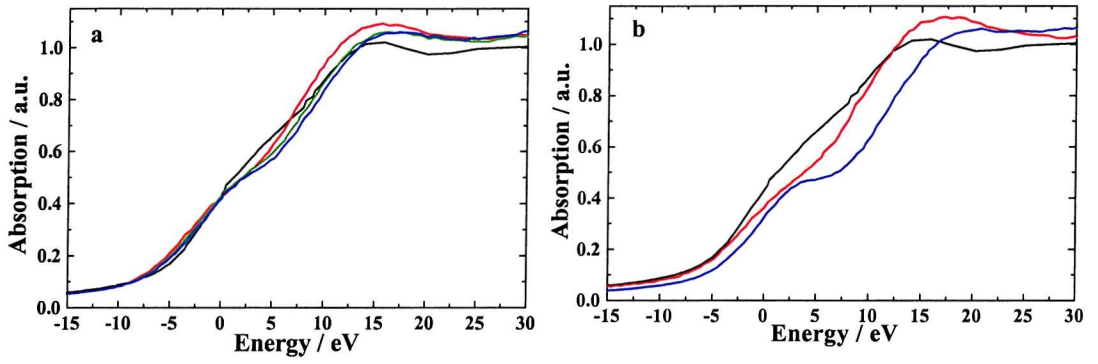

Figure 17 : XANES spectra of the Pt-Mo/C and Pt-MoO_x/C in panels (a) and (b), respectively. Black line is Mo foil, red line is – 0.6 V, blue line is 0.3 V and and green line is – 0.1 V. All potentials vs. MMS.

The improved CO tolerance of PtMo/C electrocatalysts as compared to Pt/C has been attributed to the redox behaviour of the Mo(IV/VI) couple [11]. The XANES region of the XAS spectrum provides direct *in situ* evidence of this redox couple.

3.2 The electronic property

Transition metals are known as good catalysts because of their ability to adsorb hydrogen and oxygen as well as molecules or hydrocarbons fragments. Their characteristic partly filled d-shell provides an attractive electronic property. Electron-band theory invokes the overlap of d levels electron with the immediately higher s level [12]. The electronic property remains a major parameter in understanding the catalytic activity of the amorphous materials used as fuel cell catalysts.

3.2.1 Determination of the d-band vacancy

When X-rays were firstly detected photographically, an over-exposed 'white line' appeared on the film negative [13]. Therefore, the sharp resonance feature observed near the edge in the XAS spectrum was named the white line and has been attributed to the high density of final states. Since the dipole selection rules in the XANES region restrict transitions to $\Delta L = \pm 1$ and $\Delta J = 0, \pm 1$ (L and J are the orbital angular and total angular momentum quantum numbers, respectively), the transitions to the d-orbitals are the most strongly favored. Therefore, the electronic transition occuring at the Pt L_{II} and the L_{III} edges excites the $2p_{3/2}$ and $2p_{1/2}$ core states, respectively, to vacant d states. Also, it has been demonstrated that for Pt the final states with J =5/2 contribute 14 times more than those with J =3/2 [14]. Qualitatively, the predominance of the $d_{5/2}$ character is observed as the intensity of the white line at the Pt L_{III} is more intense compared to that at the Pt L_{II} edge (Figure 18). Further, Mansour et al have proposed a quantitative method to evaluate the d-band vacancy using the L_{II} and L_{III} edge XAS spectrum [15]. This was done by comparing the fractional change of the d-band occupancy (f_d) of the sample from that of a reference, namely bulk platinum.

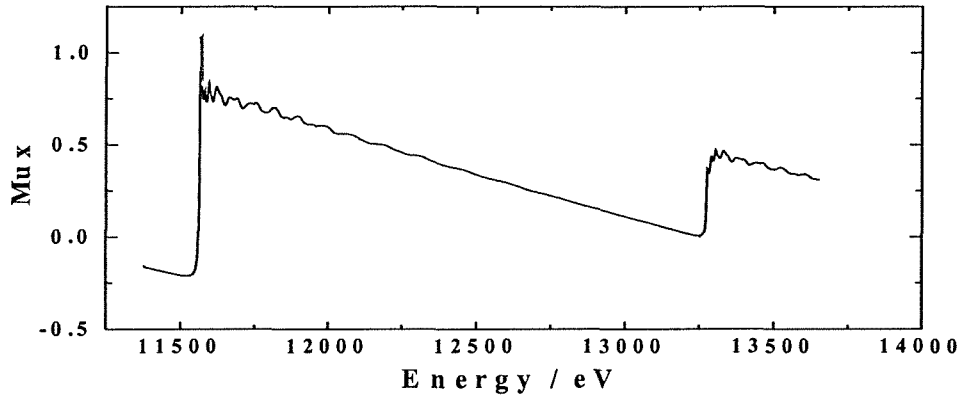

Figure 18 : Transmission XAS spectrum at the Pt L_{III} and the L_{II} edges for the Pt foil.

The total density of the unoccupied d-state (h_T) is compared to that of the reference (h_r) by :

$$h_T = (1.0 + f_d)\, h_r \qquad \text{Equation 1}$$

The calculation of the fractional change is based on Equation 2.

$$f_d = \frac{(\Delta A_3 + 1.11\Delta A_2)}{(A_{3reference} + 1.11A_{2reference})} \quad \text{with} \quad \Delta A_3 = A_{3sample} - A_{3reference} \quad \Delta A_2 = A_{2sample} - A_{2reference} \qquad \text{Equation 2}$$

Where A_i is the intensity of the white line of the L_i edges, where i = 2 or 3. Thus, a larger f_d value corresponds to smaller d-state occupancy.

The intensity of each white line can be regarded as the difference between the atomic background and the XANES. The atomic background may be described by an arc tangent function that cuts off the spectral area from the inflection point to the second (or first) local minimum in the appropriate normalized XANES spectrum at Pt L_{III} (or Pt L_{II}) edge. This was done by adjusting the minimum, maximum, steepness and energy of the arc tangent function to match the experimental data. Examples are given in Figure 19 for Pt L_{III} and Pt L_{II}. Then, the integration of the area A_i in the energy range of –10 eV to 40 eV enables the calculation of f_d according to Equation 2.

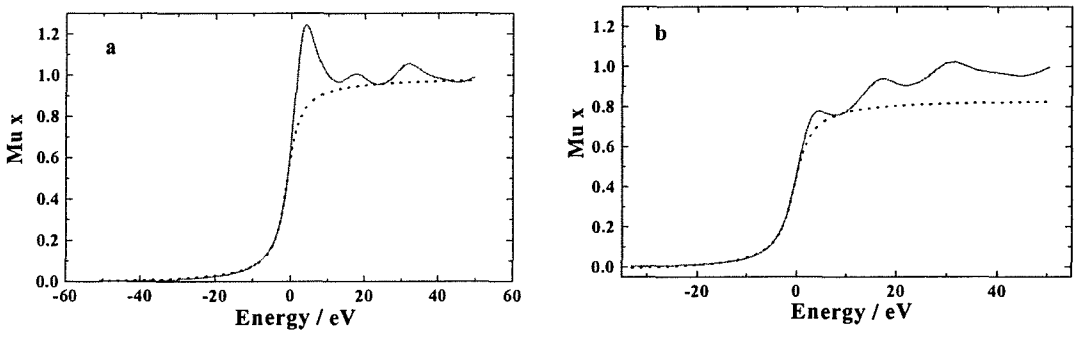

Figure 19 : Normalised XAS spectrum (solid line) at the Pt L_{III} edge (a) and the Pt L_{II} edge (b) ; Arc tangent determining the white line area (dotted line).

The evaluation of the electronic density for the catalysts presently investigated was considered with f_d only, as h_T is proportional to f_d. The reference used was a 4 μm thick Pt foil.

3.2.2 Results

3.2.2.1 d-band occupancy

The electronic density was evaluated for the series of the Pt-based carbon supported catalysts listed in Table 1. To remove the impact of the oxide on the Pt d-band occupancy the white line analysis was completed with the EXAFS spectra recorded at most reducing potential, i.e. – 0.6 V vs. MMS. Thus, the fractional change (f_d) in the d-band vacancy is given in Table 9. The Pt-Ru/C (B) and Pt-Mo/C provide the most significant change in the Pt electronic density, whereas the Pt/C and the Pt-Ru/C (A) have similar d-band occupancy within an error evaluated to be 10 % of the value of the fractional change.

Catalysts	**f_d**
40 wt. % Pt/C	-0.03
40 wt. % Pt, 20wt. % Ru/C (A)	0.03
40 wt. % Pt, 20wt. % Ru/C (B)	-0.35
40 wt. % Pt, 20wt. % Mo/C	-0.34
40 wt. % Pt, 5 wt. % Mo/C	-0.26

Table 9 : Fractional change (f_d) in the d-band occupancy at – 0.6 V vs. MMS for the series of Pt-based carbon supported catalysts. $\Delta f_d = \pm$ 10%.

3.2.2.2 XANES

Figure 20 compares the XANES plots or the normalised XAS spectra as function of potential with that of the bulk Pt for each sample.

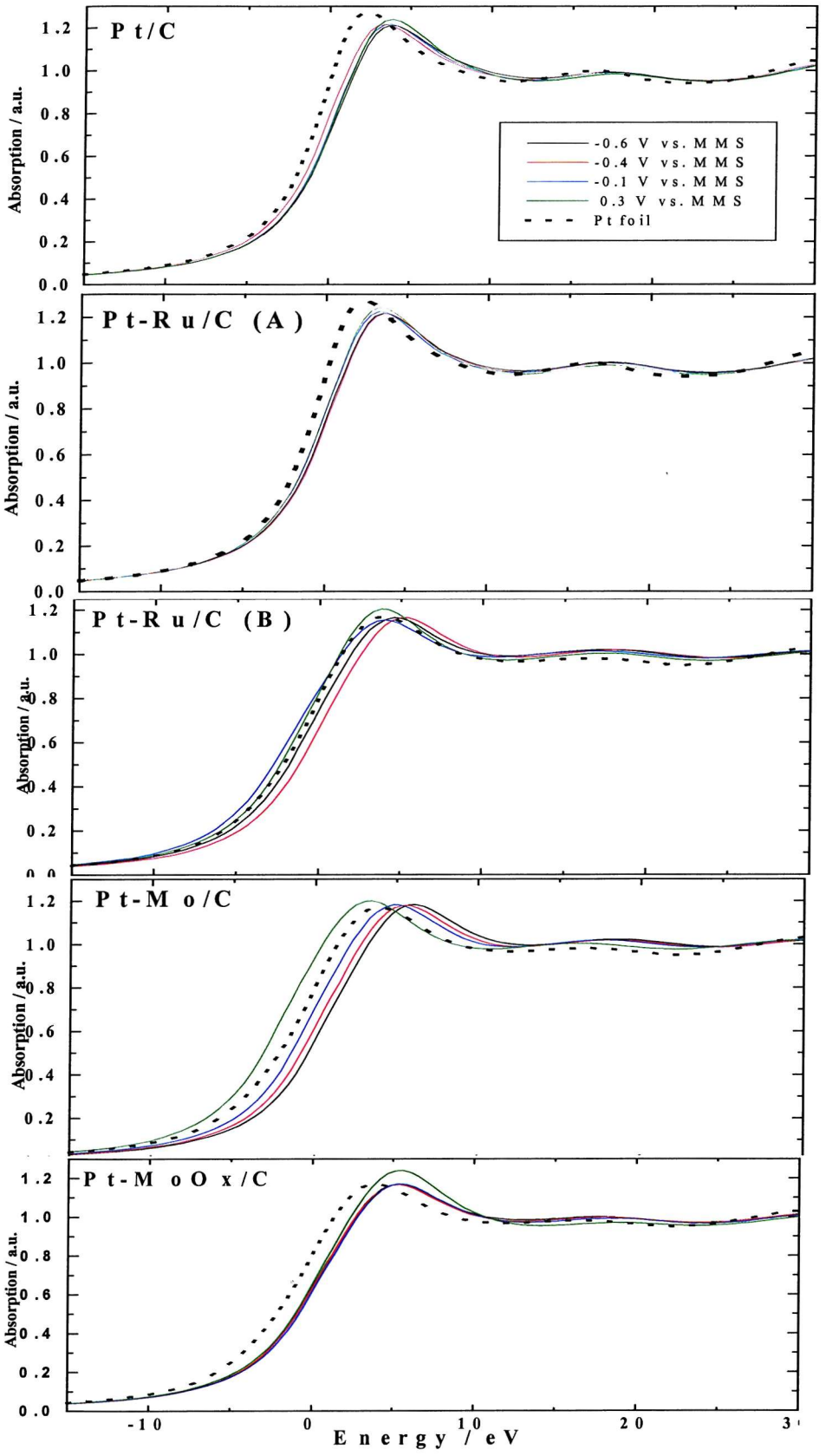

Figure 20 : Comparison of the XANES plots for the series of Pt-based carbon supported catalysts as function of potential.

The edge resonance of the Pt-based carbon supported catalysts corresponds to that of the bulk Pt indicating the metallic property of the nanoparticles. The XANES spectra of the Pt/C and the Pt-Ru/C (A) reflect only a very small change (e.g. energy shift or widening of the edge) when changing the applied electrode potential. This is reflected in the small variation of the parameter f_d as function of potential shown in Figure 21.

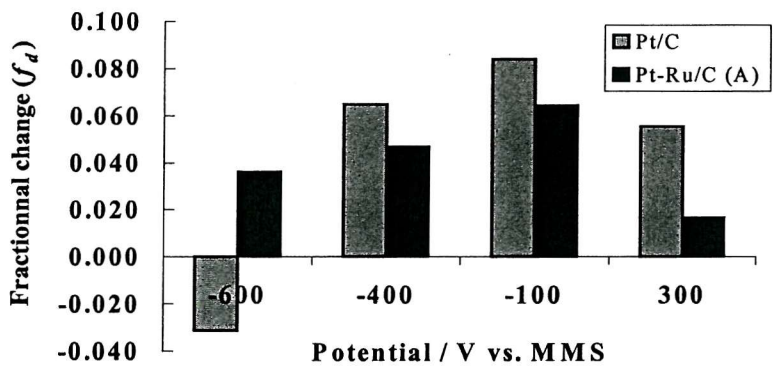

Figure 21 : Frationnal change in the d-band vacancy for the Pt/C and the Pt-Ru/C (A) as function of potential.

Considering that the error in the f_d value is at least 10 %, the d-band occupancy of the Pt/C and the Pt-Ru/C(A) (bad alloy) catalyst can be regarded as equivalent. Furthermore, a decrease of the d-band occupancy is observed when the potential is increased towards an oxidised state. This result is in agreement with those reported by other groups [9,16].

In contrast, the normalised XAS spectra of the Pt-Ru/C (B) and Pt-Mo/C catalysts show significant changes in the near edge region (an energy shift, a greater intensity and the broadening of the resonnance peak), particularly when the potential reaches the oxidation potential. Such changes are consistent with the large d-band vacancy or greater f_d obtained for these two catalysts. Although the Pt-MoO_x/C electrocatalyst provides a large d-band vacancy compared to that of the Pt/C electrode, the XANES remain stable as the potential increases and increases greatly at the oxidation potential. This is consistent with the

sensitivity of this catalyst towards the oxide formation that was previously observed through the change in the fit parameters.

4 DISCUSSION

The EXAFS and XANES results presented above have shown clear differences between the Pt/C and the Pt-M/C (where M = Ru or Mo) electrocatalysts. The presence of the secondary element M in the nanosized platinum particles induces changes in the features of the Chi(k) and the FTs compared to that of the Pt/C (i.e. phase cancellation and the splitting of the main peak, respectively). Thereby, structural changes are expected. Indeed, the bimetallic carbon supported particles provide smaller first shell coordination numbers (N_1) and shortened Pt-Pt first shell coordination distances, as illustrated in Figure 7 and Figure 8, respectively. This behaviour is evident over the entire potential range investigated. The Pt-M/C particles are smaller which is in good agreement with the crystallite size obtained using *ex situ* XRD (Table 1). The Pt-Ru/C (B) and the Pt-Mo/C catalyst exhibit a smaller crystallite size of 2.4 nm compared to that of the Pt/C, i.e. 4.0 nm. Also, the shortened interatomic distances (R_1(Pt-Pt)) are in good agreement with the contraction of the lattice parameter compared to that of the Pt/C (a = 3.92 Å). This is particularly true for the Pt-Ru/C(B) (a = 3.86 Å) whereas only a slight contraction for the Pt-Ru/C(A) (a = 3.90 Å) and no contraction for the Pt-Mo/C and Pt-MoO_x/C were obtained. This is somewhat surprising, as the crystallite size of PtMo/C is comparable to PtRu/C (B).

The presence of a second Pt-Pt coordination distance at about 3.9 Å in the EXAFS data indicates the presence of a 3 dimensional metal cluster for each of the samples. Since the second shell distance in an fcc structure is defined as the lattice parameter itself [17] a correlation between *ex situ* XRD and *in situ* EXAFS data is given in Table 10 overleaf. The second Pt-Pt coordination distance, R_2(Pt-Pt) and the lattice parameter are in good agreement one with another, except for the Pt-Mo/C and the Pt-MoO_x/C electrodes.

	EXAFS parameters		XRD parameters	
Catalysts	**N1 (Pt-Pt) + N1 (Pt-M)**	**R2 (Pt-Pt)**	**Crystallite size /nm**	**Lattice parameter / Å**
Pt/C	9.1	3.91	4.0	3.92
Pt-Ru/C (A)	7.8	3.89	3.2	3.90
Pt-Ru/C (B)	7.6	3.85	2.4	3.86
Pt-Mo/C	6.6	3.86	2.4	3.92
Pt-MoO_x/C	7.5	3.87	2.9	3.91

Table 10 : Comparison of the EXAFS data at – 0.6 V vs. MMS and the XRD parameters.

The fit parameters for Pt-Mo/C and Pt-MoO_x/C catalysts extracted from the *ex situ* EXAFS data (Table 5 and 6) indicate a R_2(Pt-Pt) distance which is similar to the lattice parameter obtained with the XRD technique, i.e. 3.92 Å and 3.91 Å, respectively. Thus, the shorter distance may be a result of the electrochemical reduction.

Since the first shell coordination number reflects the size of the particles, the formulae derived by Benfield *et al.* may be used to correlate N_1 to the total number atoms in the particle [18]. The stability of the Pt clusters depends on their cubooctahedral and icosahedral geometrical shape [19]. If the Pt cluster adopts a cubooctahedral shape a N_1 value of 9.63 corresponds to a metal cluster of 309 atoms, a N_1 of 8.98 to 147 atom cluster and a N_1 of 7.85 to a 55 atom cluster. In addition, if the Pt cluster adopts a icosahedral shape a N_1 of 9.47 corresponds to a metal cluster of 147 atoms, a N_1 of 8.51 to 55 atom cluster and a N_1 of 6.46 to a 13 atom cluster. The number of surface atoms for each of these clusters is 162, 92, 42 and 12 (starting from the larger cluster size) and, thus, a dispersion of 0.53 to 0.92 is possible.

Amongst the Pt-M type catalysts, the Pt-Mo/C catalyst exhibits the smallest N_1 value as illustrated in Figure 7. For instance, the N_1 value decreases by 14%, 16%, 18% and 27% for the Pt-Ru/C (A), the Pt-Ru/C (B), the Pt-MoO_x/C and Pt-Mo/C, respectively over the N_1 of

the Pt/C electrode at – 0.6 V. However, the N_1(Pt-Pt) and the total first shell coordination number for Pt-Mo/C are not sensitive to the potential change and in particular as the electrode is oxidised. In contrast, N_1(Pt-Pt) and the total first shell coordination number decrease for the Pt-Ru/C and the Pt-MoO_x/C electrodes, as does, to a larger extent, N_1 for the Pt/C electrode. In addition, the first shell Pt-Pt coordination distance expands as the particles are oxidised for Pt/C. This result is consistent with other *in situ* EXAFS investigations [20]. To a lesser extent, this latter phenomenon was observed for the PtRu/C(A), which was defined as a poorly mixed alloy.

The presence of a Pt-O coordination distance at 2 Å has also provide evidence of the formation of an oxide layer on the Pt surface at 0.3 V. The oxide adsorption is not restricted to the surface as indicated by the decreased Pt-Pt coordination number. From the low Pt-O contribution for PtRu/C(A) compared to that of the PtRu/C(B) it is clear that the Ru atoms occupy some of the surface sites. Thereby, the number of sites are less available for the oxide adsorption onto Pt. It should be said that the investigation of the oxide formation on small platinum particles using EXAFS technique can be done more precisely with the difference file technique. This consists of substracting the contributions from the heavier scatterers contributions from the experimental data to enable the fitting of the of the lighter scatterers. This will be presented for the Pt/C electrode in the following chapter.

EXAFS data and fit parameters for PtMo/C at the Pt L_{III} edge have evidenced the presence of Mo within the first shell coordination sphere, as indicated by the Pt-Mo coordination distance. Furthermore, *in situ* fluorescence studies at the Mo K edge have revealed the absence of Mo scattering atoms. This reflects a poorly mixed alloy, as confirmed by the small contraction of the first shell Pt-Pt interatomic distance and small Pt-Mo coordination number with regards to the stochiometry. In addition, a Mo-Pt coordination number of 4 to 5 indicates that Pt is the dominant scatterer around the absorbing Mo atom. This information together with the observation of O backscatterer atoms at 1.95 Å, indicates that Mo is oxidised when a reducing potential is applied. This result agrees with the Mo K edge

XANES investigations that have suggested the presence of the Mo(IV)/Mo(VI) redox couple. This is consistent with previously reported XPS data that have concluded that Mo oxidation state of (IV) is present at potentials as low as - 0.55 V vs. MMS for PtMo bulk electrode [21]. Mukerjee *et al.* have recently reported preliminary XAS data at the Mo K edge for a carbon supported PtMo electrocatalyst. They have suggested that the oxidation state of the Mo is potential dependent using XANES spectra and the presence of $Mo(OH)_2^{2+}$ species at low potentials was suggested. Thereby, in the present case an oxyhydroxide form of Mo is assumed to be localised on the surface of the Pt particles. For instance, the *N*(Pt-Mo) of 1.8 ± 0.9 tends to correspond to the monolayer on the Pt surface evaluated earlier, i.e. 0.9. This is consistent with the fact that the Pt-Mo coordination number has shown no potential sensitivity and with the examination of the cyclic voltammogram comprising a large pseudo-capacitance.

The $PtMoO_x/C$ catalyst showed a potential dependance of the EXAFS data at the Mo K edge compared to that obtained for the PtMo/C. The oxidised form of the $PtMoO_x/C$ (the 'as prepared' catalyst) showed smaller Mo-Pt coordination numbers N(Mo-Pt) = 2.9 compared to that obtained at – 0.6 V, N(Mo-Pt) = 5.2, as well as shortened Mo-O coordination distance to 1.75 Å. This is consistent with other i*n situ* fluorescence studies at the Mo K edge for carbon supported platinum electrocatalysts modified with Mo using organometallic chemistry [22]. XAS data for the $PtMoO_x/C$ with a nominal surface coverage of the platinum surface by the molybdenum equivalent to *ca.* 0.1 monolayer have shown that at oxidative potentials Mo exists as an oxide associated with platinum, with a Mo-O bond distance of 1.75 Å. Upon electrochemical reduction, the oxide is reduced with formation of a metal-metal bond between Mo and Pt substrate at a bond distance of 2.63 Å.

In contrast, data analysis at the Ru K edge for Pt-Ru/C electrodes at reducing potentials has not required a Ru-O coordination distance. However, the modification of the electronic properties of Pt, as evidenced by the change in the Pt d-band vacancy has been confirmed for the well mixed PtRu alloy electrocatalyst.

5 CONCLUSION

The present work has demonstrated that EXAFS studies may be used to validate preliminary XRD results. *In situ* XAS results presented above provide evidence of the potential dependance of the carbon supported Pt and PtRu electrocatalysts. As the potential reaches an oxidative potential, the extension of the Pt-Pt inter-atomic distances and smaller Pt-Pt coordination number revealed the oxide formation on the Pt electrode which was not restricted to the Pt surface. *In situ* XANES data at the Pt edge for the PtRu/C well-mixed alloy electrocatalyst have shown that the presence of Ru enhanced greatly the Pt-d band vacancies at the potentials at which hydrogen oxidation occurs. Ru EXAFS data also verified the metallic nature of Ru at these reductive potentials. Therefore, the interplay of both electronic and geometric effects due to the introduction of Ru in the Pt particle and their combined role results in the modification of the chemisorptive behaviour of CO on the Pt sites.

In situ XAS results for the carbon supported PtMo electrocatalyst described a poorly mixed alloy system with Mo likely to be situated on the surface of the platinum particles. The Mo XAS study evidenced the Mo(VI)/Mo(IV) redox couple that confirmed the potential dependance of the Mo oxidation state as well as the oxidised form of Mo at low potentials. The electronic effect of the addition of Mo on the Pt atoms in the particles is weaker than that found for the PtRu/C. Also, very little lattice contraction, therefore, very little structural effect was observed for both the PtMo/C catalysts studied. Thereby, the promotional role of the oxyhydroxide species at the Mo sites for the CO electrooxidation was confirmed.

6 REFERENCES

[1] Attard, G.; Barnes, C., *Surfaces*; Oxford Science Publications: Oxford, 1998; Vol. 59.

[2] Malm, J.-O.; Bovin, J.-O.; Perford-Long, A.; Smith, D. J.; Schmidt, G.; Klein, N., *Angew. Chem.Int. Ed. Engl.*, **1988**, *27*, 555.

[3] Liang, K. S.; Chien, F. Z.; Hughes, G. J.; Meitzner, G. D.; Sinfelt, J. H., *J. Phys. Chem.*, **1991**, *95*, 9975.

[4] Duff, D. G.; Edwards, P. P.; Evans, J.; Gauntlett, j. T.; Jefferson, D. A.; Johnson, B. F. G.; Kirkland, A. I.; Smith, D. J., *Angew. Chem. Int. Ed. Engl.*, **1989**, *28*, 590.

[5] Mc Breen, J.; O'Grady, W. E.; Pandya, K. I., *J. Power Sources,* **1988**, *22*, 323.

[6] Binsted, N. Excurv98: Computer programme CCLRC Daresbury Laboratory, 1998.

[7] International, X. S. http://wwwxs4all.nl/~xsi The Netherlands.

[8] Zhang, H.; Wang, Y.; Fachini, E. R.; Cabrera, C. R., *Electrochem. Solid State Lett.*, **1999**, *2*, 437.

[9] Yoshitake, H.; Mochizuki, T.; Yamazaki, O.; Ota, K.-I. *J. Electroanal. Chem.*, **1993**, *361*, 229.

[10] Ressler, T.; Timpe, O.; Neisius, T.; Find, J.; Mestl, G.; Dieterle, M.; Schlogl, R. *Journal of Catalysis,* **2000**, *191*, 75-85.

[11] Mukerjee, S.; Lee, S. J.; Ticianelli, E. A.; McBreen, J.; Grgur, B. N.; Markovic, N. M.; Ross, P. N.; Giallombardo, J. R.; DeCastro, E. S., *Electrochem. Solid State Lett.*, **1999**, *2*, 12.

[12] Bockris, J. O. M.; Srinivasan, S., *Fuel Cells: their electrochemistry*; McGraw-Hill, Inc: New York, 1969.

[13] Meitzner, G.; Via, G. H.; Lytle, F. W.; Sinfelt, J. H., *J. Phys. Chem.*, **1992**, *96*, 4960.

[14] Brown, M.; Peierls, R. E.; Stern, E. A., *Phys. Rev. B,* **1977**, *15*, 738.

[15] Mansour, A. N.; Cook, J. W.; Sayers, D. E., *J. Phys. Chem.*, **1984**, *88*, 2330.

[16] Mukerjee, S.; McBreen, J., *J. Electrochem. Soc.*, **1996**, *143*, 2285.

[17] Kittel, C., *Introduction to Solid State Physics*, 6th ed.; Wiley: New York, 1986.

[18] Benfield, R. E., *J. Chem. Soc. Faraday trans.*, **1992**, *8*, 1107.

[19] Khanna, S. N.; Butcher, J. P.; Buttet, J., *Surf. Sci.*, **1983**, *127*, 165.

[20] Herron, M. E.; Doyle, S. E.; Pizzini, S.; Roberts, K. J.; Robinson, J.; Hards, G.; Walsh, F. C. *Journal of Electroanalytical Chemistry,* **1992**, *324*, 243-358.

[21] Grgur, B. N.; Markovic, N.; Ross, P. N., *J. Phys. Chem. B,* **1998**, *102*, 2494.

[22] Crabb, E. M.; Ravikumar, M. K.; Qian, Y.; Russell, A. E.; Maniguet, S.; Yao, J.; Thompsett, D.; Hurtford, M.; Ball, S. C., *Electrochem. Solid State Lett.*, **2002**, *5*, A5-A9.

There is no page 102

CHAPTER FIVE : EXAFS OF CO OXIDATION ON CARBON SUPPORTED PT ELECTROCATALYST

*The results presented in this chapter have been published elsewhere :
Maniguet, S.; Mathew, R. J.; Russell, A. E.; *Journal of Physical Chemistry B*, **2000**, 104, 1998-2004.

1. INTRODUCTION

Interest in the electrooxidation of CO adsorbates on noble metal surfaces (Pt, Rh, Au,..) can be attributed to the large participation of CO in many electrocatalytic reactions. CO can be either a reactant or product (intermediate) for the production (e.g. Fisher-Tropsch reaction) or the reforming of hydrocarbons and other organic compounds, respectively. As said before (Chapter 1), the latter process provides H_2 rich fuel that is widely used to supply the anode compartment in PEMFCs. Hence, trace levels of CO (30 ppm to 100 ppm) may be present in the H_2 rich reformate fuel stream or CO may be formed during the course of the electrooxidation of small molecules such as methanol. The CO poisons Pt-based fuel cell electrocatalysts. In poisoning the surface, CO blocks Pt sites available for hydrogen (or methanol) oxidation reaction, subsquently, leading to anode deactivation.
Since CO plays a key role in the understanding of the reaction mechanism of electrocatalytic oxidations, researchers sought to explain the electrosorption of CO on noble metal surfaces as well as the following oxidation of CO_{ads} to CO_2. In addition, the electrooxidation of CO adsorbates on noble metal surfaces has been widely used as a test reaction in order to develop spectroscopic techniques in surface science.

Earlier, potentiodynamic experiments, such as cyclic voltammetry enabled the adsorbed species at the electrode surface to be quantified. The number of electrons involved in the CO oxidation reaction (determined by coulometric charge under CO stripping peak) was directly correlated to the number of adsorption sites and by extension to the geometry of $CO_{adsorbed}$ molecules. Many groups reported the voltammetric determination of the CO coverage corresponding to full blocking of the hydrogen adsorption sites on smooth single crystal Pt electrodes such as Pt(111), Pt(110) and Pt (100) in aqueous acid solutions [1], [2].

Infrared spectroscopic experiments were also used to identify the various CO adsorbed species such as linearly, bridge or multifold bonded CO to Pt, that were appearing at distinct potentials in the voltammetry [3]. Further, the possibity to record vibrational spectra of adsorbed species at the electrode/electrolyte solution interface by modulating the electrode potential was achieved using the electrochemically modulated infrared spectroscopy (EMIRS) technique. For instance, Beden *et al.* have reported for CO adsorption on Pt in aqueous CO saturated solution, linearly and bridge bonded species that are detected at 2080 cm^{-1} and 1860 cm^{-1}, respectively. These solid/liquid EMIRS results were reported similar to the solid/gas phase reflectance absorption infrared spectroscopy (RAIRS) investigations [4]. Recently, Gomez *et al.* have reported similarity between saturated CO coverages on Pt(111) obtained by voltammetric evaluation and adlayer structural informations obtained from *in situ* scanning tunneling microscopy (STM) along with infrared spectroscopy, and also with structural data for corresponding adlayers in ultrahigh vacuum (UHV) [5].

As seen in previous examples as well as in the literature, the identification of CO_{ads} species on smooth polycrytalline platinum or platinum single crystal surface is feasible using infrared spectroscopy. (Those surfaces being highly reflective to the IR beam). However, anode fuel cell electrodes are using carbon supported small platinum particles as the catalysts (crystallite size of 2 nm to5 nm). Since the surface of a metal particle consists of atoms with different coordination numbers due to their location at edges, corners and steps, one can expect the chemisorption of CO to be partly different from the mechanistic obtained from bulk surface (containing less structural defects). At present, few groups have reported *in situ* IR study on highly dispersed platinum particles. Christensen *et al.* have succeeded for the electrooxidation of methanol on basal plane graphite substrate supported small platinum particles using *in situ* FTIR spectroscopy [6]. They have reported that the methanol electrooxidation reaction was sensitive to the morphology of the particle. They have also obtained different results in comparison to similar investigations on bulk platinum. For instance, the methanol chemisorption on platinum particles takes place at more negative potentials with a dominant threefold CO_{ads} geometry while linearly bonded CO_{ads} is more predominant on bulk platinum.

As explained before, *in situ* X ray absorption spectroscopy offers the possibility of investigating fuel cell catalysts under electrochemical conditions, close to the operating fuel cell conditions. Though *in situ* XAS studies have shown structural and electronic effects for

carbon supported platinum based electrocatalyst in presence of CO, methanol or oxide, the identification of CO adsorbates has not been yet reported.

To improve the understanding of the chemisorption and the electrooxidation reaction of CO on carbon supported Pt catalysts, *in situ* XAS data measurements were carried out. Based on a difference file technique which allows the determination of low atomic number backscatters such as C or O, XAS data analysis have revealed the presence of the CO adsorbate on the platinum surface.

2. EXPERIMENTAL

2.1.Materials

A 40 wt. % Pt/XC-72R catalyst supplied by Johnson Matthey was formulated into an electrode using the procedure described in chapter 2, section 2.1. (The crystallographic parameters of this catalyst obtained from XRD measurements were given in chapter 4, section 2.1). Prior to XAS measurements, electrodes were boiled in triply distilled water to ensure a fully flooded state.

2.2. XAS experiments

In situ XAS measurements were performed at the Pt L_{III} edge in transmission detection mode on wiggler station 9.2 at Daresbury (SRS) laboratory. For the experimental set-up and experimental procedure refer to chapter 2, sections 6.4.2 and 6.4.4, respectively. The electrode was placed in the XAS cell and was exposed to CO prior to XAS data collection. This was done by purging with CO gas for 15 minutes through the reservoir containing the electrolyte (i.e. 1 mol dm^{-3} H_2SO_4) that, in turn, flowed through the cell, as well as purging CO acros the back face of the catalyst electrode. During the pretreatment, the electrode potential was held at – 0.6 V vs. MMS. Further, XAS spectra were recorded at successive potentials: – 0.6, - 0.4, - 0.2, - 0.1, 0 and 0.4 V vs. MMS for a single electrode, along with recording the cyclic voltammogram.

2.3.Data analysis

Data reduction and data analysis were performed using the XDAP package [7]. Raw XAS data were background substracted as described in chapter 2, section 6.3.1. Then, normalised data were processed using multiple shell fitting in *r*-space in order to extract the following structural parameters; coordination numbers (*N*), interatomic distances (*R*) and the Debye-Waller factor ($\Delta\sigma^2$), for each backscattering atoms.

Firstly, a Fourier filtering technique was used to isolate the shell contribution of interest. The *r*-window choosen will be specified in the following results section. The shell contribution can be clearly seen by direct comparison of the absolute and imaginary parts of the Fourier transform.

Experimental references were used to obtain the backscattering phase shifts and amplitudes for the Pt-Pt and Pt-O contributions using a Pt foil and $Na_2Pt(OH)_6$, respectively, with the following crystallographic parameters ; N = 12, R = 2.77 Å for the Pt foil and N = 6, R = 2.05 Å for the $Na_2Pt(OH)_6$. Since no reference compound was available for Pt-C, a theoritical Pt-C reference foil was calculated using FEFF3.1 [8], with the following parameters ; N = 4, R = 1.99 Å, $\Delta\sigma^2 = 0.002$ Å^2 and $S_o^2 = 0.93$.

The difference file technique was used to determine the different backscatterers within a restricted *r*-window. This can be expressed by the following equation [9] :

$$\chi_i = \chi_{experimental} - \sum_{j=1, j\neq i}^{n} \chi_j \qquad \text{Equation 1}$$

where χ_i is a single scattering contribution in a model contribution,

$\chi_{experimental}$ is the experimental EXAFS signal,

$\sum_{j=1}^{n} \chi_j$ is the sum of all the model contributions (χ_{model})

In this technique, the parameters *R*, *N* and $\Delta\sigma^2$ (relative to the reference compound) of the largest contribution (i.e. Pt-Pt contribution in our case) in the spectrum are firstly estimated from a spectrum in *r*-space. This latter spectrum was obtained by Fourier transformation, phase and/or amplitude corrected for the atom type, namely Pt, which causes the largest contribution. Those estimated parameters were used to calculate the corresponding EXAFS

function that was substracted from the experimental EXAFS signal. From the remaining EXAFS signal again, the largest contribution, i.e. Pt-C and/or Pt-O, was then fitted. During any iteration process, the number of free parameters was restricted while optimising the fit. A comparison of the data in *r*-space and fits have led to results presented in the following section.

The fit quality was determined by the variance in the absolute and imaginary parts given by Equation 2, as previously described by Mojet *et al.* [9].

$$k^n variance = 100 \frac{\int \left[k^n \left(FT_{model}(R) - FT_{experiment}(R)\right)\right]^2}{\int \left[k^n FT_{experiment}(R)\right]^2} \qquad \text{Equation 2}$$

Models with variances in absolute and imaginary parts below 1% are considered to represent very good models for experimental data. The error in the fit parameters are estimated to be 5 to 10% in the coordination number (N), 1% in interatomic distance (R), 5% to 10% in Debye-Waller factor ($\Delta\sigma^2$) and 10% in inner potential correction (ΔE_o).

In addition, the correctness of the fitted parameters data set was verified by k^n-weighting (with n = 1, 2 or 3) the data and the Fourier transforms. As it was mentioned before, k^n-weighting emphasises the scatterer in a specific region. Low Z (atomic number) atom (e.g. C and O) scatterers contribute more at low k-values while higher Z atom (e.g. Pt) scatterers contribute more at high k-values. Therefore, k^3-weighting confirms the quality of the fits for the isolated (Pt-Pt) contribution, whereas k^1-weighting confirms the isolated (Pt-O) and (Pt-C) contributions. k^2-weighting provides a compromise between these two extremes and has been used in isolating the first shell contributions (Fourier filtering) prior to the fitting. The quality of the overall fit was examined using both k^1 and k^3-weightings.

3. RESULTS

3.1. EXAFS of CO covered Pt/C fuel cell electrode

Figure 1 shows k^1-weighted experimental EXAFS data, in panels (a) and (c) and the corresponding Fourier transforms, in panels (b) and (d) for the Pt/C electrode at – 0.6 V

when exposed to CO. (As said before, k^1-weighting was chosen to emphasise the low Z neighbouring atoms backscattering contributions, such as C and O atoms). The solid line corresponds to the experimental data with a high signal to noise ratio indicating good data quality which may be analysed up to 17 $Å^{-1}$. Both dashed and dotted lines represent the best fits obtained after r-space analysis of the data after Fourier filtering. The filter conditions such that $2 \leq k \leq 17$ $Å^{-1}$ and $1.2 \leq r \leq 3.4$ Å were applied over a k^2-weighted Fourier transform to isolate the first Pt-Pt contribution. Further, both the first and second Pt shells were isolated with the following filter conditions; $2 \leq k \leq 17$ $Å^{-1}$ and $1.1 \leq r \leq 4.0$ Å.

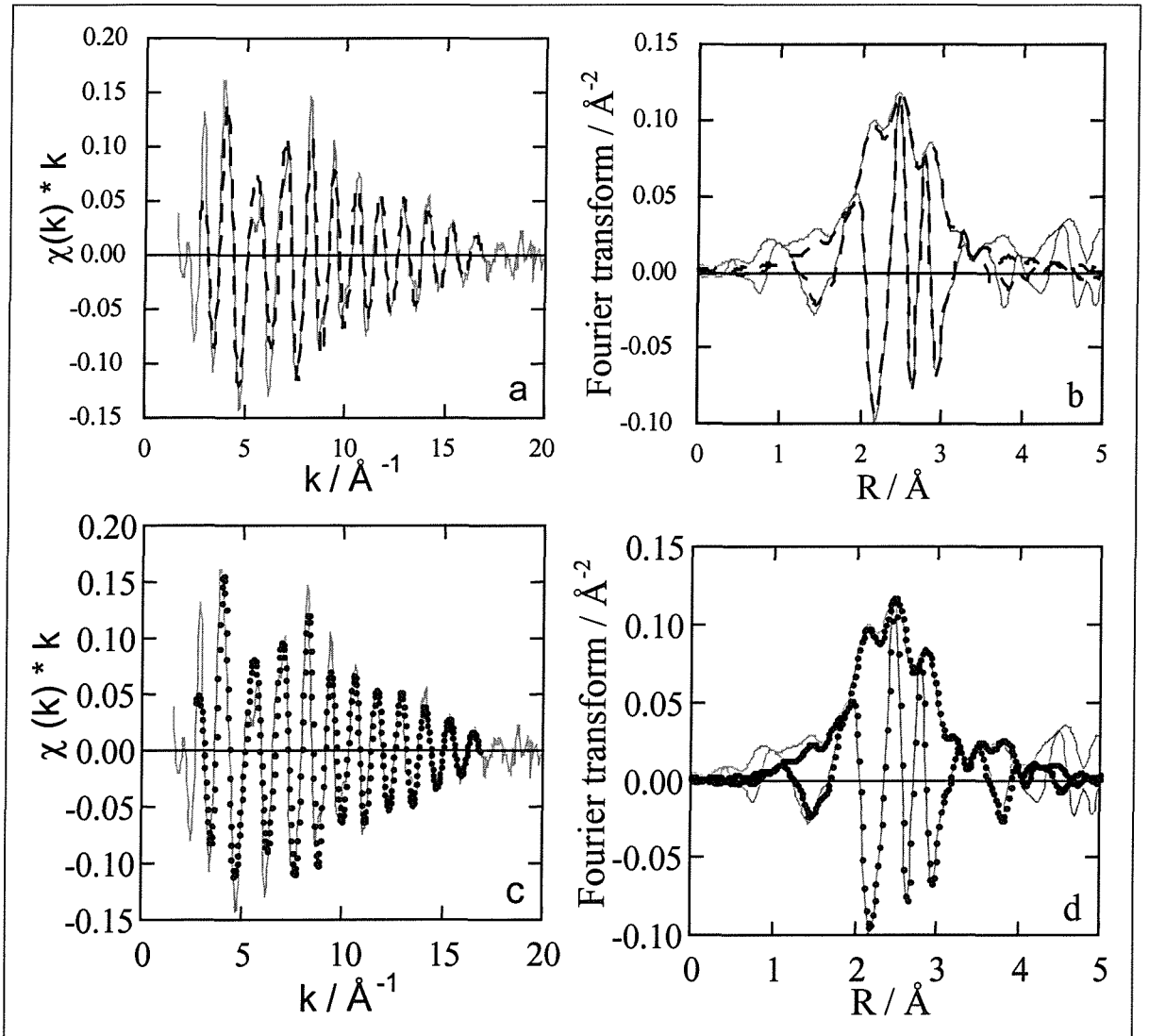

Figure 1 : (a) and (c) k^1-weighted experimental data (not Fourier filtered) at - 0.6 V vs. MMS (solid line) and fits, including (a) only first Pt-Pt distance (dashed line) and (c) both first and second Pt-Pt distances (dots), for Pt/C fuel cell electrode in 1 mol dm^{-3} H_2SO_4 following CO exposure. (b) and (d) k^1-weighted Fourier transforms, $3.1 \leq k \leq 14$ $Å^{-1}$, of the data and fits of spectra in (a) and (c), respectively.

It should be noticed that the fit of the second (Pt-Pt) shell implies no significant phase and amplitude change in the Chi(k) plots in panels (a) and (c). As seen in FTs, the resulting r-space position for both Pt contributions is in fair agreement with results presented in previous chapters; the first Pt shell is situated between 2 Å and 3 Å (dashed line in panel (b)) and the second shell Pt contribution at about 3.8 Å (dotted line in panel (d)).

The difference file technique was applied to both models. That is, when the first Pt-Pt coordination distance (model 1) and both first and second Pt-Pt coordination distances (model 2) were included in the fit.

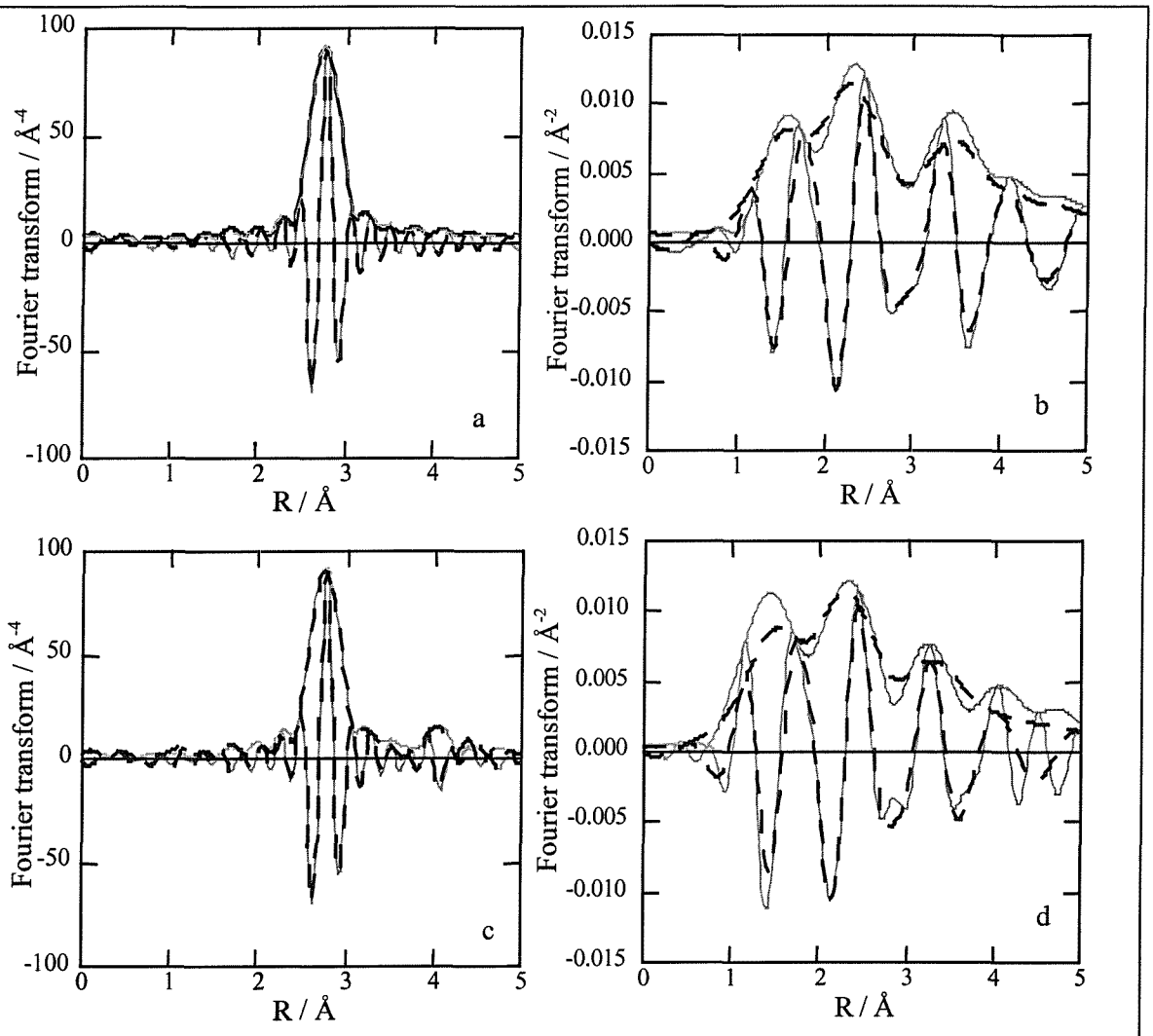

Figure 2 : Difference plots corresponding to fits in Figure 1. (a) and (b) fit including only first Pt-Pt distance, (c) and (d) fit including both first and second Pt-Pt distances. Panels (a) and (c) k^3-weighted Fourier transform, 3.5 $\leq k \leq$14 Å^{-1}, Pt phase and amplitude corrected,[isolated experimental EXAFS data – fit of C neighbours] (solid line) and fit of Pt neighbours (dashed line). Panels (b) and (d) k^1-weighted Fourier transform, 3.5 $\leq k \leq$9 Å^{-1}, C phase corrected, [isolated experimental EXAFS data – fit of Pt neighbours] (solid line) and fit of C neighbours (dashed line).

Figure 2, panels (a) and (c) compare Pt phase and amplitude corrected k^3-weighted FTs of the isolated experimental data minus the fit of the C neighbours (solid line) with the one corresponding to the fit of the Pt neighbours (dashed line). The fits of the Pt neighbours overlap correctly with the experimental data for both models. The main peak at 2.76 Å was ascribed to the first Pt-Pt contribution and the peak at 3.97 Å was ascribed to the second Pt-Pt contribution. Inversely, panels (b) and (d) compare C phase corrected k^1-weighted FTs of the isolated experimental data minus the fit of the Pt neighbours (solid line) with the one resulting from the fit of the C neighbours (dashed line). The radial distribution function consists of three main peaks that characterise the C backscatterer contribution around the Pt central atom. The resulting structural parameters are presented in Table 1.

Model	Scatterer	N[a]	R/Å (± 1%)	$10^3\,\Delta\sigma^2$/Å (± 5%)	ΔE_0/eV (± 10%)	k^0 variance (%) im part	abs part
1	Pt	9.39	2.76	3.7	2.1	0.07	0.06
	C	0.55	1.85	9.0[b]	9.0		
	C	1.36	2.71	9.0[b]	-13		
	C	1.91	3.70	9.0[b]	-13		
2	Pt	9.39	2.76	3.7	2.1	0.03	0.01
	Pt[c]	4.03	3.97	3.9	-12		
	C	0.60	1.85	9.0[b]	8.9		
	C	1.36	2.72	9.0[b]	-13		
	C	1.36	3.62	9.0[b]	-13		

Table 1: Fit parameters and variances for model spectra for Pt/C with CO_{ads} at -0.6 V *vs.* MMS.

a. N ± 5% for Pt-Pt shell and ± 10% for Pt-C shells.
b. Parameter fixed during fitting.
c. N ± 20%.

The first Pt-C coordination distance at 1.85 Å was attributed to the C of the adsorbed CO. This assignment agrees well with both the distance obtained for CO adsorbed on zeolite supported Pt particles, 1.92 Å, [9] and *ab initio* cluster calculations [10]. The two remaining Pt-C contributions fitted at 2.71 Å and 3.70 Å can be assigned to C from the support, in agreement with results previously reported in the literature [11]. Also, large inner potential shifts have been obtained for both Pt-C shells. This can be explained by the existence of multiple Pt-C distances at the interface of Pt and C close to each other, all contributing to the XAS signal and accounting for the C scattering when fitted in one shell [12].

It should be noted that fit parameters change slightly when the second Pt–Pt coordination distance is included in the analysis. This is particularly true for the third Pt-C shell, being a close distance neighbour of the Pt-Pt at 3.97 Å.

The following step of the experiment was to increase the electrode potential to study how the potential affects the EXAFS of the Pt/C electrode exposed to CO.

3.2.Potential dependance of the EXAFS

The electrode potentials were applied depending on the onset potential of the oxidation of CO. Thereby, EXAFS spectra were collected at potentials applied before (e. g. - 0.6, - 0.4, - 0.2 and - 0.1 V) and after CO oxidation (e.g. 0 V); also, during the oxidation of platinum (e.g. 0.4 V) and finally, back to the double layer region at - 0.2 V.

Figure 3 shows cyclic voltammograms for the Pt/C electrode after CO exposure recorded in the electrochemical half-cell. Though less resistive, this is representative of the cyclic voltammograms recorded in the thin layer electrochemical XAS cell.

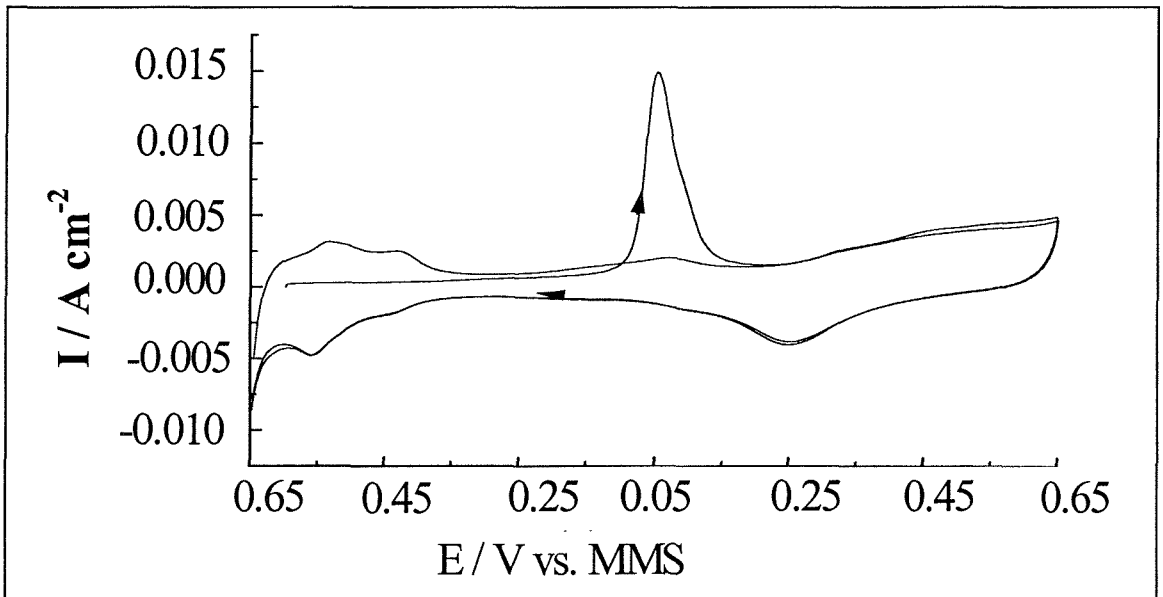

Figure 3 : Cyclic voltammogram of Pt/C fuel cell electrode (electrode area 1 cm^2) in 1 mol dm^{-3} H_2SO_4. Electrode surface exposed to CO saturated solution while the potential was held at – 0.6 V *vs.* MMS. After adsorption, CO was displaced from solution by N_2 bubbling for 15 mins. Sweep rate 10 mV s^{-1}.

Figure 4 (overleaf) compares k^2-weighted FTs of the experimental EXAFS data for the Pt/C electrode following CO exposure as the applied potential increases from – 0.6 to 0.4 V, and,

finally, returned to – 0.2 V. Panel (a) shows clearly that the shape and amplitude of the radial distribution function obtained for – 0.6 V (CO adsorbed) overlaps with that of 0 V (after CO oxidation).

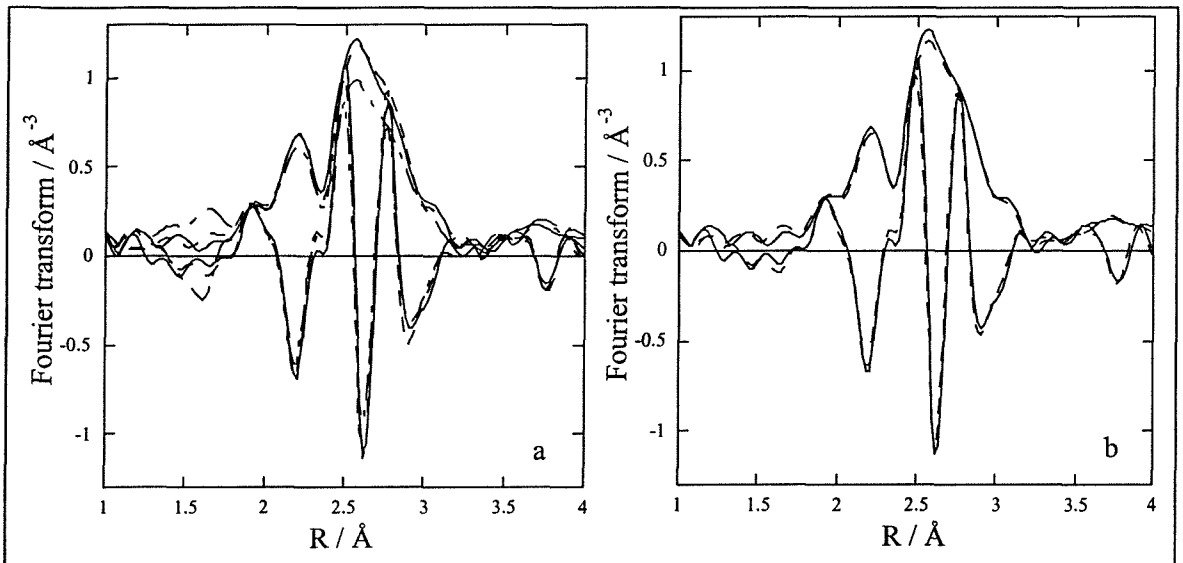

Figure 4 : k^2-weighted Fourier transform, 3.1 $\leq k \leq$14 Å^{-1}, of the experimental EXAFS data of the CO exposed Pt/C electrode obtained at: (a) - 0.6 V (solid line), 0 V (dashed line) and 0.4 V (dot dashed line), note that the Fourier transforms of the – 0.6 V and 0 V data largely overlap; and (b) – 0.2 V with adsorbed CO (solid line) and 0.2 V* after CO oxidation (dashed line). All potentials *vs.* MMS.

Though it is not included in the plot, it has been verified that the FT features of the data obtained at – 0.2 V (before CO oxidation) overlap with both previous ones. In contrast, the amplitude of the FT decreases significantly at 0.4 V corresponding to the onset potential where platinum is oxidised. This observation is in fair agreement with the results reported in the previous chapter as well as in the literature [13]. Thereby, in contrast to CO adsorption, the presence of oxide species affects Pt-Pt coordination number. In addition, panel (b) compares the k^2-weighted FT of the experimental data obtained prior (e.g. - 0.2 V) and after CO oxidation (e.g. – 0.2 V*) and shows an amplitude decrease of the FT indicating that the electrode surface has not fully recovered from the oxidation reactions.

Prior to further analysis in *r*-space using the difference file technique, data were Fourier filtered to ensure that only the contribution of the first Pt-Pt coordination shell (model 1) was included. The filter conditions were defined in the previous section for model 1 such that 2 $\leq k \leq$17 Å^{-1} and 1.2 $\leq r \leq$3.4 Å. Table 2 summarises the fit parameters obtained as the potential increases. At potentials below the onset potential of CO oxidation (e.g. below

- 0.1 V), the best fits have been obtained with one Pt-Pt contribution and three Pt-C contributions. The first Pt-C coordination distance at 1.85 Å assigned to the C of CO adsorbed is absent from - 0.1 V. Also, at potentials above – 0.1 V, shortened interatomic distances characterise the two remaining Pt-C contributions assigned to the support ; this is particularly pronounced for the longest Pt-C distances, i.e. 3.7 Å against 3.3 Å. In addition, the second Pt-C shell exhibits larger disorder (e.g. $\Delta\sigma^2 = 0.009$ Å^2) than the first Pt-C (e.g. $\Delta\sigma^2 = 0.004$ Å^2) which is consistent with higher disorder at higher coordination distance.

E / V *vs.* MMS	Neighbour	N[a]	R/Å (± 1%)	$10^3\,\Delta\sigma^2$/Å^2 (± 5%)	ΔE_o/eV (± 10%)	k^0 variance (%) im part	abs part
- 0.4	Pt	9.26	2.76	3.7	1.9	0.03	0.01
	C	0.43	1.85	9.0[b]	9.0		
	C	1.58	2.72	9.0[b]	-13		
	C	1.94	3.69	9.0[b]	-11		
- 0.2	Pt	9.23	2.76	3.6	1.3	0.03	0.01
	C	0.51	1.85	9.0[b]	9.0		
	C	1.44	2.71	9.0[b]	-13		
	C	2.32	3.71	9.0[b]	-12		
- 0.1	Pt	9.22	2.75	3.7	1.9	0.03	0.01
	C	1.45	2.66	4.0[b]	-9		
	C	2.14	3.32	9.0[b]	-11		
0	Pt	9.22	2.75	3.7	1.9	0.12	0.08
	C	1.63	2.64	4.0[b]	-8.9		
	C	2.32	3.30	9.0[b]	-11		
0.4	Pt	8.11	2.76	4.0	1.7	0.04	0.02
	O	0.75	2.00	2.9	13		
	C	2.15	2.64	4.0[b]	-10		
	C	3.97	3.24	9.0[b]	15		
- 0.2*	Pt	8.83	2.75	3.7	2.3	0.03	0.01
	C	1.56	2.64	4.0[b]	-9.0		
	C	1.53	3.55	9.0[b]	-5.8		

Table 2: Fit parameters and variances for model spectra for Pt/C as a function of potential.

a. N ± 5% for Pt-Pt shells and ± 10% for Pt-C shells.
b. Parameter fixed during fitting.

The Pt-O coordination distance at 2.00 Å corresponds to the oxide formation at 0.4 V. This is consistent with both the decrease in the amplitude of the FT observed previously and smaller first shell Pt-Pt coordination number (e.g. $N_1(\text{Pt-Pt})_{-0.6\ V} = 9.26$ and $N_1(\text{Pt-Pt})_{0.4\ V} = 8.11$).

Figure 5 illustrates separately both the Pt contribution (panels (a), (c) and (e)) and the C and O contributions (panels (b), (d) and (f)), within the first coordination sphere.

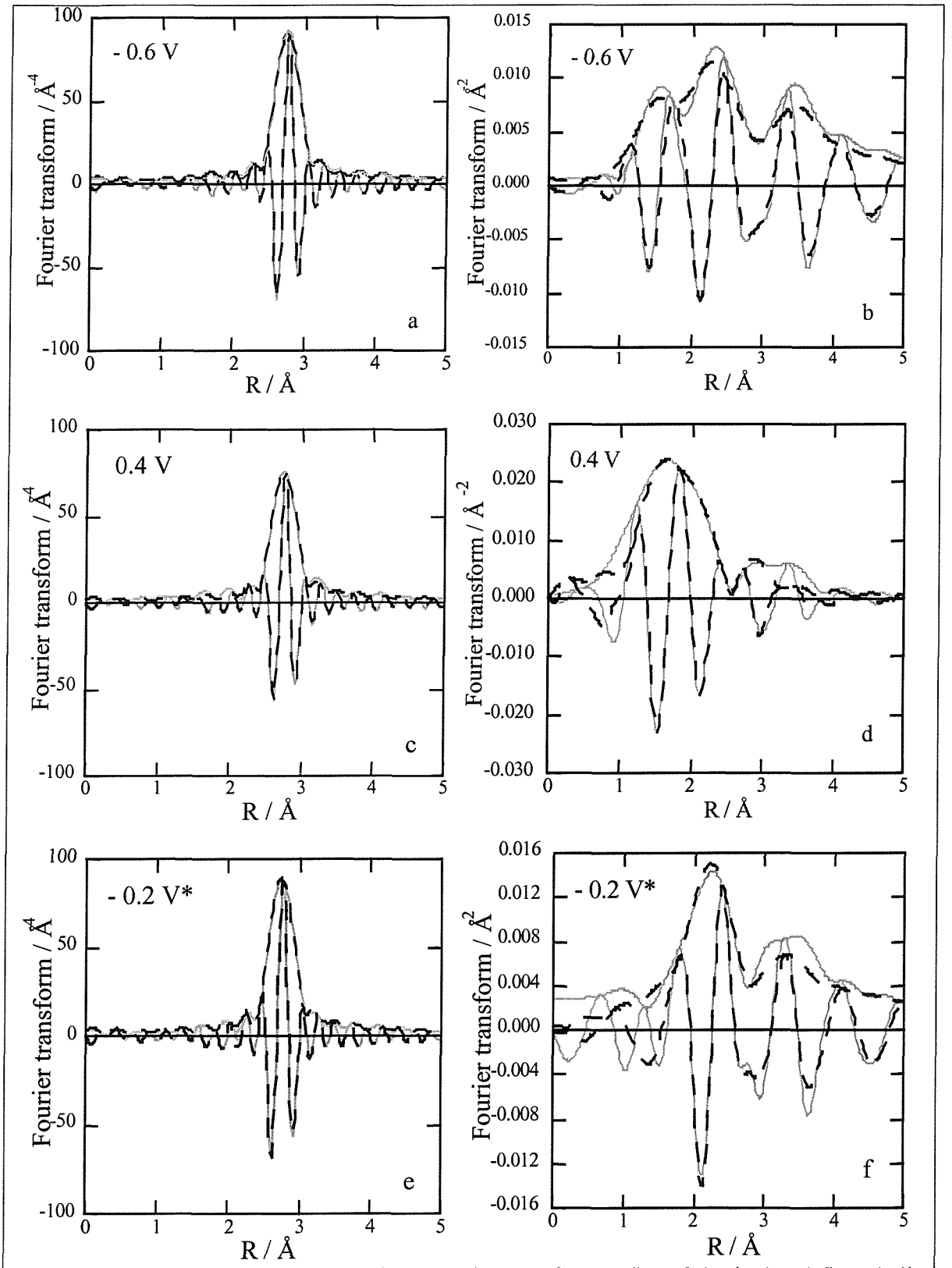

Figure 5 : Difference plots as described in Figure 2 for the fits of the isolated first shells of the data obtained at (a) and (b) - 0.6 V (CO adsorbate present), (c) and (d) 0.4 V (Pt surface oxidised) and (e) and (f) - 0.2 V* (after CO oxidation). All potentials *vs.* MMS.

k^3-weighted FTs show the well-rehearsed change in amplitude at the potential of oxide formation as well as the similarity between the shape and amplitude of the FT obtained at - 0.2 V* (after CO oxidation) and – 0.6 V. This result indicates that the electrode has recovered from the oxide adsorption which implies no restructuration since the Pt-Pt interatomic distances do not change.

In contrast, the shape and the amplitude of the k^1-weighted data FTs that reflect the C and O contributions in the first coordination shell change dramatically as the potential increases. This is due to the presence of different backscattering atom around the Pt center atom as indicated by fit parameters in Table 2. In panel (b), three peaks characterise the feature of the FT at potential below – 0.1 V, where CO is adsorbed onto the surface of the electrode. This results from the backscattering effect of the C of the CO_{ads} at 1.85 Å and from the support at 2.7 and 3.7 Å. In panel (d), the amplitude of the FT has increased at low R values (i.e. about 2 Å) as the potential reached 0.4 V (after CO oxidation). Thus, the Pt-O contributions overtake and mask that of Pt-C from the support illustrated in panel (f).

4. DISCUSSION

The dominant backscattering phase and amplitude contributions of Pt neighbouring atom observed in the isolated first shell (Figure 5 a, c and e), together with Pt-Pt distance similar to the Pt-Pt distance in the Pt foil (2.77 Å) (Table 1 and Table 2) obtained for Fourier filtered XAS data with or without CO have evidenced the metallic nature of the carbon supported platinum catalyst. This agrees well with results obtained before, using the EXCURV98 program as well as reported in the literature for supported Pt catalysts [14]. The averaged first shell (Pt-Pt) coordination number ($N_{Pt\text{-}Pt}$) can be correlated to the platinum particle size, that was firstly determined by TEM mesurements with a crystallite size of 2-3 nm. When using Benfield's formula [15] for an icosahedral particle shape, $N_{Pt\text{-}Pt}$ of 8.51 corresponds to a 55 atom cluster, $N_{Pt\text{-}Pt}$ of 9.47 to a 147 atom cluster and $N_{Pt\text{-}Pt}$ of 10.02 to a 309 atom cluster. The number of surface atoms for each of these clusters are 42, 92 and 162, respectively. The similarity of fit parameters (coordination number and distance) obtained for the first (Pt-Pt) shell prior and after the electrooxidation of CO indicates no restructuring of the Pt particles. Thereby, CO that has been evidenced by the fit

of the Pt-C coordination distance at 1.85 Å, is adsorbed on the surface of Pt particles. The corresponding Pt-C coordination number is 0.5 and reflects well the monolayer of CO adsorbed on the Pt surface, which has been estimated between 0.45-0.63 by the ratio of the number of surface atoms / total number of atoms. In contrast, the formation of the oxide is not resticted to the surface of the particle as indicated by the decrease in the first Pt-Pt coordination number. The large inner potential corrections observed for the C shells attributed to the Pt particle / C support interface, have previously been attributed to fitting several closely spaced Pt-C distances as one distance [12]. The large Debye-Waller factors also agree with this interpretation.

The Pt-C bond distances for adsorbed CO as determined in the *ab initio* calculations of Curulla *et al.* [10] are 1.86 to 1.90 Å for CO adsorbed at the on-top/linear site and 1.44 Å to 1.49 Å for CO adsorbed at the bridge bonded site, using a 29 Pt atom cluster. The Pt-C distance obtained in this investigation, 1.85 Å, therefore suggests that the CO is adsorbed linearly, although the presence of bridge bonded CO can not be excluded. At potentials where CO is adsorbed additional longer Pt-C and Pt-O distances will also be present. If the CO is assumed to be adsorbed linearly, then a Pt-O neighbour would be expected at 2.95 Å and a Pt-C neighbour at 3.32 Å. The presence of the C neighbours from the support make a statistically significant observation of the Pt-O bond distance for the adsorbed CO, reported at 2.86 Å for the zeolite supported Pt particles [9], difficult. In addition, the backscattering phase shifts and amplitudes for the C and O neighbours are very similar. It is therefore, not feasible to investigate the influence of the applied electrode potential on the C-O bond length for C supported Pt particles. *In situ* infrared studies of CO adsorbed on smooth Pt surfaces have shown that the frequency of the ν(CO) stretching vibration is dependent on the applied electrode potential or electric field strength. This phenomenon, known at the electrochemical Stark effect, has been attributed to both a potential dependent change in the π-back bonding between the Pt d electrons and the π^* anti-bonding orbital of adsorbed CO and a coupling of the dynamic dipole of the C-O bond with the electric field strength [16]. A change in the Pt-C and C-O bond lengths with applied potential was, therefore anticipated. No change in the Pt-C distance was observed over the –0.6 V to - 0.2 V potential region investigated in this study.

Cyclic voltammograms recorded along with XAS spectra ensure the consistency of the XAS data analysis. The absence of the hydride region from – 0.6 V to – 0.1 V, in the first forward

sweep (Figure 3, scan 1) after CO exposure confirmes the blocking phenomenom due to CO adsorbates on Pt surface which were determined, below, by the Pt-C shell at 1.85 Å. The disappearence of the latter coordination distance at – 0.1 V corresponds with the onset potential of CO electrooxidation as seen in Figure 3. Free from CO, the platinum surface is oxidised, as observed at 0.4 V together with the Pt-O coordination distance at 2 00 Å. The inner potential correction and Debye-Waller factor for the Pt-C shell at 2.6Å for the fits of the data obtained at - 0.1 V and 0 V are reduced in comparison to those where CO is adsorbed. At these potentials, where CO is removed, but prior to oxide formation, fewer closely spaced Pt-C distances are present.

5. CONCLUSION

This investigation has shown that *in situ* XAFS of fuel cell electrocatalysts is sensitive to the surface composition of the metal particles and may be used to investigate the chemistry of the fuel cell reactions. The use of the difference file method enables subtraction of the dominant Pt-Pt interactions and detailed examination of the remaining non-Pt neighbours. The EXAFS fit parameters obtained in this study are consistent with the adsorption of a monolayer of CO on the Pt particles. The presence of contributions to the EXAFS from the C neighbours of the support prevent the determination of the effect of the applied potential on the C-O bond length and independent discrimination between the various possible adsorption sites; e.g. linear, bridge, or multi-fold bonding.

6. REFERENCES

[1] Orts, J. M.; Fernandez-Vega, A.; Feliu, J. M.; Aldaz, A.; Clavilier, J., *J. Electroanal. Chem.*, **1992**, *327*, 261.

[2] Weaver, M. J.; Chang, S.-C.; Leung, L.-W. H.; Jiang, X.; Rubel, M.; Szklarczyk, M.; Zurawski, D.; Wieckowski, A., *J. Electroanal. Chem.*, **1992**, *327*, 247.

[3] Beden, B.; Lamy, C.; De Tacconi, N. R.; Arvia, A. J., *Electrochimica Acta,* **1990**, *35*, 691.

[4] Beden, B.; Bewick, A.; Kunimatsu, K.; Lamy, C., *J. Electroanal. Chem.*, **1982**, *142*, 345.

[5] Gomez, R.; Feliu, J. M.; Aldaz, A.; Weaver, M. J., *Surf. Sci.*, **1998**, *410*, 48.

[6] Christensen, P. A.; Hamnett, A.; Munk, J.; Troughton, G. L., *J. Electroanal. Chem.*, **1994**, *370*, 251.

[7] International, X. S. http://wwwxs4all.nl/~xsi The Netherlands.

[8] Rehr, J. J.; Albers, R. C.; Zabinsky, S. I., *Phys. Rev. Lett.*, **1992**, *69*, 3397.

[9] Mojet, B. L.; Miller, J. T.; Koningsberger, D. C., *J. Phys. Chem. B,* **1999**, *103*, 2724.

[10] Curulla, D.; Clotet, A.; Ricart, J. M.; Illas, F., *J. Phys. Chem.*, **1999**, *103*, 5246.

[11] Lampitt, R. A.; Carrette, L. P. L.; Hogarth, M. P.; Russell, A. E., *J. Electroanal. Chem.*, **1999**, *460*, 80.

[12] Mojet, B. L.; Hoogenraad, M. S.; van Dillen, A. J.; Geus, J. W.; Koningsberger, D. C., *J. Chem. Soc., Faraday trans.*, **1997**, *93*, 4371-4375.

[13] Yoshitake, H.; Mochizuki, T.; Yamazaki, O.; Ota, K.-I., *J. Electroanal. Chem.*, **1993**, *361*, 229.

[14] Koninsberger, D. C.; Prins, R. *X-Ray Absorption: Principles, Applications, Techniques of EXAFS, SEXAFS , and XANES*; Wiley: New York, 1988.

[15] Benfield, R. E., *J. Chem. Soc. Faraday trans.*, **1992**, *8*, 1107.

[16] Holloway, S.; Norskov, J. K., *J. Electroanal. Chem.*, **1984**, *161*, 193.

CHAPTER SIX : CATALYSIS OF PT BASED CARBON SUPPORTED FUEL CELL CATALYSTS

1 INTRODUCTION

As said before hydrogen-rich fuels produced by reforming or partial oxidation of hydrocarbons are preferentially used to supply polymer electrolyte membrane fuel cells (PEMFCs). Trace level of CO (2%) and high concentration of CO_2 (20% to 25%) invariably present in the fuel stream dictate the commercial viability of PEMFCs for small and automotive applications [1]. The poisoning of platinum catalyst adsorption sites may occur for high concentration of CO_2 in the fuel stream with adsorbed hydrogen atoms to produce CO (Equation 1) or possibly COH or COOH (Equation 2) [2].

$$CO_2 + 2Pt\text{-}H_{ads} \rightarrow Pt\text{-}CO + H_2O + Pt \qquad \text{Equation 1}$$

$$Pt\text{-}H_{ads} + CO_2 \rightarrow Pt\text{-}COOH_{ads} \qquad \text{Equation 2}$$

Development of both selective oxidation catalysts for reducing the CO content in reformates to a low level (<100 ppm) and CO-tolerant electrocatalysts are essential and most effective. Watanabe *at al.* reported high catalytic activity for H_2 oxidation in presence of 100 ppm CO on several binary Pt alloys catalysts such that Pt-Fe, Pt-Ni, Pt-Co and Pt-Mo alloys exhibiting increased stability [3]. They suggested that the surface of the alloys was composed of thin Pt layers and their modified electronic structure affected the chemisorption property of CO on the alloys. In addition, it is well rehearsed that the modification of the Pt by alloying Ru is the most efficient combination and is thought to involve a bifunctional mechanism [4,5]. In this, the Ru nucleates oxygen containing species at low potentials thereby, oxidizing CO on neighbouring Pt atoms. Also, ligand effects change the electronic density of the Pt by contributing d-electron density [6,7]. An electron transfer has been suggested from Ru to Pt within the alloy, thereby weakening the Pt-CO bond distance [8]. Important parameters in the design of the electrocatalysts include the structure and composition. Gasteiger *et al.* have suggested the optimum Ru surface composition to be a 10 at.% Ru for the chemisorption of methanol [9] that requires at least three adjacent Pt sites and a 50 at.% Ru alloy composition to promote the oxidation of

CO [5]. Another competitive CO-tolerant anode electrocatalyst is the PtMo system. Pozio and co-workers have reported comparative anode performance for PtRu/C with Pt:Ru atomic ratio of 1:1 and PtMo/C with low Pt:Mo atomic ratio for half cell measurements under H_2 flux [10]. This was attributed by the presence of Mo existing under different oxidation states, Mo^{3+}, Mo^{4+} and Mo^{6+} that co-ordinate H_2O molecules more easily than Ru. This assumption was based on the hypothesised Heyrowsky-Volmer mechanism for hydrogen oxidation reduction (HOR) on Pt-M electrodes, fewer atoms of Mo are needed to obtain the same adsorbed water than ruthenium. However, the kinetics of the H_2 reaction are not measurably affected by the presence of Mo and Ru in the surface as was observed on a well characterised bulk alloy PtMo electrode [11]. Grgur *et al.* reported for a well-characterised $Pt_{75}Mo_{25}$ alloy using a rotating disc electrode in H_2SO_4, a catalytic activity comparable to that of $Pt_{50}Ru_{50}$ alloy electrode for oxidation of H_2/100 ppm CO [12]. They confirmed this result for the $Pt_{70}Mo_{30}$ well-characterised bulk alloy electrode in sulfuric acid giving rise to current densities in the low-overpotential region comparable to those on $Pt_{50}Ru_{50}$ bulk electrode for oxidation of H_2/CO and about a factor of 50 times those on pure Pt surface [11].

The electrocatalytic activity towards CO, CO_2 and methanol was studied for a series of carbon supported Pt, PtRu and PtMo catalysts using half-cell electrochemical measurements. Single cell unit experiments were also performed at a fixed current density 0.5 A cm^{-2} using the 10 and 100 ppm CO in H_2, 25% CO_2 in H_2 and 40 ppm CO, 25% CO_2 in H_2. EXAFS data presented in the previous chapters described the differences in homogeneity of the supported bimetallic particles. Electrochemical results were then related to previous XAS data analysis and conclusions regarding the sensitivity of the reactions to alloy composition and structure were drawn.

2 EXPERIMENTAL

2.1 Materials

Table 1 lists the carbon supported platinum-based electrocatalysts supplied by Johnson Matthey Technology Center with the corresponding crystallographic parameters obtained using *ex situ* XRD completed by Johnson Matthey and *in situ* EXAFS techniques at Daresbury Laboratory.

	Composition		EXAFS parameters		XRD parameters	
Catalysts	wt. %Pt	wt. %M*	N_1(Pt-Pt) +N_1(Pt-M*)	R_2(Pt-Pt)	Crystallite size / nm	Lattice parameter / Å
Pt/C	40	/	9.1	3.91	4	3.92
Pt-Ru/C (A)	40	20	7.8	3.89	3.2	3.90
Pt-Ru/C (B)	40	20	7.6	3.85	2.4	3.86
Pt-Ru/C (C)	40	20	6.9	3.88	2.7	3.91
Pt-Mo/C	40	5	7.6	3.88	2.9	3.91

Table 1 : Nominal metal loading (wt.%) of the carbon supported catalysts and the corresponding EXAFS and XRD parameters. (M^*) stands for the secondary metal which is either Ru or Mo.

Note that the PtRu/C catalysts were fabricated under proprietary methods involving the chemical reduction of both metal precursors. These catalyst powders were formulated into anode fuel cell electrodes, as described in Chapter 2, section 2.1. The platinum loading on the electrode was 0.25 mg Pt cm^{-2}, except where indicated in the text.

In contrast to the Pt-Ru/C (B) electrocatalyst, the sample (A) has been described as a poor mixed alloy, as has the sample (C). To study the alloying effect on the anode performance through the half-cell and the single fuel cell unit measurements all three samples, (A), (B) and (C), were considered. It should be said that the sample (A) was not available at the time of the single cell experiment that is why (C) was chosen as the less well alloyed electrocatalyst.

2.2 Electrode testing

Button electrodes (1 cm^2) were tested using a standard three-electrode electrochemical cell in 1 mol dm^{-3} H_2SO_4 at 80 °C after having been exposed to CO and methanol. The experimental procedures are described in Chapter 2, sections 4.2 and 4.3. The cyclic voltammograms were recorded in the following potential range, - 0.6 V to 0.3 V vs. MMS, usually, at 10 mV s^{-1} after CO exposure to evaluate the Electrode Platinum Surface Area (EPSA) and the Electrochemical Area (ECA) for each of the electrodes. These areas were determined to enable comparison of the platinum area available for the electrochemical

reactions at the anode and the platinum utilisation, respectively. Finally, the polarisation curves were recorded to evaluate the performance of the electrode in the presence of methanol.

The anode electrodes (except the Pt-Ru/C (A) electrode) were also tested in a single fuel cell unit to assess the anode performance under real fuel cell operating conditions, as explained in Chapter 2, section 5.2. The evaluation of the MEAs were achieved with a standard Pt/C cathode electrode at a Pt loading of 0.7 mg Pt cm^{-2}. Four different fuel reformate mixes, i.e. 10 ppm and 100 ppm CO in H_2, (40 ppm CO + 25% CO_2) in H_2 and 25% CO_2 in H_2 were supplied to the anode in order to study the poisoning effect of CO and CO_2.

3 HALF-CELL RESULTS

3.1 Electrochemistry of CO covered Pt-based fuel cell electrodes

Figure 1 shows the cyclic voltammograms (CVs) recorded after CO exposure in a deoxygenated solution of sulfuric acid (1 mol dm^{-3}) for the series of anode fuel cell electrodes, in panels (a) to (e). The absence of the hydride region between – 0.6 V and - 0.4 V in the first forward anodic sweep for all the electrodes indicates that the electrode surface was nearly fully covered with adsorbed CO species.

In panel (a), the first forward anodic sweep exhibits a pre-peak at - 0.247 V and a main broad peak at - 0.056 V for the Pt/C electrode. These peaks are thought to correspond to the electrooxidation of CO from the bridge- and linearly-bonded sites, respectively. It should be noted that two successive scans were required to fully strip CO from the electrode surface, as indicated by a residual oxidative current density at the potential of CO electrooxidation (Figure 1, second scan). This latter phenomenom may be attributed to oxidation of the CO adsorbates in the pores of the catalyst material.

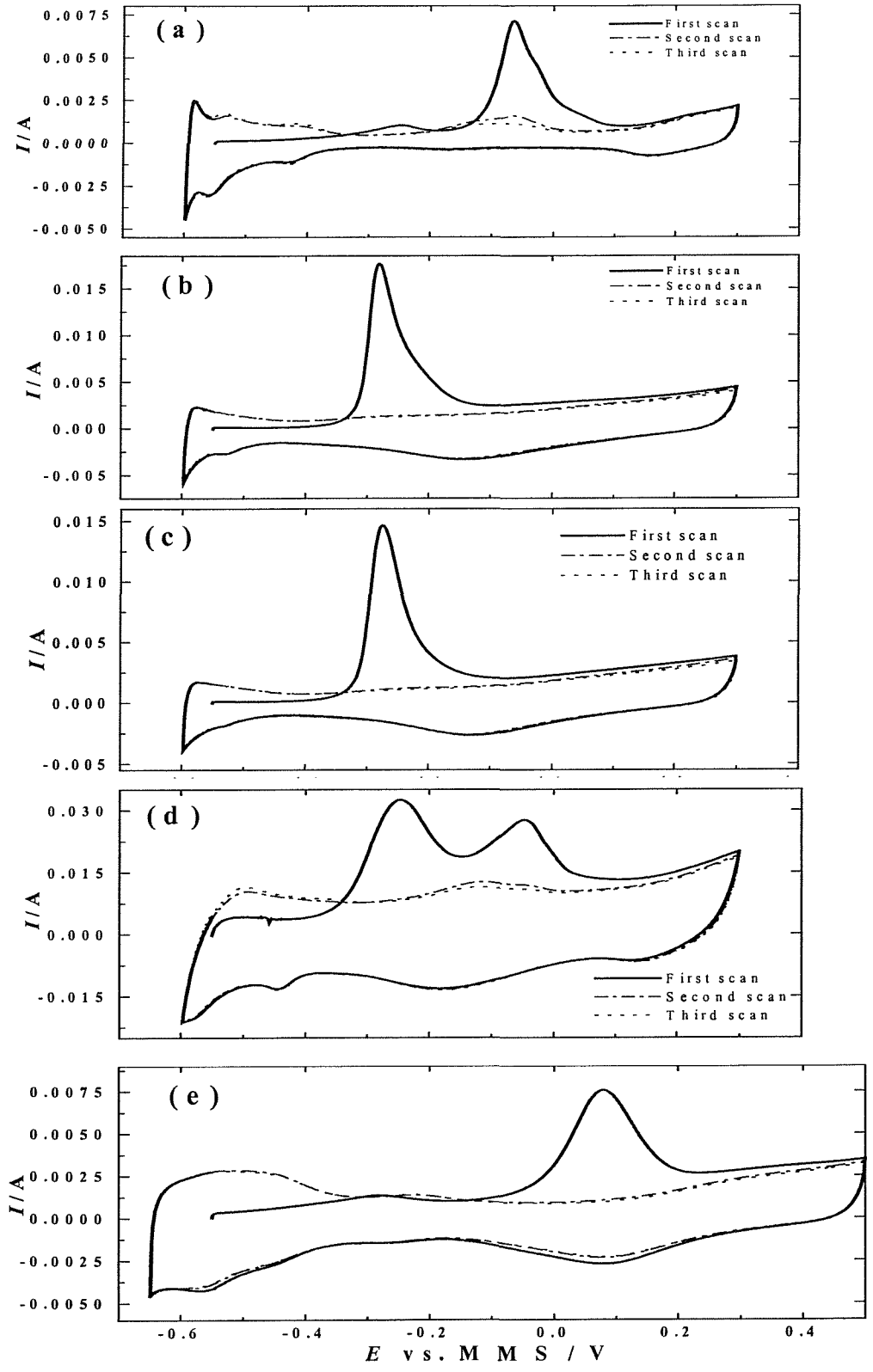

Figure 1: Cyclic voltammogram of Pt-based fuel cell electrodes (electrode area 1 cm^2) in 1 mol dm^{-3} H_2SO_4. Electrode surface exposed to CO saturated solution while the potential was held at – 0.55 V vs. MMS. After adsorption, CO was displaced from solution by N_2 bubbling for 30 mins. Sweep rate 10 mV s^{-1}. (a) is Pt/C, (b) is Pt-Ru/C (C), (c) is Pt-Ru/C (B), (d) is Pt-Ru/C (A), and (e) is Pt-Mo/C. The Pt loading is 0.25 mg Pt cm^{-2} for (a), (b) and (c) and 0.5 mg Pt cm^{-2} for (d) and (e).

In panels (b) and (c), the first forward anodic sweeps show a single CO stripping peak positioned at a potential of – 0.277 V and – 0.263V for Pt-Ru (C) and (B), respectively. As evaluated at ± 5 mV, the potentials of CO oxidation are similar for both the poor (C) and well mixed (B) Pt-Ru alloys. The CO stripping peak is shifted towards more negative potentials, i.e. about 200 mV, compared to that of the Pt/C electrode. This result is in good agreement with a previous study of the bulk polycrystalline Pt-Ru surface [5].

In contrast, two broad peaks positioned at - 0.246 V and - 0.046 V characterise the CO oxidation from the surface of the Pt-Ru/C (A) electrode, as shown in panel (d). The former peak can be ascribed to the oxidation of CO adsorbed on the Ru sites while the latter peak to the CO stripped off the Pt sites. This is in good correspondance with the position of the peaks of CO oxidation in the previous CVs (compare panel (a) and then (b) and (c)) and the reported studies using pure Ru or Pt bulk surfaces [5]. Thereby, these peaks confirm that Ru is not well mixed with Pt in the particles present in Pt-Ru/C (A).

The general features of the CVs for the series of Pt-Ru/C electrodes cycled in a deoxygenated solution of sulfuric acid (i.e. prior to CO exposure) correspond to that of the second and third scans in Figure 1. The main characteristic features of these CVs are the lack in the definition of the adsorption / desorption of hydrogen peaks between - 0.6 and - 0.4 V together with an increase of the current density when cycled towards more anodic potentials. This oxidative current is due to the oxidation of Ru-oxo-hydroxide species. Furthermore, the position of the oxide peak shifts to more negative potentials with Ru [13,14]. Nevertheless, a slight definition in the hydrogen adsorption peak at – 0.55 V and a larger pseudo-capacitance have been observed for the Pt-Ru/C (A) electrode and to a lesser extent for (C) when compared to (B). This peak in the hydride region may be ascribed to the weakly adsorbed hydrogen on Pt sites. Also, a residual oxidative current before the onset of the CO oxidation can be observed in the first forward anodic sweep for (A) and can be assigned to the larger proportion of Ru-oxohydro-species (panel (d)). This current is similarly observed for the Pt-Mo electrode and therefore, indicates the presence of Mo oxo-hydroxo species at low potentials.

The Pt-Mo/C electrode CV in panel (e) exhibits a small hump at – 0.284 V and a predominant broad oxidation peak at 0.076 V in the first forward anodic sweep following the CO exposure. Therefore, the Mo oxyhydroxide species enable the oxidation of some of

the CO adsorbates to take place at low potentials while a large majority of CO adsorbate are oxidised at potentials close to that of the Pt/C electrode. Both the second and the third scans illustrate the characteristic features for the Pt-Mo/C electrode cycled in a deoxygenated solution of sulfuric acid. In addition to the large pseudo-capacitance and the subsequent lack of definition in the hydride region, a reversible system appears at – 0.3 V, that has previously been assigned to the Mo (IV) / Mo(VI) redox couple.

Although the position, and moreover the shift towards more negative potentials of the CO stripping peak indicates the more facile oxidation reaction of CO with the Pt-Ru over the Pt and Pt-Mo electrodes, the active Platinum Electrode Area enables the quantification of the CO tolerance for each of these electrocatalysts.

3.1.1 Evaluation of the Active Platinum Electrode Area

Integration of the charge under the hydrogen adsorption peaks enables the calculation the Electrode Platinum Surface Area (EPSA) and ElectroChemical Area (ECA) as described in Chapter 2, section 4.2. However, this is not reliable for bimetallic samples as the oxidation of oxygenated species on Ru and Mo overlaps the oxidation of adsorbed hydrogen on Pt sites [4]. Thus, the EPSAs or electrode roughness factor and subsequently, the ECAs were evaluated from the charge under the CO stripping peaks and are presented in Table 2.

Samples	E_{peak}(CO) / V vs. MMS	EPSA / (cm^2 Pt/cm^2)	ECA / (m^2 Pt/g Pt)
40 wt.% Pt/C	0.056	129	51
40 wt.% Pt-20 wt.% Ru/C (A)	-0.246 -0.046	124	15
40 wt.% Pt-20 wt.% Ru/C (B)	-0.263	249	98
40 wt.% Pt-20 wt.% Ru/C (C)	-0.277	322	134
40 wt.% Pt-5 wt.% Mo/C	-0.284 0.076	167	33

Table 2: Electrochemical areas issued from the charge under the CO stripping peak.

As seen below the EPSAs values increase when using the Pt-Ru and Pt-Mo electrocatalysts. Therefore, the modification of the carbon supported small Pt particles with Ru and Mo enhance the surface area available for the electrochemical reactions at the anode electrode. It should be noticed, however, that *(i)* the Pt-Ru (A) electrocatalyst (when Ru is not very well mixed to Pt) does not provide such a perturbation and has equivalent electrochemical properties to that of the Pt electrode, *(ii)* the more well mixed Pt-Ru alloy, (B), provides a lower number of Pt sites for the hydrogen adsorption / desorption reaction than (C) and, *(iii)* the Pt-Mo electrocatalyst provides less Pt sites than the Pt-Ru electrocatalysts. The low utility percentages for the Pt-Ru (A) and the Pt-Mo electrodes can be assigned to the higher catalyst loading printed on the same geometric area. This implies that the whole proportion of platinum avalaible for the anode electrochemical reactions has not been used in totality, e.g. limitations of the fuel diffusion through the catalyst layer are dominant.

3.2 Methanol tolerance of Pt-based fuel cell electrodes

The polarisation data towards methanol are presented in Figure 2 for the series of platinum based carbon supported electrocatalysts listed in table 1. The data, namely the Potential vs. Current Density curves, were recorded in a 2 mol dm^{-3} methanol in 1 mol dm^{-3} H_2SO_4 solution at 80 °C and were *iR*-corrected using the current interrupt method, as described in Chapter 2, section 4.3.

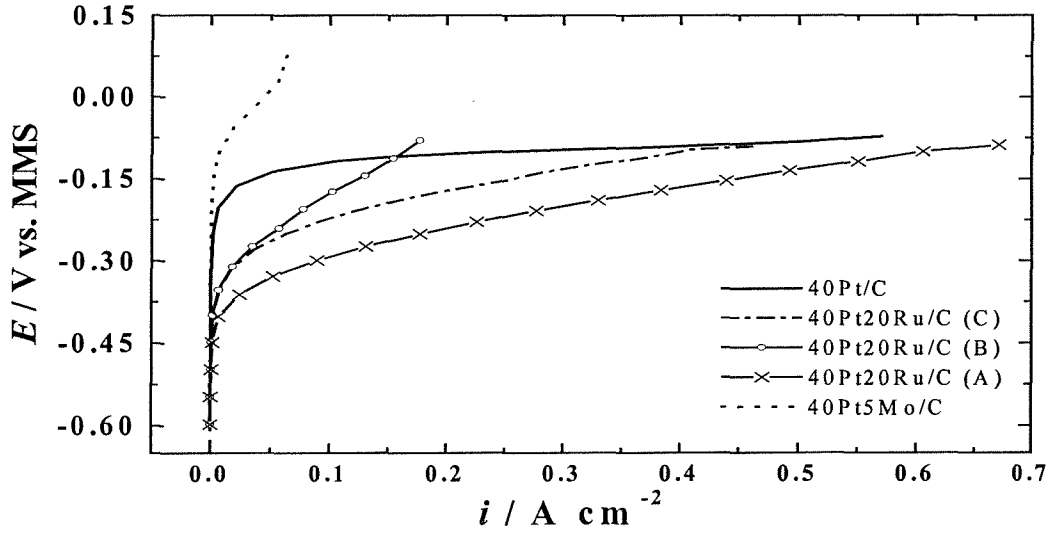

Figure 2: *iR* corrected polarisation curves for a series of Pt based catalysts; data were recorded in a solution (2 mol dm^{-3}) methanol in (1 mol dm^{-3}) H_2SO_4 at 80 °C.

The best performance was obtained with the electrode fabricated with the Pt-Ru/C type (A) catalyst, i.e. the poorly alloyed electrocatalyst. The electrode polarisation was – 0.330 V at a current loading of 50 mA cm^{-2}. The polarisation of the platinum electrode readily reaches a plateau at about - 0.1 V. In contrast, the polarisation of the bimetallic Pt-Ru electrocatalyst electrodes tested increases gradually and gives similar response to the platinum electrode at high current densities. All three of the Pt-Ru/C based electrodes exhibit lower overpotentials at low current density. However, the performance of the Pt-Ru type (B) electrode decays significantly from about – 0.3 V. This may be attributed to a mass transport limitation related to poor utilisation of the catalyst. In contrast, the Pt-Mo carbon supported electrode exhibits the poorest response in presence of methanol in the overall current density range, and gave a response which was largely mass transport limited.

4 SINGLE FUEL CELL RESULTS

4.1 Evaluation of Platinum Surface Active Area

The features of CVs presented in Figure 1 are representative of those recorded in the single fuel cell unit after having exposed the anode electrode for 15 minutes to CO. The corresponding Pt electrochemical areas are presented in Table 3.

Samples	EPSA / (cm^2 Pt/cm^2)	ECA / (m^2 Pt/g Pt)
40 wt% Pt/C	75	30
40 wt.% Pt-20 wt.%Ru/C (**B**)	140	55
40 wt.% Pt-20 wt.%Ru/C (**C**)	143	59
40 wt.% Pt-5 wt.% Mo/C	33	14

Table 3: Electrochemical parameters from the cyclic voltammetry.

The EPSAs values and, therefore, the ECAs values are smaller than those obtained through half-cell measurements. This difference may be attributed to the gas diffusion limitations, which do not occur in the case of fully flooded electrodes used in the half-cell measurements.

No distinct difference is apparent between the two types of PtRu alloy when used in the single cell. Furthermore, the EPSA for the Pt-Mo electrode is greatly decreased compared to the EPSA evaluated in the half cell.

4.2 Polymer electrolyte membrane fuel cell performance

$H_2//O_2$ and H_2//Air switching polarisation curves were recorded to assess the cathode performance. Figure 3 plots the Cell voltage (V) vs. current density (mA cm^{-2}) for the MEAs containing a C-supported Pt-based anodes and a typical standard Pt/C cathode.

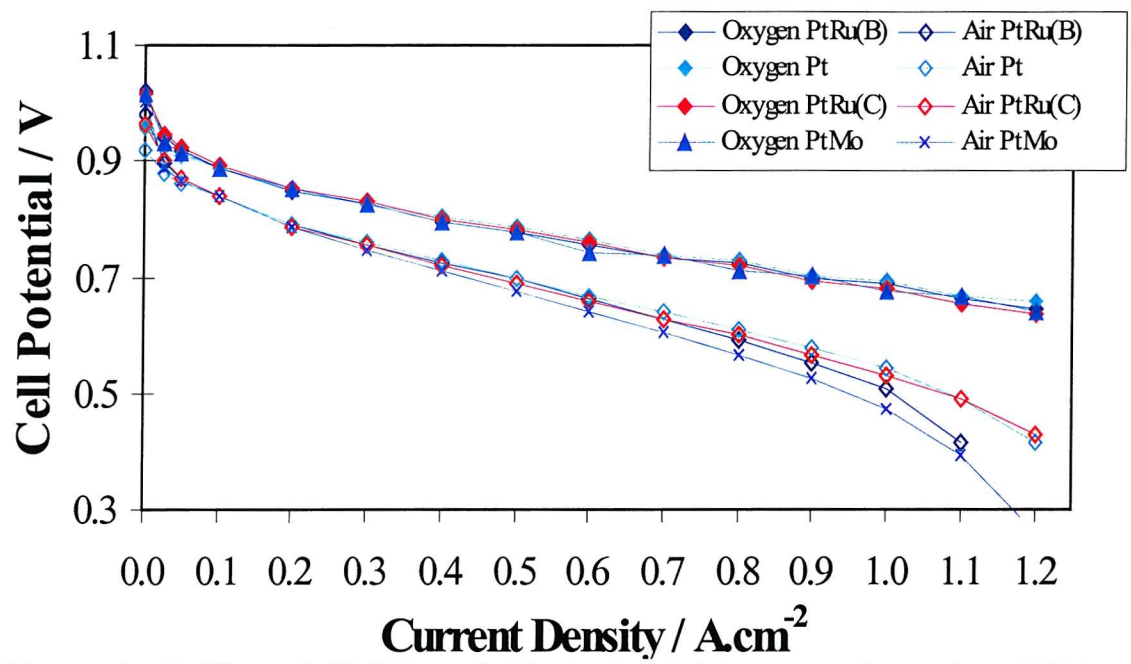

Figure 3: $H_2//O_2$ and H_2//Air switching polarisation curves for various MEAs, 30/30 psig, Temperature cell 80 °C, 1.5/2 stoichiometry, Nafion 115.

The $H_2//O_2$ polarisation curve shows that the use of the PtM/C anode as an electrode does not affect the performance of the cell. This agrees well with results reported elsewhere [15]. To anticipate the mass transport limitation the cathode gas supply was switched from oxygen to air. For the PtMo/C anode containing MEA, a gradual cell voltage loss was observed and attributed to a possible contamination in the system then, causing cathode flooding.

Table 4 gives the cell performance at a current density of 0.5 A cm^{-2}. Within an error of ±5 mV, the voltage of the single fuel cell unit comprising different type of MEAs are

equivalent one with another when using oxygen. By switching the oxidant supply to air, it generates a voltage loss between 80 mV for Pt and PtRu and 100 mV for PtMo. Again, the slightly lower performance observed for the PtMo was explained by the cathode flooding.

MEAs	Pt/C	PtRu/C (B)	PtRu/C (C)	PtMo/C
E_{cell} / mV $H_2//O_2$	783	779	783	778
E_{cell} / mV H_2//Air	696	697	690	677

Table 4: MEAs performance (mV) at 500 mA cm^{-2}.

4.3 The degradation of the fuel cell performance

Figure 4 compares the cell potential losses for the MEAs containing Pt/C, PtRu/C and PtMo/C anode electrode supply with H_2 fuel stream reformate gas mixes contaminated by CO and CO_2 at 0.5 A cm^{-2}.

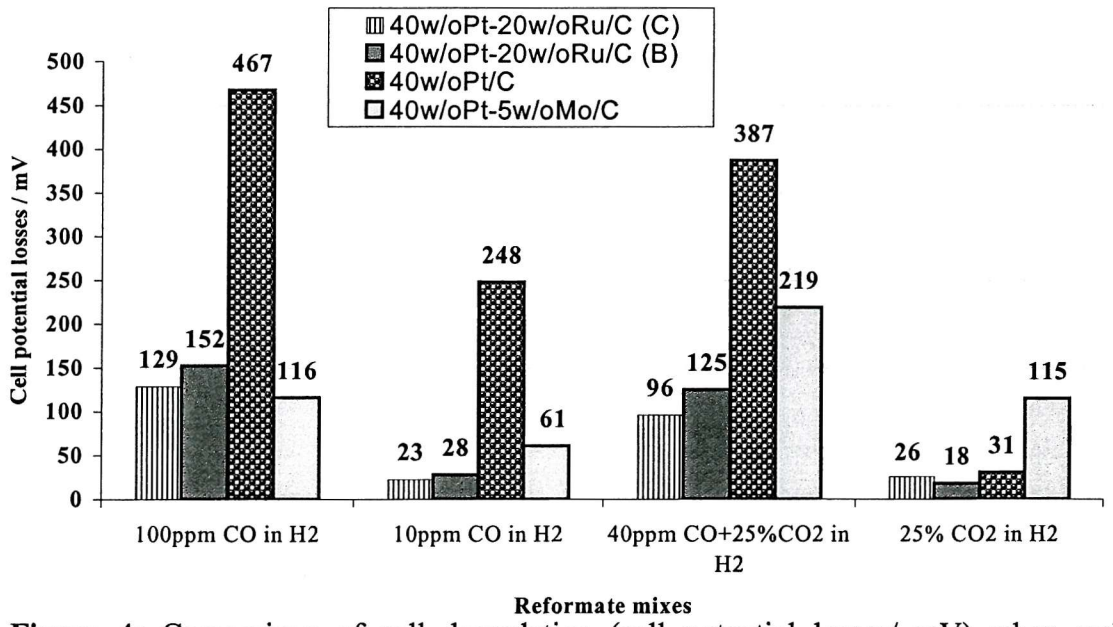

Figure 4: Comparison of cell degradation (cell potential losses/ mV) when carbon supported Pt and PtM anodes were exposed to various reformate gas mixes. The error value is ± 5 mV.

4.3.1 Impact of the CO in the reformate fuel stream

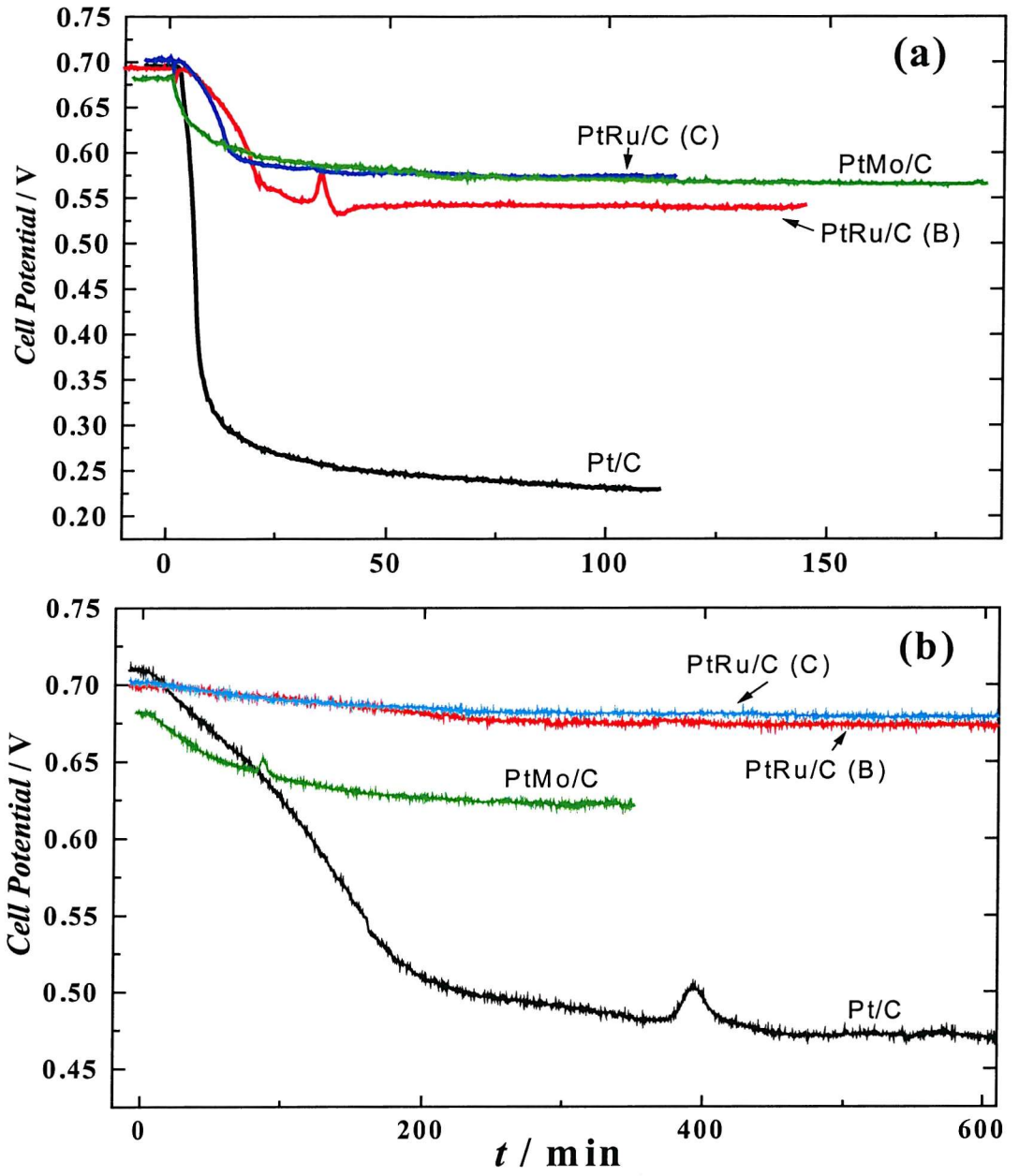

Figure 5: (a) Cell degradation as function of time at a fixed current density 500 mA cm^{-2} for different MEAs comprising different type of anode electrocatalysts which are supplied with 100 ppm CO in H_2 and (b) 10 ppm CO in H_2.
Note that the jump of the potential was attributed to water management system.

Figure 5 plots the fuel cell degradation as function of time when CO was incorporated at a concentration of 10 ppm and 100 ppm in the H_2 fuel stream, in panels (a) and (b), respectively. The cell potential for the Pt and the Pt-Mo electrocatalysts decay suddenly to readily reach a plateau, when 100 ppm CO in H_2 reformate fuel was supply to the anode. While PtRu MEAs degrade gradually until a stable value is attained.

As one can expect, the MEA containing the Pt/C anode electrode exhibits the greatest degradation at both low and high concentrations of CO compared to the other types of anodes used. However, amongst the series of MEAs the Pt-Mo and the Pt-Ru (C) require, equally, the lowest overpotentials to enable the electrochemical reaction to take place on the remaning Pt sites under 100 ppm CO in H_2, as indicated by cell potential losses of 116 mV and 129 mV, respectively. The well-mixed Pt-Ru alloy exhibit a poorer anode performance with a potential drop of 152 mV. If the single cell perform on 10 ppm CO in H_2, both Pt-Ru anodes show almost full CO tolerance and the Pt-Mo/C exhibit a modest potential loss of 61 mV. Within an error of ± 5mV the difference in cell potential between the Pt-Ru type (B) and (C) samples can be neglected at 10 ppm CO and then, present similar performance towards 10 ppm CO in H_2.

4.3.2 Impact of the CO_2 in the reformate fuel stream

Figure 6 shows that the fuel cell performance when using a Pt and Pt-Ru electrocatalyst is not really affected by the presence of 25 % CO_2 in the fuel stream, as indicated by small potential loss. However, the Pt-Mo/C catalyst shows a significant drop of the cell voltage, i.e. 115 mV, that illustrates low CO_2 tolerance of the catalyst.

4.3.3 Impact of CO and CO_2 in the reformate fuel stream

Figure 7 illustrates the degradation of the cell potential as function of time, when the single cell operates on 40 ppm CO, 25 % CO_2 in H_2. The poorest anode performance was observed for the Pt (i.e. 387 mV). The Pt-Mo/C electrocatalyst shows a significant loss in the cell voltage of 219 mV and both Pt-Ru electrodes exhibit almost similar losses to that observed on 100 ppm CO/H_2. However, the Pt-Ru/C (C) anode seems to less desactivated than the more well mixed PtRu alloy (B).

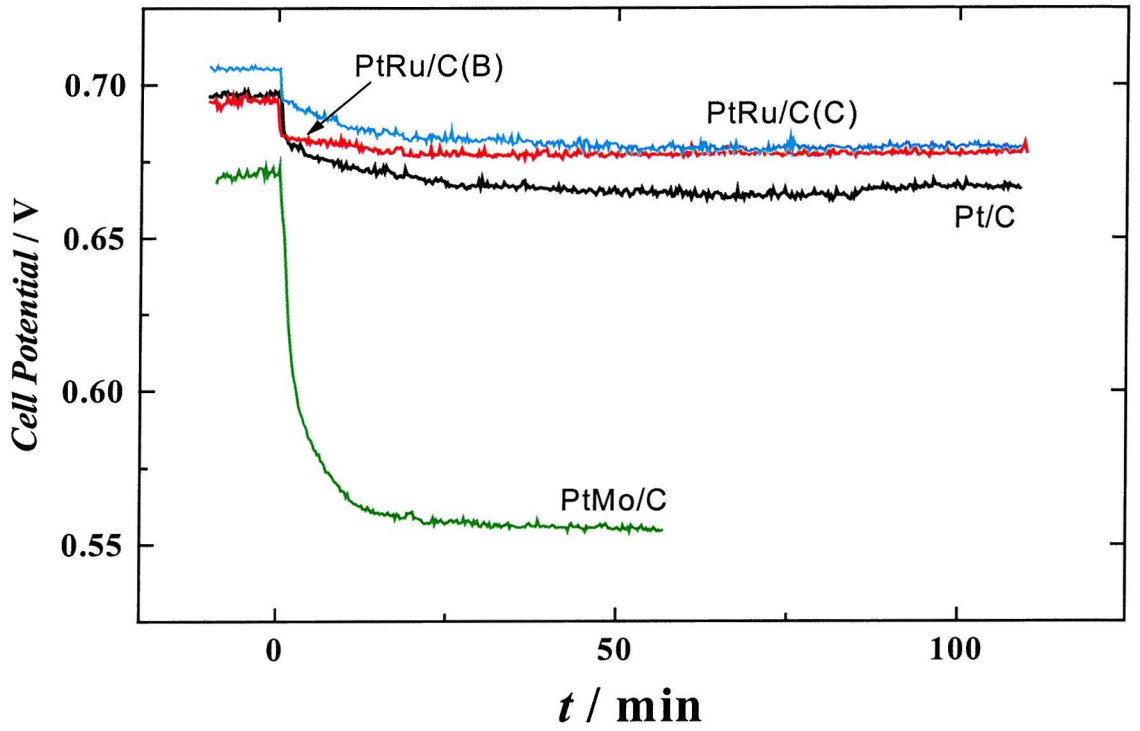

Figure 6: Cell degradation as function of time at a fixed current density 500 mA cm^{-2} for MEA comprising different type of anodes which are supplied with 25 % CO in H_2.

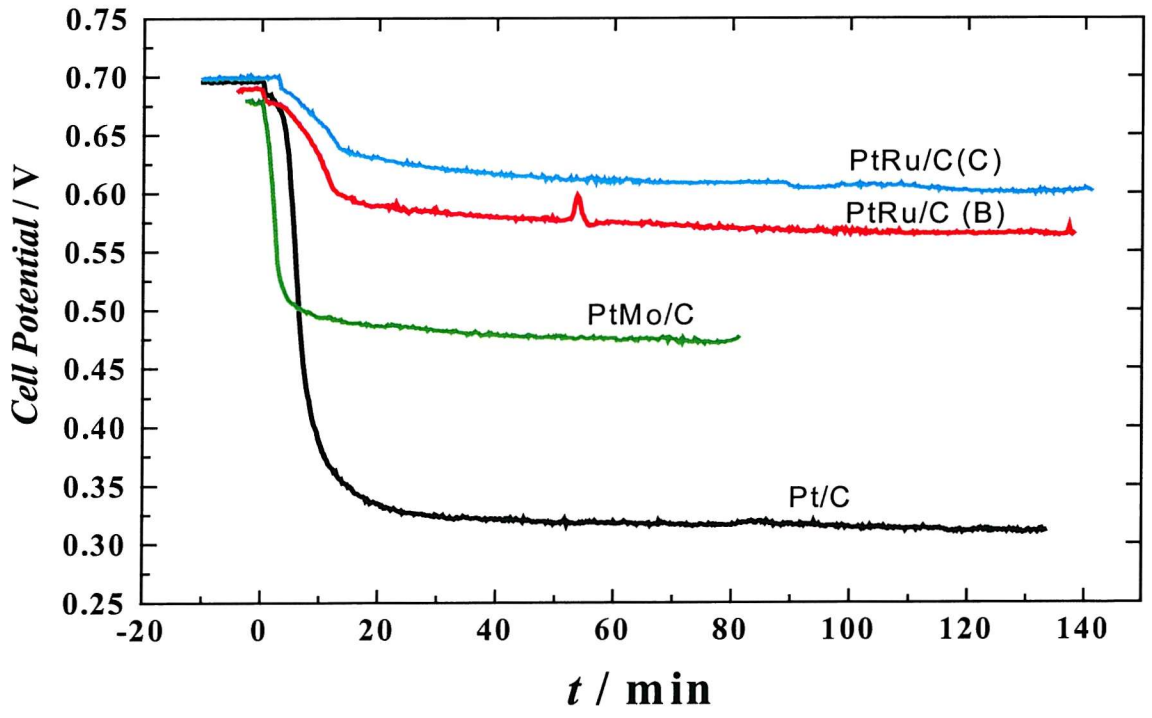

Figure 7: Cell degradation as function of time at a fixed current density 500 mA cm^{-2} for MEA comprising different type of anodes which are supplied with (40 ppm CO + 25 % CO_2) in H_2.

5 DISCUSSION

Cyclic voltammograms recorded in the half-cell experiments have shown clear differences between the carbon supported Pt and the binary Pt-M (with M = Ru or Mo) anode fuel cell electrodes in deoxygenated sulfuric acid. The lack of definition of the hydrogen adsorption/desorption peaks and a large pseudo-capacitance were ascribed to the oxidation process of the oxyhydroxide M species [16,17]. This redox process occurs in particular when the secondary element, M, is less mixed within the Pt nanoparticle, as seen for the Pt-Ru (A) and the Pt-Mo electrocatalysts. Previous *ex situ* XRD and *in situ* EXAFS measurements have assessed the extent of the alloy formation. A reduction of the lattice parameter (*a*) indicated that Ru is well-alloyed to Pt within the particle for (B), i.e. $a_{PtRu/C(B)}$ = 3.86 Å against $a_{Pt/C}$ = 3.92 Å, while no significant lattice contraction was observed for PtRu/C (A), PtRu/C (C) and PtMo/C, as indicated in Table 1. *In situ* EXAFS data (e.g. second shell Pt-Pt coordination distance) confirmed the preminilary XRD results. Also, the correspondance between both the Pt-M and M-Pt coordination numbers assessed the arrangement of M within the Pt fcc lattice. Also, the reduction of the first Pt-Pt coordination distance together with the enhanced *d*-band vacancy for the Pt-M/C type electrocatalysts have pointed out possible variations in the chemisorptive properties of the platinum particles. The potential of the CO electro-oxidation reaction shifts towards more negative potentials for the Pt-Ru/C electrodes as compared to that of the Pt electrode, and varies between – 0.27 V and – 0.24 V as Ru is less well mixed with Pt in the particle.

Whereas the majority of the CO adsorbed species were oxidised at potentials close to that occuring on the Pt/C electrode, the onset potential of the CO electro-oxidation reaction is believed to start at lower potential for the PtMo/C electrode, as indicated by the small oxidation peak at - 0.284 V. The additional oxidation peak observed at – 0.3 V, after having stripped CO from the surface of the particle was assigned to redox reactions of the Mo on the surface of the metal particle [11]. Previous XANES studies at the Mo K edge demonstrated the presence of Mo within the electrocatalyst particle under two oxidation states, i.e. Mo(+IV) and Mo(+VI). Although Mo oxyhydroxide species dispersed on the surface of the particle may contribute to the CO electro-oxidation reaction, only a small number of sites are active, as characterised by the small current density observed for the oxidative peak at - 0.284 V. These results have been discussed in terms of heterogeneity of the surface PtMo/C catalyst in comparison to PtRu/C [18]. Crabb and co-workers have recently reported the mechanism by which the surface of Mo species need to be in an

oxidised state but also need to be easily reduced to be able to undergo oxygen transfer to promote the electro-oxidation of CO by $PtMoO_x/C$ electrocatalysts [19].

The testing of Pt/C, PtRu/C and PtMo/C electrocatalysts in a single fuel cell provided direct evidence that the PtMo/C catalyst provides high CO-tolerance in 100 ppm CO/H_2, as has the PtRu/C (C) catalyst. The calculated Pt active surface area for the PtMo/C electrode in acidic solution is rather small in comparison to the PtRu/C electrodes (see Table 2) and quite similar to that measure for Pt/C electrode. Although all the catalyst EPSAs values were reduced when measured in MEAs, the EPSA of the PtMo/C catalyst was even lower than that obtained for the Pt/C. This is somehow surprising as XRD crystallite size of the PtMo/C catalyst was see to be smaller compared to pure Pt/C catalyst. This may indicate that the proportion of catalyst surface in contact with Nafion® within the MEA is different for the PtMo/C catalyst compared to the well mixed alloy PtRu/C (B) and Pt/C. Thereby, the greater CO tolerance for the PtMo/C and PtRu/C (C) may be understood in terms of the Pt surface area available.

Both the Pt-Ru and the Pt-Mo electrocatalysts showed improved the CO tolerance but are believed to do so using a different mechanism, as has already been outlined in the literature [20]. The process by which the Pt-Mo catalyses the CO oxidation reaction invokes a promoted mechanism that involves the oxyhydroxide Mo species at low potentials. In contrast, the Pt-Ru electrocatalysts provide changes in the intrinsic properties of the Pt nanoparticle such that the Pt-CO bond is weakened together. This was supported by the EXAFS data at the Ru K edge that demonstrated the metallic nature of the Ru at the potentials where the hydrogen oxidation reaction occurs. Therefore, this result disagrees with the previous assumption where the rate limiting step for the CO electrooxidation reaction depends on the combination of CO with Ru oxide species for the well alloyed PtRu electrocatalyst [5].

The reduction of CO_2 on Pt electrodes to produce CO-like species has been known for 40 years [2]. Therefore, it is not surprising that CO_2 has a modest poisoning effect on PEMFC anode performance. The single cell results show that PtRu has a lower loss than Pt. Recent studies have shown that on polycrystalline Pt electrodes, CO is favored as the electroreduction product [21]. Pt and PtRu have lower CO coverage than that achieved with 10 ppm, as indicated by the small losses in the cell voltage. Whereas the coverage on the PtMo catalyst is more comparable to 100 ppm CO. This is partially due to relatively low

EPSA of the PtMo, when compared to Pt and PtRu. Alternatively, it appears that PtMo is a much more effective catalyst for the electroreduction of CO_2 than Pt and PtRu. This may be a consequence of its ability to electro-oxidize CO at low potentials. The electroreduction of CO_2 is the reverse reaction as shown below

$$CO_2 + 2\,H^+ + 2\,e^- \rightarrow CO + 2\,H_2O$$

$$Eo = -0.103 - 0.0591\,pH + 0.0295 \log [pCO_2 / pCO] \quad [22]$$

Therefore, the ability to catalyse the forward reaction (CO electrooxidation) also indicates the ability to catalyse the reverse reaction (CO_2 electrooxidation). The magnitude of both reactions depends strongly on the concentration of each reactant present.

The dilution effect of CO_2 in the fuel stream appears for the single cell results of Pt and PtRu in 40 ppm CO, 25% CO_2 in H_2 as reflected by the similarity in the performance behavior to that obtained with 100 ppm CO. Whereas the PtMo performance is controlled by both CO and CO_2 poisoning.

The improvement in the catalytic activity for the methanol electrooxidation reaction when using Pt-Ru electrocatalysts compared to pure Pt electrocatalysts was observed, in good agreement with other studies [9]. However, the lowest anode polarisation towards methanol was seen for the poorly mixed Pt-Ru/C catalyst at low current densities. This is consistent with the fact that the methanol electro-oxidation is a surface sensitive reaction. Recently, the investigation of the methanol oxidation at small Pt particles dispersed on a basal plane graphite disc have suggested that the electro-oxidation of methanol was sensitive to the morphology of the Pt surface [23]; with the coordination of CO_{ads} being three-fold on the particles and the small particles acting as nucleation sites for the CO_2 gas. The large deactivation of the Pt-Mo/C anode in the presence of methanol may be assigned to diffusion limitation due to CO_2, product of the methanol dehydrogenation reaction. Thus, the CO_2 layer may hinder the diffusion of methanol to the electrocatalyst. Wang and co-workers have, however, reported the electrocatalytic activity for the methanol electro-oxidation of a modified electrode, $PtMoO_x$/Glassy Carbon having an optimal Pt/Mo atomic composition that lies between 1.5 and 2.0, based on cyclic voltammetry [24].

6 CONCLUSION

The single cell results have clearly shown that the performance of a fuel cell lowered when the anode gas reformate supply was contaminated with CO and/or CO_2. The CO_2-intolerance of the PtMo/C might attenuate the possible potential use of the catalyst in PEMFC, despite the excellent CO-tolerance of the catalyst at 100 ppm CO. In contrast, the Pt and Pt-Ru system were largely deactivated by high CO concentration in the fuel stream while almost fully tolerant to low CO concentration and CO_2 in the fuel stream. If the fuel cell operates on 100 ppm CO/H_2 at 0.5 A cm^{-2}, the level of intermixing between Pt and Ru has an impact on the CO tolerance of the catalyst. In addition, a poorly mixed PtRu enhanced the electrocatalytic activity of the electrooxidation of methanol to a larger extent to the well mixed PtRu/C catalyst. The electrochemical tests were consistent with the promoted mechanism proposed for the PtMo/C electrocatalyst as well as the intrinsic mechanism for the Pt-Ru/C electrocatalyst.

7 REFERENCES

[1] Gottesfeld, S.; Pafford, J., *J. Electrochem. Soc.,* **1988**, *135*, 2651.

[2] Giner, J., *Electrochemica Acta,* **1963**, *8*, 857.

[3] Watanabe, M.; Igarashi, H.; Fujino, T., *Electrochemistry,* **1999**, *67*, 1194.

[4] Watanabe, M.; Motoo, S., *J. Electroanal. Chem.,* **1975**, *60*, 275.

[5] Gasteiger, H. A.; Markovic, N.; Ross, P. N.; Cairns, E. J., *J. Phys. Chem.,* **1994**, *98*, 617.

[6] Ross, P. N.; Kinoshita, K.; Scarpellino, A. J.; Stonehart, P., *J. Electroanal. Chem.,* **1975**, *63*, 97.

[7] Frelink, T.; Wisscher, W.; Van Veen, J. A. R., *Surf. Sci.,* **1995**, *335*, 353.

[8] Goodenough, J. B.; Manoharan, R.; Shukla, A. K.; Ramesh, K. V., *Chemistry of Materials,* **1989**, *1*, 391-.

[9] Gasteiger, H. A.; Markovic, N.; Ross, P. N.; Cairns, E. J., *J. Phys. Chem. B,* **1993**, *97*, 12020.

[10] Pozio, A.; Giorgi, L.; Antolini, E.; Passalacqua, E., *Electrochemica Acta,* **2000**, *46*, 555.

[11] Grgur, B. N.; Markovic, N.; Ross, P. N., *J. Phys. Chem. B,* **1998**, *102*, 2494.

[12] Grgur, B. N.; Zhuang, G.; Markovic, N. M.; Ross, P. N., *J. Phys. Chem. B,* **1997**, *101*, 3910.

[13] Mahmood, T.; Williams, J. O.; Miles, R.; McNicol, B. D., *J. Catal.,* **1981**, *72*, 218.

[14] McNicol, B. D.; Short, R. T., *J. Electroanal. Chem.,* **1978**, *92*, 121.

[15] Antolini, E.; Giorgi, L.; Cardellini, F.; Passalacqua, E., *J. Solid State Electrochem,* **2001**, *5*, 131.

[16] Hamnett, A.; Kennedy, B. J.; Wagner, F. E. *J. Catal.,* **1990**, *124*, 30.

[17] Grgur, B. N.; Markovic, N. M.; Ross, P. N., in *Proton Conducting Membrane Fuel Cells*; Gottesfeld, S. F., T. F. and Halpert, G., Editors, PV 98-27, p. 176, The Electrochemical Society Proceedings Series, Pennington, NJ, (1999).

[18] Ball, S. C.; Hodgkinson, A.; Hoogers, G.; Maniguet, S.; Thompsett, D.; Wong, B. *Electrochem. Solid State Lett.,* **2002**, *5*, A31-A34.

[19] Crabb, E. M.; Ravikumar, M. K.; Qian, Y.; Russell, A. E.; Maniguet, S.; Yao, J.; Thompsett, D.; Hurtford, M.; Ball, S. C., *Electrochem. Solid State Lett.,* **2002**, *5*, A5-A9.

[20] Cooper, S. J.; Gunner, A. G.; Hoogers, G.; Thompsett, D., in *Reformate tolerance in proton exchange membrane fuel cells: electrocatalysts solutions*; O.Savadogo, P. R., O.Savadogo, P. R.s, p. 286, Montreal, Canada, (1997).

[21] Hoshi, N.; Hori, Y. *Electrochemica Acta,* **2000**, *45*, 4263-4270.

[22] Pourbaix, M. *Atlas of Electrochemical Equilibria in Aqueous Systems*; Pergamon Press: Oxford, (1966); pp 452.

[23] Christensen, P. A.; Hamnett, A.; Munk, J.; Troughton, G. L. *Journal of Electroanalytical Chemistry,* **1994**, *370*, 251-258.

[24] Wang, Y.; Fachini, E. R.; Cruz, G.; Zhu, Y.; Ishikawa, Y.; Colucci, J. A.; Cabrera, C. R. *Journal of the Electrochemical Society,* **2001**, *148*, C222-C226.

CONCLUSIONS AND FURTHER WORK

This thesis has presented the results for a study of carbon supported Pt and Pt-M (with M = Ru or Mo) alloy electrocatalysts by means of X-ray absorption spectroscopy (XAS) combined with electrochemistry. *In situ* extended X-ray absorption fine structure (EXAFS) experiments enabled the determination of both the electronic properties (e.g. change in the Pt 5d band vacancy) and short range structural information (e.g. coordinations numbers and distances) for polymer electrolyte membrane fuel cell (PEMFC) catalysts with an element specificity under conditions much closer to real fuel cell operating conditions, e.g. acidic medium, potential control and CO exposure. The purpose of this research work was to investigate the origins of the well-established higher catalytic actvity for the CO oxidation reaction and/or the methanol oxidation reaction by Pt alloys in comparison with Pt when used as anode fuel cell electrodes. For example, the performance of the state-of-the-art PtRu/C anode catalyst together with the PtMo/C was reported when tested in a PEMFC single cell in chapter 6.

Chapter three discussed the influence of the secondary element M within the structure of C-supported Pt nanoparticles. EXAFS results for anode fuel cell electrodes based on a 40 wt.% Pt, 20 wt.% Ru/ C type electrocatalyst were reported for both the Pt L_{III} and the Ru K edges when a reducing potential was applied (to avoid structural changes due to the platinum oxide formation). The decrease of the amplitude of the EXAFS signal compared to that obtained for the Pt/C electrode evidenced the presence of Ru within the first coordination sphere, also confirmed by the data analysis indicating a Pt-Ru coordination distance at about 2.71 Å. In addition, an interference phenomenom between Pt and Ru neighbouring atoms within the first coordination sphere gave rise to a phase cancellation at about k ~10 $Å^{-1}$. Ru and Pt backscattering atoms being out of phase with one another at this energy, a subsequent splitting of the first coordination peak of the Fourier transform is observed in proportion to the degree of alloying of the Ru within the Pt face centered cubic lattice. Thereby, this feature may indicate the level of inter-mixing between Pt and Ru. Similar Pt-Ru and Ru-Pt coordination numbers and distances (collected at both edges) confirmed the degree of alloy formation. The changes visualised for the experimental data were supported by simulations made at both edges with increasing Ru content. Although

similar results where reported, the Ru K edge data was seen to be more sensitive to phase correction of the Fourier transforms. From EXAFS data analysis, the structural parameters described smaller PtRu/C particles (i.e. shortened (Pt-Pt) cordination distances and smaller average coordination number) compared to the Pt/C catalyst. The complementary study at the Ru K edge described the metallic form of Ru with the absence of Ru-O contribution at the reducing potential. Therefore, conclusions drawn on the basis of 'as-prepared' PtRu/C catalyst are thought to be less relevant in modeling the catalytic activity of PtRu as predominantly from Ru oxides.

If these studies were to be extended, it may be interesting to illustrate simulations that have been done at both the Pt L_{III} and the Ru K edges to visualise the impact of Ru in the Pt structure. *In situ* EXAFS spectra should be recorded for the PtRu/C electrocatalysts made with various Pt:Ru atomic ratios, that span concentrations from pure Pt to pure Ru.

Chapter four presented the XAS data as function of potential for anode fuel cell electrodes based on the following catalysts: Pt/C, PtRu/C, PtMo/C and $PtMoO_x$/C. Structural changes were mainly observed at the potential of oxide formation on platinum. Smaller Pt-Pt coordination numbers and expanded Pt-Pt interatomic distances were obtained, specifically for Pt/C and the PtRu/C well mixed alloy catalysts. These changes, anticipated by the decrease of the main peak of the Fourier transform, indicated the oxide formation, confirmed by the presence of the Pt-O contribution located at 2 Å, was not restricted to the electrode surface. Quantification of the oxide monolayer on the platinum surface (Pt-O coordination number) was not feasible with the EXCURV98 program as Pt and Ru scattering contributions mask the backscattering phase and amplitude from the neighbouring O atoms.

White line analysis confirmed the enhancement of the Pt 5d-band vacancy with the introduction of the secondary element at a reducing potential, where hydrogen electrooxidation occurs. The well mixed PtRu/C has a great impact on the modification of the Pt oxidation state. This electronic effect implies the weakening of the Pt-CO bond and, hence the modification of the equilibrium coverage of CO and H_2, favoring an increased proportion of H_2 electrooxidation sites.

For the PtMo/C and the $PtMoO_x$/C catalysts, the lack of Mo-Mo contribution in the first shell, together with the presence of a Mo-O contribution situated at 1.95 Å, and the difference between Pt-Mo and Mo-Pt coordination numbers demonstrated that the structure consisted of a Pt core atom surrounded by a monolayer of oxidised Mo species. A complementary XANES study at the Mo K edge demonstrated the presence of two oxidation states for Mo, Mo(VI) and Mo(IV), then suggesting the presence of Mo oxyhydroxide species taking part in the CO tolerance. The C-supported PtMo catalyst having low Mo content appears as the most potential dependant. This was evidenced upon electrochemical reduction by the increased Mo-Pt coordination number together with the contraction of the Mo-Pt coordination distance as well as the absence of Mo-O coordination distance at 1.75 Å (characteristic in the 'as prepared' catalyst).

Future *in situ* EXAFS investigations might be realised for the PtMo/C to explore the impact of the reversible electrochemical system at -0.3 V vs. MMS on the structure of the catalyst, particularly for the catalyst with a smaller amount of Mo at the Mo K edge.

Chapter five showed the effectiveness of *in situ* XAFS spectroscopy to determine the nature of adsorbate molecules, namely CO and O on the surface of small carbon supported platinum particles. The difference file technique offers the ability to substract heavier scatterers, e.g. Pt contributions, from the experimental EXAFS spectrum to obtain the contributions of lighter atoms (C and O). As a result, the Pt-C contribution located at 1.85 Å was ascribed to linearly adsorbed CO on Pt, at potentials in good agreement with that found in the cyclic voltammogram, i.e. below the onset potential for CO oxidation. However, the carbon support interaction (e.g. Pt-C contribution at 2.71 Å) hinders study of C-O bond distance as well as the anticipation for possibly different adsorption sites (linear, bridge, or multi-fold bonding).

The application of the difference file technique to analyse CO adsorption on PtRu and PtMo electrode surfaces would illustrate the assumption for the two distinct mechanisms believed to occur for CO adsorption and oxidation at surfaces.

In the last chapter, an electrochemical study of the Pt/C, PtRu/C and PtMo/C catalysts in half cell and single cell environments was presented. The carbon supported PtRu and PtMo catalysts showed significant CO-tolerance in CO/H_2 mixtures under PEMFC test conditions at 80 °C at a fixed current density of 0.5 A cm^{-2}. The PtRu/C electrocatalysts exhibited higher cell performances than PtMo/C in 10 ppm CO in H_2. However, PtMo/C and the less well mixed alloy PtRu/C provided the lowest potential drop under 100 ppm CO in H_2. The PtMo/C electrocatalyst was largely deactivated by 25% CO_2 in H_2. Such CO_2-intolerance is a serious draw back in the potential use of the PtMo/C catalysts in PEMFC.

Half cell results have shown that the PtRu/C catalyst appears as the most tolerant to methanol, compared to Pt and PtMo. The highest catalytic activity was observed for the poorly mixed PtRu/C electrocatalyst, therefore indicating the structure sensitivity of the methanol electrooxidation reaction. Additional half cell measurements conducted in presence of CO provided evidence of the intrinsic mechanism for the CO electrooxidation reaction by PtRu/C electrocatalyst (e.g. shift of the potential of the CO oxidation peak towards more cathodic potentials). This was supported by the EXAFS results when both electronic and structural effects arise from the modification of small Pt particle by Ru. While Mo on the surface of the Pt particle was seen to promote CO adsorbate species oxidation at lower potential than that on Pt.

In summary, the combined XAS and electrochemical studies presented in this thesis shed new light on the origins of enhanced catalytic activity behaviour of PtRu/C and PtMo/C alloys over that of Pt/C. The degree of mixity of the two components in the alloy phase was seen to be of great importance. For the PtRu/C catalysts the enhanced activity could be related to electronic effect, the intrinsic mechanism and less to the presence of oxides on the Ru surface sites. The enhanced behaviour of PtMo/C, however, was shown to be related to the presence of the reversible Mo(IV)/Mo(VI) redox couple of Mo species at the surface of the metal nanoparticles.